The many mysteries of graphene oxide

A Thesis Submitted to the

College of Graduate Studies and Research

in Partial Fulfillment of the Requirements

for the degree of Doctor of Philosophy

in the Department of Physics and Engineering Physics

University of Saskatchewan

Saskatoon

By

Adrian Hunt

Permission to Use

In presenting this thesis in partial fulfilment of the requirements for a Postgraduate degree from the University of Saskatchewan, I agree that the Libraries of this University may make it freely available for inspection. I further agree that permission for copying of this thesis in any manner, in whole or in part, for scholarly purposes may be granted by the professor or professors who supervised my thesis work or, in their absence, by the Head of the Department or the Dean of the College in which my thesis work was done. It is understood that any copying or publication or use of this thesis or parts thereof for financial gain shall not be allowed without my written permission. It is also understood that due recognition shall be given to me and to the University of Saskatchewan in any scholarly use which may be made of any material in my thesis.

Requests for permission to copy or to make other use of material in this thesis in whole or part should be addressed to:

Head of the Department of Physics and Engineering Physics
163 Physics Building
116 Science Place
University of Saskatchewan
Saskatoon, Saskatchewan
Canada
S7N 5E2

Abstract

Graphene, the first two-dimensional crystal ever found, is a material that has attracted fervent and sustained interest from condensed matter researchers from around the world. It has a unique and unprecedented band structure in a bulk material: the bands near the Fermi level are linear, leading to massless charge carriers that propagate at the speed of light. However, graphene does not possess a band gap, and as such, it cannot be used to process information in any electronic device that uses digital logic. Graphene is oxidized when several different basic functional groups like hydroxyls, carboxyls, and epoxides bond to the hexagonal carbon basal plane to make graphene oxide (GO). The result is a non-stoichiometric and highly disordered system that, according to the results shown in this thesis, consists of zones of densely-packed functional groups interspersed between zones of relatively small functional group concentration. This has been confirmed by DFT calculations presented here, which is the first time that a successful simulation of the GO density of states has been compared to X-ray data. Contrary to many assumptions in the literature, many of the features in the density of states of GO are due not to carbon sites bonded to functional groups, but are due to nearby non-functionalized carbon sites.

The band gap of graphene oxide is principally controlled by oxidation level. Reduction, followed by heating, will regenerate the near-Fermi states and close the band gap significantly as has been seen by others. However, heating non-reduced graphene oxide can also result in a much-reduced band gap, which occurs because intercalated water can react with the heated GO sample to remove functional groups by creation and eventual expulsion of carbon dioxide. The band gap of GO is further complicated by stacking effects if it is multilayered, because residual π-conjugated states in neighboring planes interact. The two major types of stacking in graphite are AA-stacking and AB-stacking. AA-stacking interactions cause the π^* resonance to broaden and push states to lower energy, which means that AA-stacking determines the width of the gap in highly oxidized samples. However, direct oxidation of graphene is not the only way that one alter the electronic structure of GO. Other results presented here also show that non-covalent functionalization of graphene oxide by amorphous solid water is a powerful, reversible way to dramatically change the GO electronic structure.

Acknowledgements

I would like to thank Alex Moewes, my supervisor, for the opportunity and support to complete my work. Alex has ever been the supervisor that I required in the moment: Pushing for results some times, but at other times, allowing me the walk the path as I needed. I thank the staff at the Canadian Light Source and the Advanced Light Source for the use of such fine scientific instruments. The SGM beamline at the Canadian Light Source, in particular, has been constantly improved, with new and amazing functions added over time. Some of the experiments presented in this thesis were not possible when I started my Ph.D. work, and never would have been possible without the efforts of the SGM staff. In terms of funding, I would like to thank the Department of Physics and Engineering Physics for their financial support in the beginning. For last three years, I have been on a CGS-D3, which is a simply fantastic scholarship from the Canadian Natural Sciences and Engineering Research Council that has allowed me to support my family. I would therefore like to thank NSERC for their generous funding. Last but certainly not least, I thank God, for He has walked the path with me at all times to see me to the end.

To my wife, Jodi, and my three children Selene, Connor, and Quinn, all of whom have shared with me the stress of graduate student life with grace and dignity.

Contents

List of Tables

List of Figures

List of Abbreviations

XANES	X-ray absorption near-edge spectroscopy
TFY	Total fluorescence yield
PFY	Partial fluorescence yield
TEY	Total electron yield
XES	X-ray emission spectroscopy
nRXES	Non-resonant X-ray emission spectroscopy
RXES	Resonant X-ray emission spectroscopy
DOS	Density of states
pDOS	Partial density of states
TICS	Total inelastic counts per second
DFT	Density functional theory
CB	Conduction band
VB	Valence band
HOPG	Highly-oriented pyrolytic graphite
GO	Graphene oxide
ALS	Advanced Light Source
CLS	Canadian Light Source
BL8	Beamline 8.0.1 (Soft X-ray Fluorescence) at the Advanced Light Source
SGM	Spherical Grating Monochromator beamline at the Canadian Light Source
REIXS	Resonant Elastic and Inelastic X-ray Scattering beamline at the Canadian Light Source

Chapter 1

Introduction

Conventional wisdom held that two-dimensional (2D) crystals were not supposed to be stable. If one ever tried to make a 2D crystal, it would buckle, curl, twist, or undergo some other transformation to give it the supposedly necessary third dimension. In 2004, however, that belief was shattered when Novoselov *et al.* discovered graphene: a one-atom thick plane of hexagonally-bonded carbon atoms [1]. The fact that it took until 2004 to find graphene is, in and of itself, somewhat amazing. The first theoretical look at the band structure of graphene was done by Wallace *et al.* in 1947 [2]. Experimental evidence of graphene had been discussed in the literature in 1992, when Land *et al.* reported 'single-layer graphite', as they called it, in their scanning tunneling microscopy (STM) images [3]. Whomever saw it first, Novoselov *et al.* were the first to realize what they had found, and therefore won the Nobel Prize in 2010 for their efforts.

Pristine graphene is a zero-band gap semiconductor, wherein electrons near the Fermi edge behave like massless Dirac fermions due to linear bands [4]. This property is unprecedented. Having an effective mass of 0 has two extremely important results: Firstly, the electrons do not interact with the graphene lattice, which leads to ballistic transport [5]. This basically means that the resistivity of graphene is exceptionally low, which leads to less power lost over the length of a wire made from graphene. The other property is that the electrons conduct through graphene at the speed of light. The conduction electrons in copper at room temperature is roughly 1500 km/s (Fermi velocity, not drift velocity). The conduction speed of graphene is over 5 orders of magnitude better than that of copper. The maximum current density of graphene would of course not be very high, due to the fact that graphene has little volume to hold charge. (Graphene has a 2D crystal structure, not a 2D physical structure. The material still has height due to the non-zero height of the carbon atoms

themselves.) However, if one were to use graphene as an interconnect in an integrated circuit, the processing speed of the device would improve simply because the charge carriers would conduct so quickly [6].

Graphene is a material that has been suggested for use in supercapacitors [7] and as a hydrogen storage medium [8–10]. Given how thin it is, graphene could possibly be used in integrated circuits, as active components as well as interconnects [6]. However, all digital logic devices require two distinct logic states: 'on' (conducting) and 'off' (non-conducting). Graphene fails this very basic measure of merit, because it is an excellent conductor and therefore would always be 'on'. A band gap would solve this problem, because with such a gap, there would be a minimum threshold energy necessary to force charge carriers to begin conducting. The device would thus be in the 'off' state if the energy supplied to the system *via* an external electric field fell below this minimum energy. Finding the best way to introduce such a gap is a subject of tremendous effort by graphene researchers.

One area of unexpected trouble for graphene comes when one tries to use it in solar cells. It is highly transparent, and it has great conductivity, so using as a charge collecting layer in organic photovoltaic (OPV) applications seems like an obvious win [11]. The problem is, OPVs, like all photovoltaic devices, need to separate charge and extract it quickly for the cell to work efficiently. This requires that the energy levels of all of the respective components line up appropriately so as to provide minimal resistance to either the holes or the electrons. Graphene, unfortunately, does not have an appropriate energy level structure because it has a low workfunction, which inhibits efficient charge collection [12]. Oxidizing graphene helps to fix the energy alignment problem, and also makes it more transparent, although doping graphene in this manner will force its band structure to stray from linear [13] It is also soluble in polar solvents, which makes it easy to spin cast or spray on. The cost is much lower conductivity. Graphene oxide has other applications for which it could serve. It functions as a photocatalyst [14], and chemically-reduced graphene oxide has also been suggested as a detector for airborne molecules [15].

Interestingly, the problem of introducing a band gap into graphene may be solved while simultaneously attempting to solve the problem of how to make graphene. The original method used by Novoselov *et al.* to isolate graphene was to place scotch tape on the top of

graphite and peel off the top layer. The 'scotch tape' method, also called the 'micromechanical cleavage' method, is obviously not a cost-effective way to mass produce graphene. One way to make graphene on a large scale is to oxidize graphite in some way so as to place polar functional groups on the graphene sheets. Once this is accomplished, the graphene sheets spontaneously separate if placed water, although other polar solvents can be used [16]. The exfoliated graphene oxide sheets may then be reduced and harvested [17]. The challenge at this point is how then to reduce the harvested graphene oxide sheets to make graphene. Even if it were possible, one cannot simply remove all of the functional groups from graphene oxide, because the functional groups are what is keeping the GO sheets in suspension. However, research is ongoing as to how one may efficiently reduce GO in solution. In particular, diazonium-chemistry based covalent functionalization has been shown to help prevent the aggregation of GO sheets in solution while reducing them [18].

Thus, oxidizing graphite allows one to produce graphene oxide, which can either be reduced to make graphene or used as-is. Either choice leaves one with a desirable product. It is therefore important to develop methods to control the process by which graphene is oxidized, such that the electronic structure of graphene oxide in general, and the band gap in particular, are reproducibly controlled [19]. With pristine graphene functioning as highly conductive and chemically compatible interconnects, a new era of carbon-based electronics may be realized [20]. However, many problems must be overcome before these goals may be realized, not the least of which being able to properly and reproducibly control the electronic and physical structure of graphene oxide. Many have theorized about the structure of graphene oxide and its precursor graphite oxide [21–25], and there have been many experimental studies using various techniques to characterize these materials [26–29]. In particular, X-ray absorption near-edge fine structure (XANES) studies of graphite oxide have been highly useful in elucidating the local electronic structure of the carbon and oxygen sites in graphene oxide [30–34].

Despite the impressive work done on graphene oxide, many questions persist as to the structure of this material. There are two main lines of research that we have pursued: 1) How does one change the electronic structure of graphene, particularly the band gap, to suit the application? 2) How does graphene oxide oxide change with time? The last question

in particular has been of great interest to theoreticians, who have predicted that GO is not stable, either in terms of functional group distribution [35, 36], or in terms of chemical structure [37]. However, the graphene oxide community has been slow to answer in the literature from an experimental perspective. Work done recently to characterize the aging mechanisms in GO show that functional groups spontaneously react together to change the overall chemistry of GO over time [38].

Our manuscript, *Epoxide Speciation and Functional Group Distribution in Graphene Oxide Paper-Like Materials*, deals with both questions simultaneously. One particularly poignant question concerns the bond integrity of the carbon lattice under the strain of functional group bonding. The functional groups, originally attached to the 2D carbon plane to make graphene oxide soluble, may serve to alter the electronic and physical structure of graphene in a variety of beneficial or deleterious ways. The epoxide functional group has attracted special focus because some studies have suggested that this functional group may serve to unzip the C-C σ-symmetry bonds that form the backbone in graphene [23]. Line defects have been visually observed in HOPG [39], and unzipping carbon nanotubes to produce graphene nanoribbons is a very active area of research [40].

The band gap is a highly important parameter of a condensed matter system that affects such disparate macroscopic properties as hardness [41, 42] and electrical conductivity. Although the band gap factors into the conductivity of a sample, it is by no means the only determining factor. After the electron has been promoted into the unoccupied states, charge carrier mobility determines the speed with which the electron moves through the bulk of the sample. There is more than one method of conduction that can occur, and each has repercussions on carrier mobility. For materials that are well-represented by a one-electron, mean-field approach to band theory, any electron (hole) that is promoted into the unoccupied (occupied) states becomes delocalized. However, for highly localized electrons, such as the d electrons in the $3d$ transition metals, a hopping model of conduction is more appropriate [43]. In such a model, charge carriers move from localized state to localized state, rather than within a band. Nevertheless, conduction begins with moving an electron from the occupied states to the unoccupied states. The band gap is therefore a key parameter that one must properly characterize if one is to understand how the material in question will

function as an electronic material.

Two of our papers deal directly with the band gap of GO. These two papers form a series. The first paper, *Modulation of the Band Gap of Graphene Oxide: The Role of AA-Stacking*, studies the role of interplanar stacking order on the band gap of multilayered graphene oxide. We have found, for the first time, that stacking order can play a large role in determining the band gap, and as such, care must be taken when designing the equipment. The second paper, *The Influence of Sample Preparation Methodology on the Band Gap of Graphene Oxide Paper*, uses the concepts built in the first paper to discuss how sample chemistry and stacking order come together to influence the band gap.

Although oxidization of graphite allows for facile production of graphene, the damage to the basal plane is sometimes too high a price to pay for introducing a band gap because it destroys the π-conjugated network that grants graphene its unique characteristics, even after chemical reduction to remove some of the functional groups [44]. Thus, one must either repair the damage to the carbon basal plane [18], or modify the electronic structure of graphene without damaging it, such as by non-covalent functionalization [45]. Our work in the manuscript entitled *Pronounced, reversible, and in situ modification of the electronic structure of graphene oxide via cooling below 160 K*, addresses this possibility. Through cooling, we have found that the advent of amorphous solid water (ASW) can non-covalently functionalize graphene, or lightly oxidized graphene. Although the work focused on graphene oxide, the ASW preferentially attacked those carbon sites that were not bonded to a functional group.

Oddly enough, the electronic structure of graphene oxide is not yet fully understood. Although there is general consensus that the Lerf-Klinowski model is correct, this model describes only the functional groups that are present, and not how they change the electronic structure. We have found that, contradictory to the literature, most of the peaks that arise in the XANES spectrum of GO at energies below 288 eV are actually due to carbon atoms near to, but not bonded directly to, functional groups. These results are detailed in our manuscript entitled *A Reevaluation of the Role of Functional Groups in Modifying the Electronic Structure of Graphene Oxide*. Indeed, the states at 288.4 eV are hotly contested, with the two main interpretations being that these are interlayer states [30], whereas others believe that it is due to functionalization [34, 46]. Many other researchers speak of both

as possibilities [32, 33, 44, 47–49]. Our results show that there is a third, and likely strong, possibility. The 288.4 eV resonance and the 287.4 eV resonance are both strongly influenced by adsorbed atmospheric gasses, most likely water.

The overall theme of the work presented here is to characterize the electronic structure of graphene oxide paper for the purpose of encouraging new avenues of research into device fabrication. GO-based device design for the mass market requires the researcher to understand how to modify the electronic and physical structure to achieve a particular design objective, not only in the short term, but the long term as well. Product longevity strongly impacts its economic underpinnings. Thus, a complete picture of how to alter graphene oxide is a necessary and worthy goal.

Chapter 2

Experimental Techniques

2.1 The Essence of Band Structure

Bringing atoms together to form bonds marks a fundamental shift in how one can visualize the physical underpinnings of a system. This applies not only to how one may model the system theoretically, but how one interprets experimental results. Simple, few-atom systems can be described by molecular orbital (MO) theory, which involves the linear combination of atomic orbitals to describe the bonds between the atoms. However, at the other end of the spectrum lay crystals, each of which is a large conglomerate of a small, repeatable structure, called a unit cell. The framework in which the unit cells are placed is the lattice. This periodic lattice structure has one very important result: the creation of bands, where the energy of an electron with a particular symmetry is dependant upon its crystal momentum vector, $\mathbf{k}$. The energy states that the charge cloud may occupy are no longer discrete steps, but rather form a continuous range (or band). From a spectroscopic viewpoint, the spectra will appear to blur from the discrete states one expects to see in spectra from isolated atoms.

Conceptually, the rise of band structure is a consequence of the fact that electrons are fermions. Fermionic statistics do not allow electrons with the same quantum description (in whatever quantum mechanical picture happens to hold at the time) to exist with the same energy and momentum. Of course, this is precisely the problem that one finds when atoms form a condensed matter system that has a periodic lattice: all of the atoms that share the same site in all of the unit cells have electrons in precisely the same states. Note that this is a problem only for electrons that have the ability to interact with the electrons on neighboring atoms, typically referred to as the valence electrons; strongly bonded electrons that do not form bonds, called the core electrons, do not experience the problem of neighboring electrons

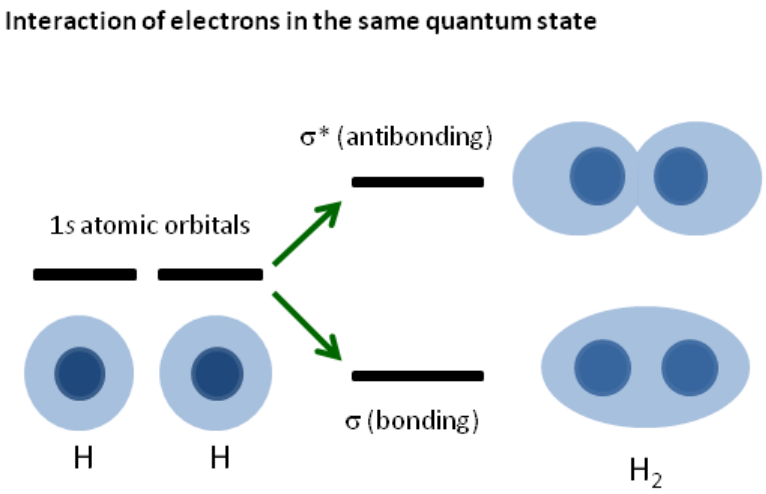

Figure 2.1: Electrons are fermions, and as such, electrons in the same state cannot coexist in the same space. Hence, the system will remove the degeneracy and create new states at new energies that are based upon the original atomic orbitals.

sharing the same state. For the valence electrons, however, something must be done to satisfy the requirements of fermionic statistics.

The solution is to lift the degeneracy. The wavefunctions of the interacting electrons are altered to allow electrons with the same state to coexist in the same space. This is not dissimilar to what happens when atoms of the same kind bond to form molecules, such as what happens with H atoms bond to form H_2, as is shown in Figure 2.1. In fact, the example in Figure 2.1 is instructive if one considers what happens even if the number of atoms in the crystal is only a few thousand (a very small crystal indeed!). If each electron requires its own independent state (two per orbital if one includes spin), then the parent atomic orbitals will split into a indistinguishable group of tightly packed states, separated in energy by undetectable amounts. In the infinite limit, the states will form a continuous band.

The creation of bands is neither a function of unit cell size nor direct interaction, but of periodicity. Bands will still form even if equivalent atoms in neighboring unit cells are too far apart to interact directly. This is because wavefunctions of a particular momentum $\mathbf{k}$ at a point $\mathbf{r}$ in a periodic lattice can be described by Equation (2.1), which was proven by Bloch [50].

$$\phi_{\mathbf{k}}(\mathbf{r}) = u_{\mathbf{k}}(\mathbf{r}) \exp(i\mathbf{k} \cdot \mathbf{r}) \tag{2.1}$$

where $u_{\mathbf{k}}(\mathbf{r}) = u_{\mathbf{k}}(\mathbf{T} + \mathbf{r})$, and $\mathbf{T}$ is the translation vector between equivalent points in neighboring unit cells.

The magnitude of T is irrelevant, and therefore so is the size of the unit cell. The formation of bands is a function of periodicity, not direct interaction between the sites forming the bands, although the shape and character of the resultant band will change based upon the strength and nature of the interaction. Large, low-symmetry unit cells filled with many non-equivalent sites will produce bands that are very flat and relatively featureless. The shape of the bands is of course highly important, because it determines two extremely important observable properties of condensed matter systems. The first is the effective mass m^* of the carriers, defined by Equation (2.2).

$$\frac{1}{m^*} = \frac{1}{\hbar^2} \nabla^2_{\mathbf{k}} \epsilon(\mathbf{k}) \tag{2.2}$$

where ϵ is the band structure (dispersion relation).

One notable result is the effective mass of conduction electrons in a metal. The free electron model holds that the band structure of a metal is parabolic in shape, which returns an effective mass that is the rest mass of a free electron. However, this particular approach fails to account for the effective mass of 0 for graphene. The linear band shape near the Fermi level returns a second derivative of 0, which would make the effective mass infinite. Calculation of effective mass should therefore be done with care. If the band structure allows for the computation of effective mass, then $m*$ also determines the conductivity. For semiconductors, which can have both holes and electrons as charge carriers, the conductivity is given by:

$$\sigma = n_e m_e^* q + n_h m_h^* q \tag{2.3}$$

where q is the elemental charge, n_e and n_h are the densities of electron and hole charge carriers, respectively, and m_e^* and m_h^* are of course the effective masses of the electrons and holes.

The second observable of prime importance is the density of states (DOS), which is related to the band structure through Equation (2.4). The DOS of a system is, as the name might suggest, the density of electronic states, in units of [1/eV], at a particular energy, E.

$$\mathrm{DOS}(E) = \frac{V}{(2\pi)^3} \int \frac{\mathrm{S_E}}{|\nabla_{\mathbf{k}} \epsilon(\mathbf{k})|} \tag{2.4}$$

where S_E is a surface area element on a constant energy surface of the three dimensional band structure, and $\nabla_{\mathbf{k}} \epsilon(\mathbf{k})$ is the gradient of the band structure with respect to $\mathbf{k}$.

Given that the DOS arises from the band structure, and the band structure is highly dependent upon interactions between atoms, the DOS of system gives very detailed information about the bonding environment that each non-equivalent site experiences. Depending on the particular experimental apparatus one uses, measuring the DOS thus informs one about chemical interaction, the degree of order in the physical structure, local site symmetry, defect structures, magnetic ordering, and more. In the context of the above discussion, measuring the DOS also helps one determine the conductivity of the sample. The carrier concentrations n_e and n_h strongly depend upon the DOS.

The DOS is a quantity that is highly useful for characterizing a sample. How, then, may one measure the DOS? There are a number of different techniques, but two very powerful techniques are X-ray absorption near-edge spectroscopy (XANES) and X-ray emission spectroscopy (XES), which allow one to probe the unoccupied and occupied partial density of states (pDOS), respectively.

2.2 X-ray Absorption Near-Edge Spectroscopy

X-ray absorption spectroscopy (XAS) is an umbrella term that covers a number of different specialized spectroscopic techniques that all have one thing in common: an X-ray photon impinges upon the sample and is absorbed by the electron cloud. The energy and momentum of this photon is then used to induce an electronic transition in which the electronic cloud is put into an excited state from its ground (or rest) state. Considering electrons from a more classical single electron model, one can visualize such a transition as forcing a bound electron to move into an unoccupied state. If the core electron is promoted into a higher

energy state, but is still bound to the atom, the energy required to induce this promotion is called the transition energy of that electron. If the electron is supplied with sufficient energy to be promoted to continuum (or vacuum) states, then the electron has become unbound from the atom; the minimum energy required to do this is the binding energy.

One should note that, when dealing with condensed matter, the meaning of 'binding energy' can sometimes be ambiguous. In many condensed matter systems, some, if not all, of the normally-unoccupied bands have strong dispersion and low effective mass. Consequently, an electron promoted into such a band becomes highly delocalized. This means that, although the electron is still bound with the *material*, it may no longer be bound to the *atom* from which it originally sprung. Hence, it is common in the literature, particularly among X-ray photoelectron (XPS) spectroscopists, to refer to the energy required to promote an electron into a bound-yet-delocalized conduction band state as the 'binding' energy.

Although the X-ray absorption process can occur, in principal, for any bound electron, the probability that a particular electron will be 'chosen' for promotion rises dramatically if the energy of the photon coincides with the transition energy of that electron. This is called resonant excitation. The binding energies of core electrons vary greatly between the elements, which allows the XAS spectroscopist an ability to choose which atom he or she would like to excite independently of the rest of the compound. Couple this natural advantage of all X-ray based techniques with the brightness and tunability of synchrotron light sources [51], and one has a powerful tool for probing the electronic structure of any compound one might imagine.

Different excitation energy ranges give different information about the structure of the material. The range near the edge provides information largely about the electronic structure of the sample, and XAS spectra measured in this region is called X-ray absorption near edge spectroscopy (XANES). XANES probes the unoccupied partial density of states (pDOS). The unoccupied descriptor comes about because of Fermi's Golden Rule, shown below in Equation (2.5) [52]. In short, the equation tells us that the transition rate for an electron to be promoted into an occupied state (which is proportional to the absorption spectrum) should simply be the density of states in the final state ρ accessible by the transition, modified by the transition probability from the initial state $|i\rangle$ to a set of final states $\langle f|$. The final

density of states in resonant absorption differs from the ground state only in that there is an electron in the conduction band; hence, the unoccupied states are probed. There is also a hole in the core level, which can be problematic for analysis because the unmasked electrostatic potential from the nucleus, as well as the coupling of the N-1 core shell to the unoccupied states, can distort a XANES spectrum significantly. This is typically referred to as the core hole effect.

$$T_{i\to f} = \frac{2\pi}{\hbar} \left|\langle \Psi_f | H' | \Psi_i \rangle\right|^2 \rho_f \tag{2.5}$$

The transition operator for X-ray absorption is the electric dipole operator. Using the dipole transition operator is actually a simplification, as the expansion of the field description of a photon has higher components, such as electric quadrupole and magnetic dipole. However, the contribution of these higher order terms to the overall electronic transition probability are typically much smaller than the dipole contribution, and in any event, all terms higher than dipole symmetry are completely irrelevant in light atoms such as carbon (the main constituent atom in graphene). This is because each component in the multipole expansion has an associated quantum number describing its angular momentum. The dipole component has a momentum quantum number of 1, quadrupole has 2, etc [53]. The X-ray absorption process has to conserve momentum, which effectively means that all quantum numbers must be accounted for; absorption of a dipole symmetry photon must produce a transition wherein the promoted electron experiences a change in momentum corresponding to $\Delta l = \pm 1$. Thus, when exciting $1s$ electrons in carbon, only the dipole component of light has the correct momentum to promote these core electrons into the p-symmetry unoccupied bound electronic states.

The 'partial' descriptor in 'partial density of states' comes about because of the aforementioned chemical specificity of resonantly exciting core electrons at only one atomic site. Coupled with the fact that XANES probes the unoccupied states as just discussed, the core electrons at any given site are preferentially excited into the unoccupied states that are associated with that site. In a compound where there is a very high degree of hybridization between sites, XANES spectra taken from the each site will share a lot of the same characteristics. However, this will not be the case in compounds where electrons tend to be highly

localized, such as in highly correlated systems.

Now that the basic physics of X-ray absorption spectroscopy has been established, the problem is how one may actually measure a spectrum. If one can manufacture a thin enough sample, it is possible to measure the radiation that passes through the sample and measure the radiation intensity that has not been absorbed as a function of incident photon energy. If one subtracts this measurement from the known incident light intensity, then this produces an X-ray absorption spectrum. The incident and transmitted light intensities (I_0 and I_T, respectively) are additionally related through the Beer-Lambert law, given in Equation (2.6).

$$I_T = I_0 \exp -\sigma l N \tag{2.6}$$

where σ is the absorption cross-section, l is the path length of the radiation, and N is the number density of absorbing atoms. Note that, in the derivation of this formula, no assumptions are made concerning the physics behind σ, so the Beer-Lambert law applies in both resonant and non-resonant cases.

Assuming that I_0 and I_T have been measured appropriately, the absorption cross-section σ can then be directly extracted from the measured data. However, in the soft X-ray regime, where the core hole binding energies of organic materials (C, N, O) are located, it is very difficult to manufacture a sample thin enough due to the very short attenuation length of soft X-rays in matter. Thus, XANES spectra must usually be measured indirectly by counting secondary particles, either photons or electrons, that are emitted from the sample as a result of core hole decay. Because I_T is not directly measured but only inferred, the true absorption cross section σ can only ever be known, at best, to within a constant factor.

2.2.1 Total Electron Yield

When an electronic system has been perturbed by an absorbed photon, the system is necessarily unstable. To restore stability and shed the excess energy, an electron in a higher-lying state can collapse into the core hole and annihilate it. The released energy can then be transferred from the system by either emission of a second photon or ejection of an electron. Photon emission is called radiative decay, and it will be discussed later. The second option,

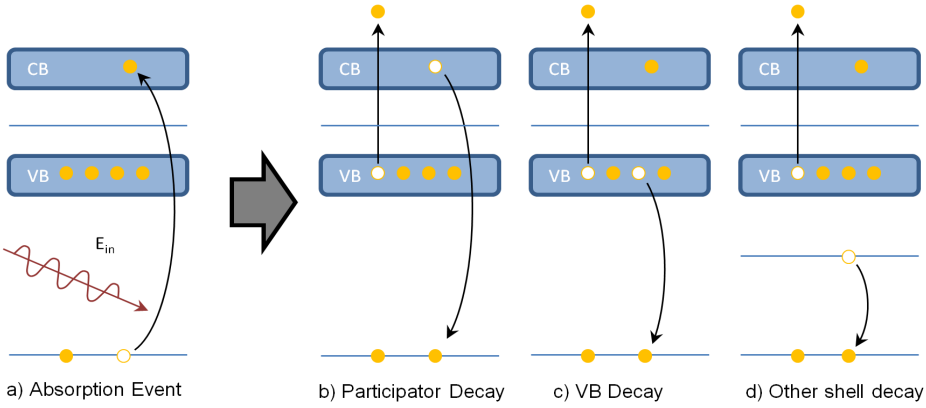

Figure 2.2: Auger decay possibilities. Part a) shows the initial X-ray absorption process. The excess energy is then shed through b) the original participator electron decaying from the conduction band (CB) back down to the core level and transferring the energy to a valence band (VB) electron, or c) a valence electron fills the core hole, or c) an electron from an intermediate core level refills the core hole. This last possibility does not exist in second row elements like carbon.

ejection of an electron, occurs when the energy released by the decay of a core hole is transferred to another electron in the system, which is then ejected from the atom. This process is called Auger decay. The concept of Auger decay is shown graphically in Figure 2.2.

If the energy released by the core hole decay is imparted to a valence electron, then the electron has much more than enough energy to break free of the atom and, if it makes its way to the surface, overcome the work function of the material and escape into free space. Of course, as more and more Auger electrons leave, the sample begins to build up positive charge. If one connects the sample to ground through a sufficiently sensitive ammeter, then one can measure the current flowing from ground to the positively charged sample, as shown in Figure 2.3. Of course, the current will flow more strongly if the sample is more positively charged, which is directly proportional to the number of electrons being ejected from the sample, and thus the number of core holes being created as a function of excitation energy. A TEY spectrum is therefore proportional to the absorption cross section.

TEY has two key limitations. The obvious one is the conductivity of the sample. An

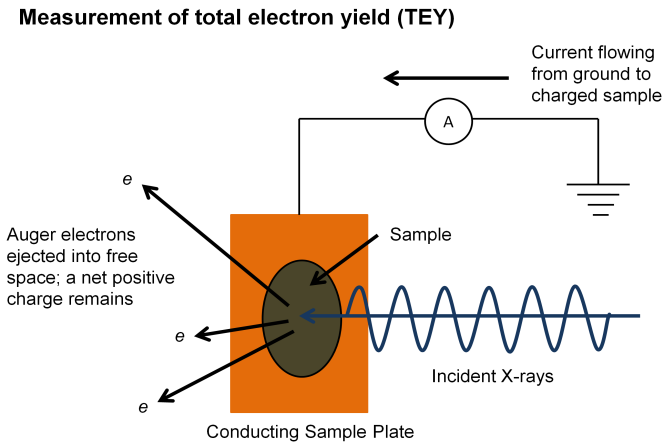

Figure 2.3: Measurement of total electron yield. The ejected Auger electrons leave behind a positively-charged sample. If connected to ground, the neutralizing current flowing into the sample is proportional to the time-averaged Auger electron creation rate, which is equal to the core hole creation rate.

insulating sample will not allow the electrons to be replaced by the ground wire as fast as they are being removed *via* Auger decay, which can lead to a distorted spectrum because the building positive charge will make it increasingly more difficult for Auger electrons to escape the sample. This problem is referred to as sample charging. The easiest way to mitigate this is to utilize surface conduction; the dangling bonds at the surface will allow electrons to hop. This can either be accomplished by attaching conductive wires to the surface, or by simply increasing the surface area by grinding the sample into a powder.

The other limitation is unfortunately inherent to the matter in which electrons interact with the matter around them. Electrons, even ones with hundreds of eV in kinetic energy, have very short mean free path lengths through the bulk of the crystal. Typically in the soft X-ray energy regime, one cannot expect electrons deeper than 10 nm to successfully escape the sample [54]. This means that the surface states will have a very large influence on TEY spectra. This problem can be mitigated somewhat by applying a large positive bias to the sample *via* an external electric field. This will supply more energy to electrons heading to the

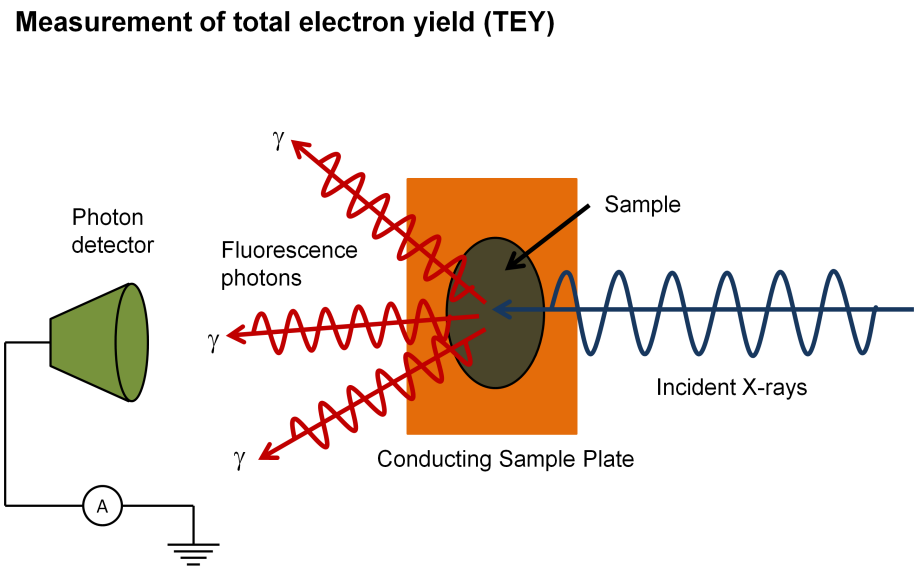

Figure 2.4: Measurement of total fluorescence yield.

surface, and will help to extend their escape depth. The short mean free path length is not a problem outside of the realization that care must be taken to ensure that the surface and the bulk are mutually representative. Otherwise, *in situ* surface cleaning may be necessary, or a more bulk sensitive X-ray absorption measurement technique must be used.

2.2.2 Total Fluorescence Yield

Total fluorescence yield (TFY) is a measurement technique that involves counting photons that are emitted from the sample as core holes decay. Note that this could also be done for TEY by integrating all of the electrons emitted from the sample, but this is not usually done unless the equipment for detecting electrons is already a part of the experimental apparatus, such as an electron spectrometer for XPS measurements. Counting photons is typically done by placing a detector near the sample which is sensitive to the photons in the energy range in question, as is shown in Figure 2.4.

The photon detector in use at a beamline is typically either an electron multiplier or a photodiode, each with its own unique advantages and caveats. The electron multiplier functions by detecting the avalanche of charge generated by an incident particle. When used as a photon detector, the avalanche has to be started by vacuum photoemission of an electron, so electron multipliers are only sensitive to ionizing radiation. This allows the electron multiplier to work with visible light in the chamber, unlike a photodiode. Photodiodes work not by charge avalanche, but by separation of bound excitons which can be created by visible light. Thus, a XANES measurement performed in TFY mode, using a photodiode, must be done in complete darkness lest stray light completely swamp the signal of interest. Although photodiodes may be sensitive to light, they are not sensitive to charged particles. The change avalanche in an electron multiplier may be started by an incident ion or electron. This means that electron multipliers, if used for TFY, must have a strong negative bias to repel the Auger electrons that are streaming out of the sample along with the photons of interest. An electron multiplier without strong enough shielding will count electrons as well as photons, meaning that the desired TFY signal will be contaminated with the TEY signal.

Given that florescence photons only emerge when a core hole is refilled, the implicit assumption that one makes while performing a TFY measurement is that the number of photons emerging from the sample is directly proportional to the number of core holes being created, and hence the absorption coefficient. TFY is more bulk sensitive because photons can penetrate through much more material than electrons, which means that the emitted photons can escape from much deeper. TFY is also not subject to sample charging, so the conductivity of the sample is not an issue. However, TFY suffers from two problems that TEY does not: saturation and self-absorption [54].

2.2.3 Partial Fluorescence Yield

PFY is also a photon-counting technique, like TFY, however the experimentalist chooses to count only those photons emitted from the sample that fall within a certain energy range. TFY and PFY often give very similar spectra, for the simple reason that most of the photons emitted from the sample will originate with the element that is being resonantly excited, and thus greatly overwhelms all other spectral signatures. However, there are some cases where

this is not the case.

One such case occurs when one cannot help but to resonantly excite more than one edge at once. This is the case with carbon and oxygen, because the O 1s and C 1s thresholds, at 550 eV and 290 eV respectively, differ in energy by roughly a factor of 2. Consequently, when tuning the beamline to resonantly excite on the C 1s threshold, second order contamination (X-rays with twice the energy that pass through the monochromator at the same angle) resonantly excites the O atoms as well. The percentage of the total number of photons hitting the sample that are second order contamination differs based on the quality of the beamline instrumentation, but it is typically less than 5%. Therefore, TFY spectra measured from compounds with roughly even number of C and O sites, such as GO, are mostly due to counting C Kα photons. In the manuscript *Modulation of the band gap of graphene oxide: The role of AA-stacking* detailed in Chapter 5, we could not measure the fluorescence yield of the multilayered pristine graphene samples in TFY mode, because the graphene samples were mounted on SiO_2 substrates. The vastly larger number of O atoms in the substrate ensured that O Kα fluorescence yield from the substrate competed strongly with the C Kα fluorescence yield from the graphene.

The solution to this problem involves counting the C Kα photons only. In theory, one could use a spectrometer for this task. Instead of using the imaging device to record the spectrum as a function of emitted energy, as one one do if measuring an XES spectrum, one need only integrate all of the counts and record the integrated intensity as a function of excitation energy to receive a PFY spectrum. In practice, this will not work for the graphene/SiO_2 sample system either, for much the same reason as why there is second order contamination in the first place: Photons at double the energy can pass the grating of the spectrometer at the same angle, which means that the emitted O Kα photons will also be counted by the detector.

One therefore needs a detector that can differentiate between photons of different energies, but does not use diffraction from a grating to achieve it. One such detector is a silicon drift detector (SDD). An SDD differentiates photons based upon the degree of ionization that they create as the pass into the detector. An SDD therefore distinguishes O Kα and C Kα photons *via* a solid state effect, rather than diffraction. The experimental broadening is extreme -

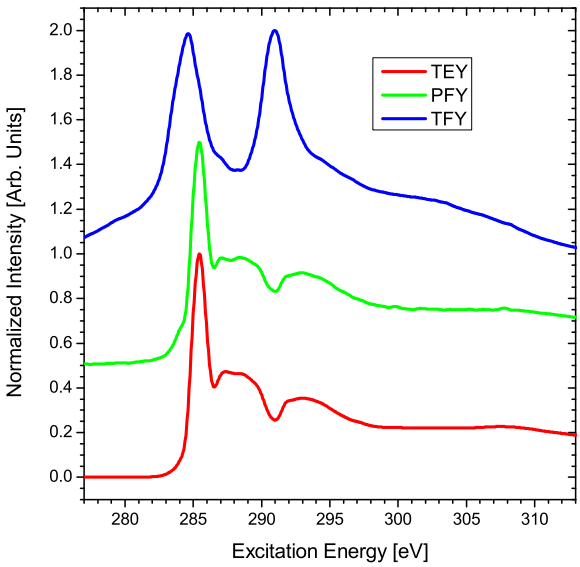

Figure 2.5: Comparison of TEY, TFY, and PFY measurement modes for C 1s XANES of graphene on SiO_2 substrate. The angle of incidence was 80°.

over 100 eV full width at half maximum (FWHM) - which makes an SDD grossly unsuitable for recording an XES spectrum. However, it is more than sufficient to tell an O Kα photon from a C Kα photon. The apparatus for measuring PFY is not conceptually different from Figure 2.4, except that the detector produces a spectrum rather than a number at a given excitation energy.

A comparison of the TEY, TFY, and PFY measurement modes is shown in Figure 2.5. The sample was single layer graphene on an SiO_2 substrate. The spectra were measured as the sample was resonantly excited across the C 1s threshold. As one can see, the PFY and TEY spectra are very similar, as one would expect given that the sample only exists at the surface. The TFY spectrum is, however, completely swamped by the O Kα photons, and is thus meaningless.

2.2.4 Saturation and Self-Absorption

Saturation is a problem that arises when the excitation energy of the photons with which one is exciting the sample begins to approach a very strong resonance feature. As the excitation

energy approaches resonance, the cross-section of the site grows drastically, and thus the site absorbs photons more and more efficiently. If the site being excited happens to be the dominant atomic species, and the resonance is very strong, then eventually the cross-sections grow big enough that nearly all of the photons are being absorbed. At this point, if the cross-section continues to grow at the next incremental excitation energy, no more new core holes are created despite the increased cross-section because all of the photons are already being absorbed. Saturation thus has the effect of stunting the growth of high-intensity features, and brings all features closer in relative height. Saturation cannot change relative peak heights, but can severely distort the integrated peak intensities. Because saturation is a bulk effect - the cross-sections of all the resonantly-excited sites adding together to absorb all the incoming photons - it is not an issue for XANES measurements of impurities and/or dopants, provided that the concentration is low enough.

An instructive way to visualize this problem is to think of the TFY spectrum as the penetration profile. In particular, if one subtracts the absorption spectrum (after proper normalization) from the background penetration depth, then one receives the modified penetration depth as a function of energy. Figure 2.6 shows an illustrative example of how this would look. The absorption spectrum is supposed to represent the aggregate cross-section of the sample. Obviously, the penetration depth cannot exit the surface, so as the surface gets closer, the decrease in penetration depth and the increase in the cross-section are no longer directly proportional to one another, and the TFY spectrum is saturated.

Note that TEY is immune from saturation because the atoms that successfully emit Auger electrons from the sample are all very near to the surface. The number of atoms near enough to the surface is a small fraction of the overall number of atoms accessible by the incident X-rays, and they are the first to see the incoming radiation. These surface atoms can therefore always absorb as much as possible. As saturation takes over, the deeper-lying atoms will be the ones that become starved for light.

The immunity of TEY to saturation exists because the escape depth of the electrons is shallow, and is not intrinsically related to the Auger process. With this in mind, it is therefore possible to mitigate the effects of saturation by choosing an appropriate experimental geometry, i.e. the positions of the source and detector relative to the sample surface nor-

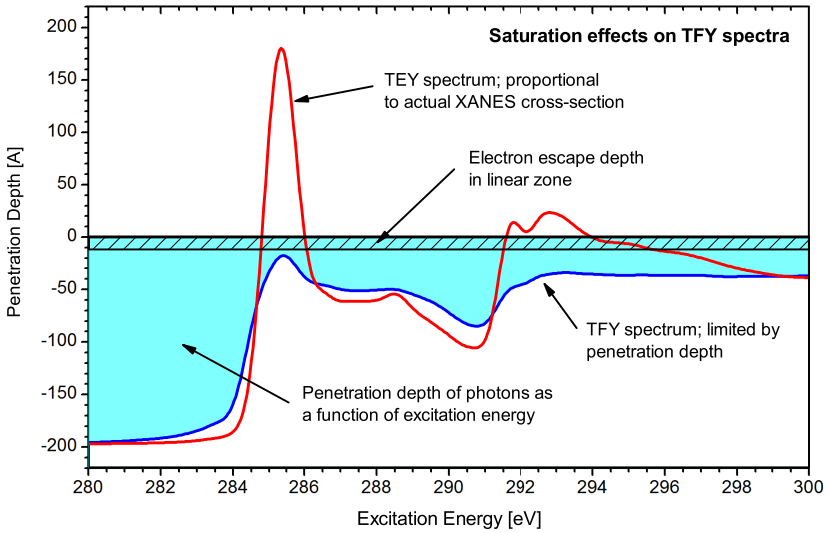

Figure 2.6: Penetration depth of incident photons as a function of excitation energy. The spectra are measured TEY and TFY spectra of HOPG. The TEY spectrum represents the how the true absorption cross-section changes with energy, but the penetration depth cannot be negative. Hence, the TFY spectrum gets cut off a energies with strong resonances.

mal. A good choice would maximize the penetration depth while minimizing the volume of material emitting photons. Such a geometry would be one with normal incidence for the incoming radiation (the incident propagation vector and the sample normal are parallel), with grazing incidence for the emitted radiation (the detector surface normal and the sample surface normal are nearly perpendicular). The normal incidence angle would drive the incoming radiation deeply into the sample, while the grazing emission angle would mean that only atoms very near to the surface can emit radiation that will be measurable by the TFY detector. Of course, just like with TEY, such a measurement will be very sensitive to surface states, but it will be relatively free of saturation. Of course, the opposite experimental setup, a near-grazing incident angle and a near-normal detection angle to nearly normal, will maximize saturation.

In addition to saturation, self-absorption can also be a problem for TFY measurements. After an atomic site emits a photon, that photon must travel through the bulk of the sample that lies between the emitting atom and the fluorescence detector. These photons can be

absorbed on the way, hence the name self-absorption. However, the probability with which a photon will be re-absorbed obviously depends strongly upon its energy. A photon emitted by a valence electron filling a core hole *via* normal emission will have an energy that is below the minimum energy necessary to excite a core electron into the unoccupied states, and hence cannot be resonantly reabsorbed. The emitted photon can be absorbed, but the probability that this will happen will be determined by the pre-edge (background) cross-section. The background cross-section is typically not very large, and is constant regardless, so normal X-ray emission from the conduction band will be unperturbed by self-absorption. The elastic peak, which is produced when the original core electron refills the core hole, and scattered X-rays in systems where resonant inelastic scattering occurs, do however have the energy necessary to be resonantly re-absorbed. For reference to resonant inelastic scattering, please see the section on X-ray emission spectroscopy in Section 2.3.3.

Saturation and self-absorption are highly important considerations when performing K-edge spectroscopy on anisotropic samples, such as graphene oxide. As will be discussed later, the angle with which one excites a sample has a strong impact on how efficiently an unoccupied state is populated through resonant excitation, independent of excitation energy. The dichroic ratio, which is a measure of how flat a layered sample is, requires an accurate measure of the relative intensities of in-plane and out-of-plane excitations [32]. Saturation in particular will distort this ratio. Even from a qualitative standpoint, care must be taken when evaluating the response of a system. Grazing incidence significantly worsens saturation, for two reasons. First, grazing incidence more efficiently excite out-of-plane states, which means a greater cross-section and more shallow penetration depth. Second, as has been mentioned, grazing incidence worsens saturation in general. Thus, features that were small at normal incidence in a TFY spectrum, yet seem to grow strongly at grazing incidence, may not actually be aligned out-of-plane. It may simply be a false conclusion brought on by much stronger saturation (read: suppression) of the rest of the TFY spectrum.

2.3 X-ray Emission Spectroscopy

X-ray emission spectroscopy (XES) is, much like XANES, an umbrella term that can mean different things depending upon the context. However, the common thread is that all XES techniques measure the photons emitted from the sample as a function of energy by passing the X-rays through a spectrometer. The three divisions of XES that are of concern here are non-resonant X-ray emission spectroscopy (nRXES), resonant X-ray emission spectroscopy (RXES), and resonant inelastic X-ray scattering (RIXS). As we shall see, the three techniques differ mostly in terms of how the electron, newly placed in the unoccupied states, interacts with the rest of the system.

2.3.1 Non-resonant X-ray Emission Spectroscopy

Non-resonant X-ray emission spectroscopy (nRXES) is performed by exciting the sample significantly above resonant threshold, on the order of 15 to 20 eV. When one excites in this energy range, the core electron is promoted into continuum states and is no longer bound. If the atom originally had N electrons before excitation, then the final state is an $N-1$ system with a hole in the valence band after a valence electron has refilled the core. Much as placing an electron in the unoccupied states in the final state of an X-ray absorption event allows one to probe the unoccupied states, so too does placing a hole in the occupied states allows one to probe them. This is simply a consequence of eq. (2.5), only energy is being shed rather than be absorbed.

Because the excitation energy is above threshold, there is no preferential absorption by any particular non-equivalent site of the atom being excited, although photons will still be preferentially absorbed by the core level of the atom with binding energy that is closest to the excitation energy. In graphene oxide, for example, exciting the sample at just above the C $1s$ threshold will still preferentially create core holes on the C sites rather than O sites, although little distinction will be made between functionalized and non-functionalized carbon. Because all non-equivalent sites are treated equally, nRXES probes the sum of all occupied C pDOS.

2.3.2 Resonant X-ray Emission Spectroscopy

Resonant X-ray emission spectroscopy (RXES) measurements are performed by measuring emission spectra while resonantly exciting electrons into bound conduction band states. Note that, in this context, 'bound' means that the electron is bound within the material, but not bound to the atom with the core hole. The electron thus becomes highly delocalized, and it is therefore highly probable that the electron can be found on other sites within the crystal. This delocalization of the electron allows it to interact with the system as more as a static background charge rather than a dynamic part of the local crystal states. When a valence electron refills the core hole and a photon is emitted, the final state of the site being excited is $N-1$, with a hole in the valence band and a delocalized electron in the background. From this point of view, RXES and nRXES have much in common.

The difference between nRXES and RXES is site selectivity. Because one is resonantly exciting the sample, it is possible to selectively excite, within the same crystal, sites of the same atomic species that have different local symmetry (called non-equivalent sites). Core holes will be preferentially created on only one non-equivalent site, so RXES probes only the local occupied pDOS of the resonantly excited site, rather than the sum of the pDOS from all non-equivalent sites as in nRXES. This can be a very fruitful technique when used on carbon-based molecules and crystals, because the various non-equivalent sites can have widely varying transition energies that allow the experimentalist to predominantly excite one site at a time [55, 56]. The RXES spectra that result can thus give detailed information as to the occupied electronic environment surrounding each site.

Obviously, taking the time to measure the occupied pDOS of each different site is only useful if there are different non-equivalent sites to probe. Highly homogenous samples will typically not show much difference between a given RXES spectrum and the nRXES spectrum. However, the structure of graphene oxide is not well-ordered, and the carbon atoms that are bonded to different functional groups can potentially show widely varying occupied and unoccupied pDOS. RXES was therefore used extensively - and fruitfully - in the graphene oxide research that will be discussed later in this report.

2.3.3 Resonant Inelastic X-ray Scattering

Resonant inelastic X-ray scattering (RIXS), like RXES discussed above, occurs when one resonantly excites the sample. In the final state of RIXS, there is a hole in the valence band and an electron in the conduction band, like in the final state of RXES. Unlike with RXES, however, the electron in the conduction band is not a delocalized background charge, but is still very much a defining part of the local electronic structure. RIXS is also a one-step process; the excitation and decay steps are coupled through the Kramers-Heisenberg formula shown below as Equation (2.7), which describes the intensity $I(\omega, \omega')$ of the emitted spectrum as a function of the excitation energy.

$$I(\omega, \omega') = \sum_{|\phi_f\rangle} \left| \sum_{|\phi_n\rangle} \frac{\langle f|\hat{d}|\phi_n\rangle\langle n|\hat{d}|\phi_i\rangle}{E_i - E_n + \hbar\omega + i\frac{\Gamma_n}{2}} \right|^2 \delta\left(E_i - E_f + \hbar\omega - \hbar\omega'\right) \tag{2.7}$$

where ϕ_i, ϕ_n, and ϕ_f denote the initial, intermediate, and final states, respectively; E_i is the energy of ϕ_i and E_f is the energy of ϕ_f. The incoming and outgoing photons are denoted by ω and ω'. As the energy difference between the initial and intermediate states approaches the excitation energy, the denominator becomes very small allowing for resonant excitation to occur. The intermediate lifetime broadening, Γ_n, functions to keep the denominator from going to zero on resonance. Its physical interpretation is that there is some uncertainty as to exactly what energy the system is at in the intermediate state.

RIXS is a one-step scattering process. The energy needed to induce the net transition i to f, which has a hole in the valence band and a locally bound electron in the conduction band, is subtracted from the energy of the incident photon. This property gives RIXS peaks the unique characteristic that they track with the excitation energy, as long as the intermediate state can be resonantly accessed by the impinging radiation field. This property thus makes differentiating RIXS and RXES features very easy, as is shown in fig. 2.7. Note that this is the case if the same net transition occurs at each excitation energy. However, RIXS must obey conservation of crystal momentum, so the energy subtracted from the incident photon energy can change (i.e. the RIXS peak will move even on the energy loss axis) if the peak is tracking the band structure [57].

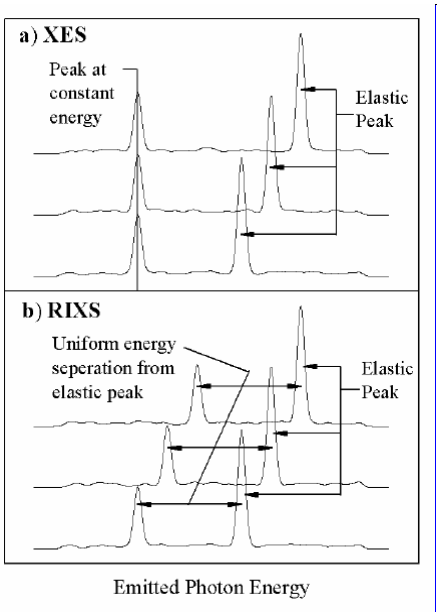

Figure 2.7: RIXS peaks track with the excitation energy, as shown in panel (b), whereas regular emission lines remain constant irrespective of the excitation energy.

Note that RIXS distorts XANES spectra, when measured in some fluorescence mode (TFY or PFY). This is because the probability of the event occurring depends upon transition matrix elements from the intermediate state to the final state in addition to the transition matrix elements from the ground state to the intermediate state (final state in simple absorption). Additionally, RIXS spectra track with excitation energy. As one increases the excitation energy, the high-energy portions of the inelastic section of the RIXS spectrum may have sufficient energy to drive another resonant core hole excitation event as the radiation cone propagates out through the material. The new core hole excitation, which obviously is at a lower energy, will add spectral weight to the lower end of detected spectrum. Such an event can distort a spectrum by subtracting spectral weight from higher-energy portions of the spectrum and placing them, instead, in lower-energy spectral features.

2.4 Geometrical Selection Rules in K-shell X-ray Spectroscopy

Angular dichroism is a well-known effect in graphite and other organic compounds that are based upon aromatic carbon rings, and is used often to determine the orientation of molecules when making thin films. Measurements that show angular dichroism are displayed in Figure 2.8, which shows nRXES and XANES measurements of HOPG at with angles of incidence of 30° and 60°. In this case, the angle of incidence is the angle between the normal of the sample surface and the propagation vector of the impinging radiation. Angular dichroism arises because the electric field vector of the dipole component of light, with a momentum quantum number of 1, couples directly with the p-symmetry unoccupied states. In the final state of the excitation process that dictates transition probabilities, the newly half-filled p-symmetry antibond is an oscillator with an angular momentum quantum number of 1. As a result, even if the photon energy is correct for resonant excitation into an unoccupied state, the transition probability will suffer if the final p-symmetry state and the electric field vector of the incident x-ray are not perfectly aligned.

X-ray fluorescence is the same process as X-ray absorption, only time-reversed, so the same logic applies. The emitted radiation field is at a maximum when the electric field vector of the outgoing photon is aligned with the newly half-emptied p-symmetry bond from which the electron that refilled the core hole originated. The emitted intensity is 0 perpendicular to the same p bond. In short, the outgoing radiation field assumes a dipole-symmetry shape. The reason why this is significant is that the endstation at Beamline 8.0.1, where the data were measured, has the spectrometer that detects the outgoing radiation field at 90° to the incident radiation vector. This leads to the curious state where, at an angle of incidence of 30°, the incoming radiation field couples most strongly, geometrically speaking, to the in-plane antibonding states, but the outgoing radiation field that is detected by the spectrometer most strongly is produced by the out-of-plane bonding states.

This perhaps counterintuitive pattern is demonstrated quite clearly in Figure 2.8. Simulated C pDOS are also shown in this Figure to elucidate which states contribute to the main

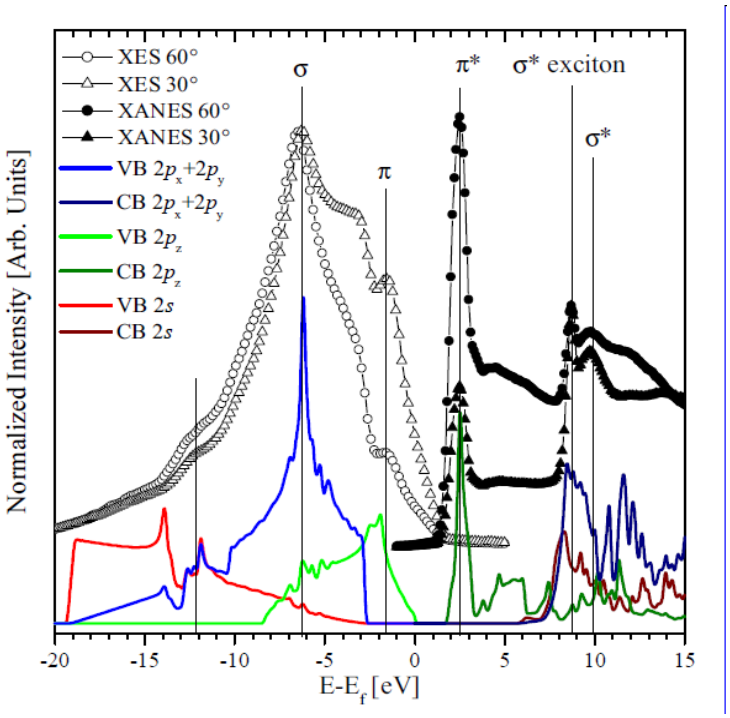

Figure 2.8: Geometrical selection rules for K-shell X-ray spectroscopy are shown using nRXES and XANES (measured in TEY mode) data measured on HOPG. nRXES and TEY spectra were measured at 60° and 30°. The spectra were normalized to the same σ-symmetry bond for both the nRXES and TEY. The features, labeled by either σ or π depending on the local symmetry, scale differently depending on the angle of incidence. DOS simulations of graphite were calculated using WIEN2k, a DFT code, and they show that the σ and π features are due to asymmetric bonding environments that are 90° with respect to one another.

spectral features. It is clear from this very simple experiment that higher angles enhance the π^* feature in the XANES spectrum, a feature which is composed entirely of out-of-plane states. Simultaneously, the π feature, which is also composed of out-of-plane states, is suppressed in the XES spectrum. The angle of the carbon plane determines how efficiently the unoccupied states are populated, but it is the angle of the spectrometer with respect to the detector that determines the prominence of particular features in the measured XES spectrum. For anisotropic crystals where the $\hat{z}$ axis is the unique axis, the polarization scales as $3/2\cos^2(\theta)$ [58].

2.5 Details of the Experimentation Equipment

2.5.1 Beamline 8.0.1: Soft X-ray Fluorescence

The RXES measurements on the carbon and oxygen K edges were performed at Beamline 8.0.1 (BL8) at the Advanced Light Source at the Lawrence Berkeley National Laboratory using the soft X-ray fluorescence (SXF) endstation [59]. Emitted radiation was measured using a Rowland circle type spectrometer with a large spherical grating and a photon-counting area detector. The total experimental resolution 0.30 ± 0.05 eV FWHM, with some variation expected between experiments. The fluorescence measurements were made using a depolarized configuration, which means that the vector E of the incidence beam lies at the scattering plane, i.e. p-polarization was used. The SXF endstation is configured such that the path of the emitted photons that can be detected by the spectrometer and the incident beam are perpendicular to each other.

Although uncommon, a few C K and O K XANES spectra reported in this thesis were measured at BL8. Any that were measured at BL8 were done chiefly in total electron yield mode. All C K and O K XANES spectra measured at the ALS were normalized to the current generated in a highly transparent gold mesh upstream of the sample.

2.5.2 Spherical Grating Monochromator

High-resolution XANES spectra on the C K edge were measured at the Spherical Grating Monochromator (SGM) beamline at the Canadian Light Source. In terms of resolution, the only adjustable parameter is the width of the exit slit, which was typically set to 25 μm, which on the SGM gives an experimental resolution of about 0.1 eV. The XANES spectra were always measured in both total electron yield and total fluorescence yield modes.

Typically, XANES spectra are measured in a stop-start method. The necessary optical components (typically the monochromator grating and exit slit) are moved in angle and position through a increment that corresponds to a particular step in energy. Once the motors have finished moving, counts are integrated for a set period of time before the optics are moved to the next energy. Although this method is well-known and well-accepted, it is

time consuming. The SGM beamline is capable of measuring TFY and TEY in fast scan mode, or slew scan mode. In such a mode, the optical components are moved continuously, and data is collected as quickly as the detectors can read out information. This requires that response of the beamline optical components are well-characterized, and requires precise timing of all of the movements. However, once this is accomplished, scans that take 15 minutes can be measured in 20 seconds.

Measuring in fast scan mode obviously has its downside. The spectra are usually a lot noisier, although the large number of data points mean that the data may be easily smoothed without compromising the quality of the spectrum. However, with the dramatic increase in efficiency, multiple subsequent scans can be done and averaged together to improve the signal-to-noise (SNR) ratio. Additionally, fast scan mode allows for one to study radiation damage directly. If the signal is strong enough that each subsequent scan can be analyzed on its own, then one can track how the spectrum of the sample changes after each 20 second exposure. Fast scan mode was used to acquire the spectra that forms the core of our findings in our manuscript, *Pronounced, reversible, and in situ modification of the electronic structure of graphene oxide via cooling below 160 K*, which is discussed in Chapter 6.

The SGM beamline is also capable of measuring partial fluorescence yield (PFY) scans. The beamline uses an SDD to measure the spectrum of emission lines from a sample. As was mentioned in Section 2.2.3, the SDD in operation at the SGM has an experimental broadening over 100 eV FWHM, so its only use is to distinguish between elemental emission lines. The SDD can be used to differentiate between C Kα and O Kα lines, and can also distinguish between O Kα and the Lα,β from transition metals.

SGM C 1s XANES data are not normalized to an upstream mesh, like at BL8, although it is still used to normalize he O 1s XANES spectra. The reason for this is that carbon contamination at the SGM beamline is quite pronounced for a variety of reasons. When carbon contaminates the gold mesh, and one wants to perform a C 1s XANES experiment, the current extracted from the mesh is no longer an accurate representation of actual beam flux hitting the mesh. This is because the carbon on the mess removes too many photons from the incident beam due to resonant excitation. Although this typically produces a very strong I_0 signal, the I_0 spectrum gives a measure of how well the incident light reacts with

the carbon on the mesh, and therefore the spectrum is a confluence of the chemical nature of the carbon contamination of the mesh with the intensity of the incident beam. The spectrum is no longer representative of the light that passed through the mesh. In other words, using a highly contaminated mesh to measure I_0 is like trying to use an ammeter to measure the current in an electrical circuit when the internal resistance of the ammeter is nearly equal to that of the circuit that it is trying to measure. The ammeter loads the circuit, and the current it detects is that of the loaded system, not of the unperturbed circuit.

Instead of normalizing to an upstream mesh current, most C $1s$ XANES spectra measured at the SGM were instead normalized to the current generated in a photodiode. This photodiode current spectrum was not taken simultaneously with the sample spectrum, but rather directly afterwards. This technique allows one to directly measure the light intensity hitting the sample as a function of energy, which allows one to correct for the problem of a carbon-contaminated mesh introducing false features into carbon spectra.

Chapter 3

Analysis Techniques

3.1 Density Functional Theory

Density functional theory, originally formulated by Hohenberg and Kohn, holds that all properties in a solid are all functionals of the ground state electron charge density. If one knows the ground state electron charge density, then one could in principle calculate all other macroscopic properties of a solid with this information alone. Equation (3.1) is the Hamiltonian proposed by Hohenberg and Kohn, written in CGS units.

$$\hat{H} = -\frac{\hbar^2}{2m_e}\sum_i \nabla_i^2 + \sum_i V_{ext}(\mathbf{r}_i) + \frac{1}{2}\sum_{i\neq j}\frac{e^2}{|\mathbf{r}_i - \mathbf{r}_j|} \tag{3.1}$$

where the first term is the kinetic energy operator, the second term accounts for external fields, and the last term is the Coulomb operator. The external fields terms also accounts for the Coulomb electric field produced by the fixed ionic lattice. The last term explicitly accounts for two-electron Coulomb interactions.

The full Hohenberg-Kohn Hamiltonian is uniquely determined for a particular electron density. The total energy, which is simply the observable eigenvalue of the full Hamiltonian, is also uniquely determined by a given electron density. The density that minimizes the total energy is, by definition, the ground state particle density. The total energy is given as follows:

$$E_{HK}[n] = T[n] + E_{int}[n] + \int \mathrm{d}^3 r V_{ext}(\mathbf{r})n(\mathbf{r}) + E_{lattice} \tag{3.2}$$

where $T[n]$ is the kinetic energy, the second term is the energy from electron-electron interactions. The third term is the energy of the interaction between the electrons and the fixed

ionic lattice, and the fourth term results from the lattice ions interacting with one another. These are straightforward to calculate, if one knows the density. The first and second terms are much more difficult to calculate, for different reasons. The main problem arises from the kinetic energy term. At present, there is no known way to calculate the kinetic energy directly from the electron charge density.

Despite its intractability, the Hohenberg-Kohn Hamiltonian is nevertheless exact. The Hohenberg-Kohn Hamiltonian can be generalized to include time dependance. Any state to which the system may be excited will have a different electron configuration, however the system must nevertheless start in the ground state, and thus the excited electron density must be a functional of the ground state density. This is in keeping with the Hohenberg-Kohn theorem. The exact Hamiltonian should also have the capacity to accurately calculate Fermi surfaces, as well as the transition between a conductor and a Mott insulator. Thus, density functional theory holds great promise, if only it were possible to calculate the kinetic energy of the system.

Using density functionals directly was thus impossible. Kohn and Sham avoided the problem by replacing the exact many-body Hamiltonian with an auxiliary independent particle one. The Kohn-Sham ansatz recasts the electron charge density in terms of independent particle wavefunctions, and assumes that the ground state electron density is exactly the same for the independent particle approximation as for the full many-body solution. Calculating the kinetic energy from wavefunctions is a well-established theoretical technique, and eliminates one of the chief restrictions to using density functional theory. The Kohn-Sham equations are as follows, written in Hartree atomic units.

$$H^{\sigma}_{KS}(\mathbf{r}) = -\frac{1}{2}\nabla^2 + V_{ext}(\mathbf{r}) + \int \frac{n(\mathbf{r}')}{\mathbf{r}-\mathbf{r}'} + V_{xc}[n] \tag{3.3}$$

where

$$V_{xc}[n] = \frac{\delta E_{xc}}{\delta n(\mathbf{r},\sigma)} \tag{3.4}$$

where the only new term is the exchange-correlation functional, V_{xc}, which is the potential due to the exchange-correlation interaction. The σ denotes spin. The Kohn-Sham Hamiltonian, Equation (3.3), is the operator in a Schrödinger-like equation, called the KS equation.

3.1.1 The WIEN2k Method

The process to find the ground state electron charge density and potential that minimizes the total energy is iterative, and it begins with an initial educated guess as to what the ground state density may be, which is a linear combination of a set of one-electron wavefunctions. These wavefunctions are in turn linear combinations of some basis set, such as plane waves or atomic orbitals. The electron charge density, and the independent particle wavefunctions that gave rise to this density, are both necessary inputs to the total energy, E_{KS}, calculated according to Equation (3.5). As stated earlier, the total energy must be at an absolute global minimum before one can unambiguously state that the ground state electron charge density has been found.

$$E_{KS} = T_s[n(\mathbf{r})] + \int \mathrm{d}\mathbf{r} V_{ext}(\mathbf{r}) n(\mathbf{r}) + \int \mathrm{d}\mathbf{r} \int \mathrm{d}\mathbf{r}' \frac{n(\mathbf{r})}{|\mathbf{r} - \mathbf{r}'|} + E_{xc}[n(\mathbf{r})] \tag{3.5}$$

Once the total energy is known, then one can calculate the energy eigenvalues ϵ_i for each eigenstate ϕ_i:

$$\epsilon_i = \frac{\mathrm{d}E_{KS}}{\mathrm{d}n_i} = \int \mathrm{d}\mathbf{r} \frac{\mathrm{d}E_{KS}}{\mathrm{d}n(\mathbf{r})} \frac{\mathrm{d}n(\mathbf{r})}{\mathrm{d}n_i} \tag{3.6}$$

The electron charge density $n(\mathbf{r})$ has, at this point, been used to calculate the Kohn-Sham potential and the energy eigenvalues that can be substituted into the Kohn-Sham equation (Equation (3.3)). The Kohn-Sham equation can then be solved, through various means, to find eigenstates ϕ_i. These new wavefunctions can be used to calculate a new charge density. This again can be used as input to the total energy functional, and the new total energy is compared to the previous value. If the total energy changes less than some predetermined threshold level between each iteration, then the total energy is *self-consistent*. Otherwise, the density is varied in some systematic manner, and the next educated guess as to the ground state density is used to calculate the next Kohn-Sham potential and eigenvalues.

According to the Bloch theorem, the periodicity of the system requires that the wavefunctions that describe the system may be expressed in terms of a linear combination of plane waves. A natural step in the analysis of the band structure would therefore be to Fourier

transform the the entire problem into momentum space. The plane waves that form the basis set from which the electron wavefunctions are constructed each occupy a single point in momentum space, and the interactions between these points can be evaluated at points in a k-point mesh. This is the heart of the WIEN2k method.

3.2 Normalization of Spectra for Comparison

Comparing experimental spectra typically requires appropriate normalization, so that one may draw conclusions as to how the systems differ from one another. In this case, 'normalization' refers to the process of multiplying a spectrum by some constant so that at least one point of said spectrum is at the same intensity as another spectrum. Normalization, if done correctly, allows one to track how features change with sample, and thus facilitates understanding of how the electronic structures of the samples under study differ from one another. Comparing the spectra from closely related systems, such as samples of graphene oxide that have been treated chemically in different ways, requires a normalization algorithm that provides highly accurate interpretation of minor spectral changes. The trick to normalization, however, is choosing the correct point in the spectrum that one can make equal. In short, there has to be a good reason for forcing multiple spectra to have the same intensity at a single point.

3.2.1 X-ray Absorption Spectra

Normalization of XANES spectra is straightforward: One needs only to measure the spectrum to sufficiently high energy that the promoted core electrons are no longer being excited into bound conduction band states, but rather are being promoted into vacuum states. At this point, the spectral intensity is no longer due to the local pDOS around the atom of interest, but rather to density and stoichiometry [60]. By normalizing XANES spectra to a common intensity in the vacuum region, one effectively normalizes to a common density. Thus, if one normalizes two spectra to a common vacuum intensity and sees that a particular feature grows in Spectrum B in the resonant XANES region as compared to Spectrum A, then there are more electrons in that state per unit of mass of sample. The energy out to where one

must measure to reach vacuum states differs between materials. For C and O K spectra in general, and for organic materials in particular, 30 to 40 eV above the onset of resonant excitation is typically acceptable.

Note that normalizing XANES spectra to a common intensity at an energy within the range of vacuum states is extremely common, but it is not the only way to normalize spectra. As stated earlier, normalizing to vacuum level intensity is, effectively, setting the samples to a common mass density, and any observed spectral changes occur assuming a constant density. However, one could also normalize to a point in the resonant XANES portion of the spectrum. Upon using such a normalization scheme, any observed spectral changes occur assuming a constant density of states at the energy where the spectra were normalized. However, this sort of resonant normalization can produce a comparison that is difficult to interpret. Two choices of normalization methods for comparing the C $1s$ XANES of GO and graphite are shown in Figure 3.1. By normalizing to the π^* feature, as is shown in Figure 3.1(b), it is not obvious how to interpret the comparison. Consider the peak at about 292 eV in both spectra; it is much less intense in the HOPG spectrum. Is it less intense in HOPG because there are fewer such states in HOPG? Or are there more of such states in GO? As it turns out, neither question is appropriate. The GO community knows that the σ bonds are affected much less strongly by oxidization than the π bonds in the π-conjugated network, so the intensity at 292 eV should not change as much as the rest of the spectrum. Improper choice of normalization, in this case, would lead to erroneous conclusions about how oxidization affects the electronic structure.

3.2.2 TICS Ratio Analysis for X-ray Emission Spectra

Normalization of XES spectra is much more complicated. Unlike in a XANES spectrum, an XES spectrum has no vacuum states; all spectral features arise from a core hole being refilled by a bound valence band electron in some process. Thus, there is no convenient point at which one may normalize a group of XES spectra. If the samples are closely related, i.e. a group of similar, but not identical, GO samples, then there may be an energy range in the valence band that is constant between all samples, and thus provides a point where they may all be normalized to the same intensity. However, this is not assured. A normalization

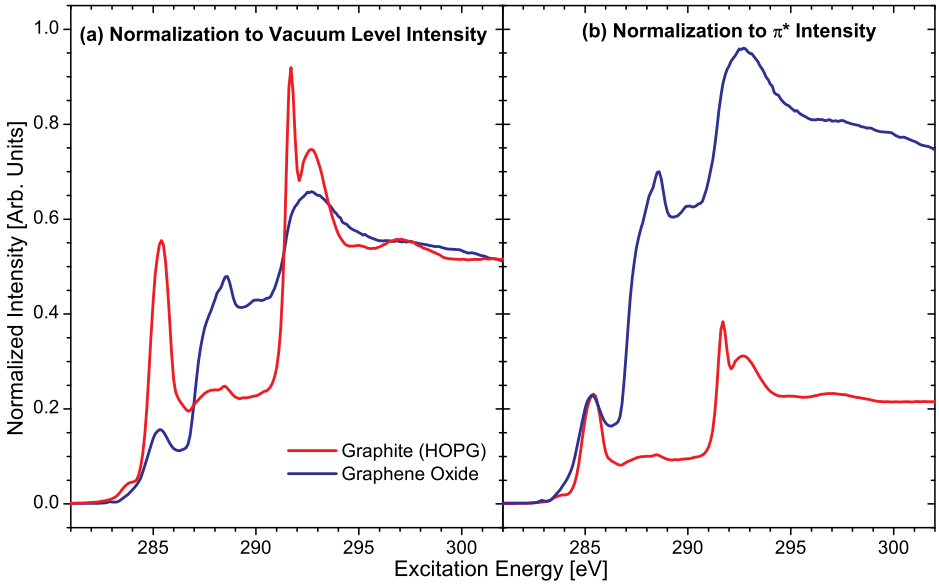

Figure 3.1: A look at two possible normalization choices when comparing GO and graphite. In Panel (a), the spectra are normalized to a common intensity in the vacuum region. In Panel (b), they are normalized to a common intensity on the main π^* resonance at 285.4 eV.

technique that does not require foreknowledge of the electronic structure of the system(s) under study, nor a judgement call on the part of the researcher, would produce less biased results.

To find an appropriate normalization algorithm for XES spectra, one must first consider exactly what is being measured. As discussed earlier, if one can assume a one-electron picture with no scattering, which holds remarkably well for non-correlated systems like organic compounds, the inelastic component of a spectrum is directly proportional to the occupied pDOS of that system. Normalizing an XES spectrum by its total inelastic counts per second (TICS) sets the area beneath the inelastic portion of the spectrum to one. Thus, the ordinate gives the probability density that an electron from a particular part of the density states will refill the core hole in a radiative decay event. Once normalized, an XES spectrum represents the probability density, in energy space, that one core hole will be refilled. Viewed from this standpoint, the TICS value for a spectrum represents, in essence, the total number of core

holes that were refilled *via* radiative decay over the accumulation time of the scan. When divided by the total measurement time, the TICS value gives the average core hole creation rate.

All XES spectra may be normalized to its TICS value in the following way. The spectrum is first smoothed with an FFT filter. Background counts were then removed by subtraction of an appropriate parabolic background function as defined by the noise floor within the spectral measurement window but outside of the spectrum. Each spectrum was then normalized to the integrated intensity of the inelastic portion of that particular spectrum. The elastic peak contributions were isolated and removed by Gaussian peak fitting.

If one were to stop here, then one could examine the distribution of the occupied states (valence electrons) in energy space within one system, and how that distribution differs from that of another system. However, one of the goals of GO research in general, and here specifically, is to understand how the local bonding environment changes as a function of chemical treatment. If one were to normalize each XES spectrum to have a unit area, then the old problem returns: If one compares two spectra from two different samples, but with unit area, and Spectrum A has a higher Peak 1 than Spectrum B, then why is there a difference? Did Peak 1 shrink in Spectrum B due to the process that made Sample B, or did Peak 1 grow for Sample A? If one wishes to remove this ambiguity, then additional, more quantitative analysis is required. Electronic structure simulations can help in this regard, but these are not always possible. A more quantitative comparison of spectra, that requires only experimental input, is required.

One answer lies in the meaning of TICS values. As stated earlier, the time-averaged TICS value, heretofore referred to simply as TICS, is the core hole creation rate. Each spectrum, from each sample, has a unique core hole creation rate that depends on many factors, and normalizing each spectrum provides the probability density that a valence electron will refill one core hole. If instead each spectrum were renormalized to a constant absorption cross-section, then the ability of the system to absorb incoming photons is removed from the problem, and comparing XES spectra measured on different samples takes on a quantitative aspect as one directly measures the relative differences in density of states at a given energy. The spectra would represent the probability of a photon being produced at a given energy

level for the same core hole creation rate.

Let us define the measured emission intensity $I_{XES}[E, E']$ as follows in Equation (3.7):

$$I_{XES}[E, E'] = I_0[E] \cdot \eta^{spec}[E'] \cdot \eta^{rad} \cdot \eta^{mass} \cdot T^{emis}[E, E'] \tag{3.7}$$

where $I_0[E]$ is the incident intensity at excitation energy E, and $T^{emis}[E, E']$ is the transition probability matrix element that a photon will be emitted at energy E' after absorbing a photon of energy E. $\eta^{spec}[E']$, η^{rad}, and η^{mass} are the spectrometer efficiency, the relative radiative decay probability, and the mass density factor, respectively.

The underlying physics that describe $T^{emis}[E, E']$ are, perhaps surprisingly, not relevant here. $T^{emis}[E, E']$ could follow Kramers-Heisenberg formalism, or could simply be decoupled, sequential absorption and emission events described by Fermi's Golden Rule. These details do not matter for the problem at hand. The other three components of Equation (3.7), $\eta^{spec}[E']$, η^{rad}, and η^{mass}, represent different efficiencies. $\eta^{spec}[E']$ encapsulates a wide range of variables that determine how many photons emitted by the sample are actually detected, including the accepted solid angle of the radiation field, the throughput of the spectrometer, and the geometry of the detector. In principle, this varies with the energy of the emitted photons, but in practice, all X-ray spectrometers have efficiency files that make the response of the spectrometer constant across the detector energy range. η^{rad} attempts to account for the fact that radiative transitions are not the only transitions possible. The fluorescence yield of the sample competes with electron yield, and the ratio between the two yields is differs among samples due to the influence of macroscopic factors like conductivity. The last one, η^{mass}, accounts for density effects. In principle, not every photon will interact with the element being probed. A higher concentration of the element in question will lead to a higher η^{mass}, whereas a very small concentration may be visible only as a small perturbation of the background.

When normalizing a spectrum by its TICS, one principally computes:

$$I_{XES}^{Norm}[E, E'] = \frac{I_0[E] \cdot \eta^{spec}[E'] \cdot \eta^{rad} \cdot \eta^{mass} \cdot T^{emis}[E, E']}{\int_{E'_1}^{E'_2} I_0[E] \cdot \eta^{spec}[E'] \cdot \eta^{rad} \cdot \eta^{mass} \cdot T^{emis}[E, E'] \, \mathrm{d}E'} = \frac{T^{emis}[E, E']}{\int_{E'_1}^{E'_2} T^{emis}[E, E'] \, \mathrm{d}E'} \tag{3.8}$$

The last step is possible only if $\eta^{spec}[E']$ has been appropriately handled with an internal efficiency correction to make it constant. If it has, then $\eta^{spec}[E']$, and all other components except for the transition matrix element itself, cancels to leave on with the definition of a normalized probability function.

To renormalize all spectra to a constant absorption cross-section, so that the emission spectra scale with the local pDOS rather than with the total core hole creation rate, then in principal what one wants to calculate is shown in Equation (3.9).

$$I_{XES}^{Norm}[E, E'] = \frac{T_1^{emis}[E, E']}{\int_{E'_1}^{E'_2} T_2^{emis}[E, E']\,\mathrm{d}E'} \tag{3.9}$$

Neither $T_1^{emis}[E, E']$ nor $T_2^{emis}[E, E']$ are directly known, so computing this normalization as it stands is not possible. They are, however, buried inside the TICS for each spectrum, and they can be brought out if one knows some of the other variables in play. Equation 3.10 shows how to renormalize appropriately. As will be shown, η^{rad} and η^{mass} can be approximated from XANES spectra. The value for η^{spec} is, however, another matter. As stated earlier, it is a very complex function of many different characteristics of the beamline. Fortunately, η^{spec} depends entirely upon the experimental apparatus and can thus be forced to be constant by simply measuring all spectra on the same run, or at the very least, on the same beamline. Attempting this normalization algorithm using data from different beamlines will be impossible without detailed and painstaking machine characterization.

$$
\begin{aligned}
I_{XES}^{Norm}[E,E'] &= \frac{T_1^{emis}[E,E']}{\int_{E'_1}^{E'_2} T_2^{emis}[E,E']\,\mathrm{d}E'} \\
&= \frac{T_1^{emis}[E,E']}{\int_{E'_1}^{E'_2} T_1^{emis}[E,E']\,\mathrm{d}E'} \cdot \frac{\int_{E'_1}^{E'_2} T_1^{emis}[E,E']\,\mathrm{d}E'}{\int_{E'_1}^{E'_2} T_2^{emis}[E,E']\,\mathrm{d}E'} \\
&= \frac{T_1^{emis}[E,E']}{\int_{E'_1}^{E'_2} T_1^{emis}[E,E']\,\mathrm{d}E'} \cdot \frac{TICS_1}{TICS_2} \cdot \frac{I_0^2}{I_0^1} \cdot \frac{\eta_2^{spec}[E']}{\eta_1^{spec}[E']} \cdot \frac{\eta_2^{rad}}{\eta_1^{rad}} \cdot \frac{\eta_2^{mass}}{\eta_1^{mass}} \qquad (3.10)
\end{aligned}
$$

The final form of Section 3.2.2 thus has two major components: The spectrum in question, normalized to one, and a renormalization factor. This renormalization factor is called I^{Renorm}, and is given explicitly by

$$
I^{Renorm} = \frac{TICS_1}{TICS_2} \cdot \frac{I_0^2}{I_0^1} \cdot \frac{\eta_2^{spec}[E']}{\eta_1^{spec}[E']} \cdot \frac{\eta_2^{rad}}{\eta_1^{rad}} \cdot \frac{\eta_2^{mass}}{\eta_1^{mass}} \qquad (3.11)
$$

η^{rad} and η^{mass} can both be approximated by analyzing XANES spectra. η^{rad} represents the fluorescence efficiency, and therefore denotes the probability that the sample will emit a detectable photon per photon absorbed. Fluorescence and Auger decay, which makes TEY spectra possible, compete for photons, then η^{rad} is simply the percentage of the total yield, at an energy above the edge, that was fluorescence. η^{mass}, on the other hand, is the probability that a photon absorbed will produce a core hole, regardless of decay path. The equations for η^{rad} and η^{mass} each are described by Section 3.2.2 and Section 3.2.2, respectively.

$$
\eta^{rad} = \frac{TFY^{Vac} - BG}{TFY^{Vac} + TFY^{Vac} - 2 \cdot BG} \qquad (3.12)
$$

$$
\eta^{mass} = \frac{TFY^{Vac} + TFY^{Vac} - 2 \cdot BG}{TFY^{Vac} + TEY^{Vac}} \qquad (3.13)
$$

where TFY^{Vac} is the intensity of the TFY spectrum at the vacuum level, TFY^{Vac} is the

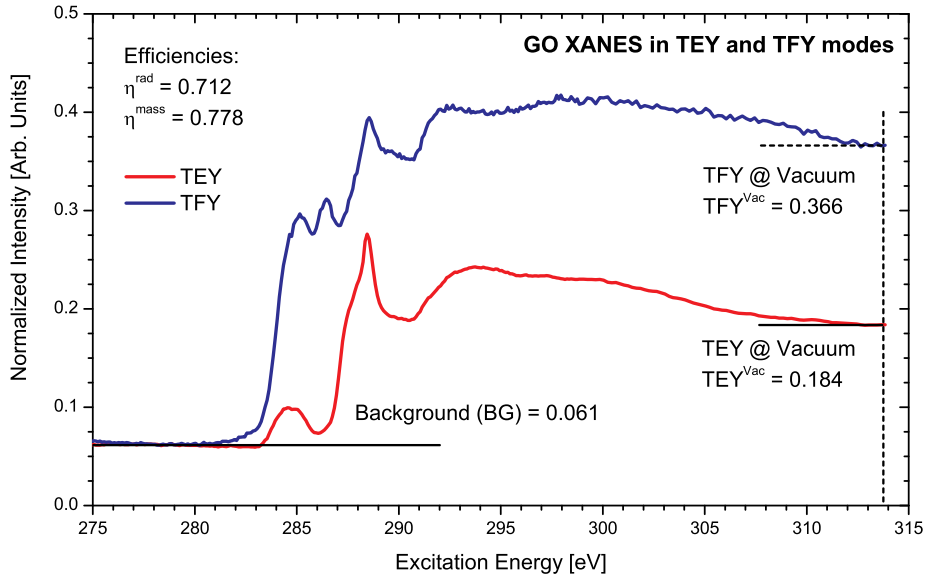

Figure 3.2: Example of how to calculate η^{rad} and η^{mass}, quoted in the top left corner, using XANES. The spectra were normalized so that each had the same background. The values TFY^{Vac}, TEY^{Vac}, and BG were used as per Section 3.2.2 and Section 3.2.2 to calculate η^{rad} and η^{mass}, respectively.

intensity of the TEY spectrum at the vacuum level, and BG is the pre-edge background intensity. BG is common to both TEY and TFY spectra, because the backgrounds of both are normalized to the same value in order to test the response of system from the same starting point. This step allows both the TFY and TEY spectra to be compared directly. Figure 3.2 gives an example of how to derive the values for η^{rad} and η^{mass} from XANES spectra.

At this point, all necessary information has been found in order to renormalize a group of XES spectra to the same radiative emission probability, thus forcing the XES spectra to scale with changes in the local occupied pDOS. This in turn allows one to compare XES spectra and understand more completely any observed peak intensity changes. It is important to note that more has been accomplished than renormalization. The renormalization factor, I^{Renorm}, also carries useful information about the system.

3.2.3 Theoretical Renormalization Factors

The renormalization factor I^{Renorm} is, in its most basic form, a ratio of the integrated radiative transition matrix elements for two different materials. These cannot be directly measured from experiment, so one must go through TICS ratios to get at the desired information. However, we can try to model the ratio. I^{Renorm} will depend most strongly on the density of states in the numerator and denominator. The requisite density of states can be modeled by a sum of the components in the system, with each component represents by its relative population and the density of states provided per component. Thus, I^{Renorm} is simply a function of relative bond populations and the relative cross-sections of those bonds at any given energy. In short:

$$I^{Renorm} = \frac{[n_1 \cdot \frac{B_1}{B_{tot}} + n_2 \cdot \frac{B_2}{B_{tot}} + \ldots + n_i \cdot \frac{B_i}{B_{tot}}]_{Sample1}}{[n_1 \cdot \frac{B_1}{B_{tot}} + n_2 \cdot \frac{B_2}{B_{tot}} + \ldots + n_k \cdot \frac{B_k}{B_{tot}}]_{Sample2}} \tag{3.14}$$

where B_i is the population of the ith site with a particular bond, B_{tot} is the total number of sites, and n_i is the relative integrated DOS of the ith bond.

When applying this general formula to graphene oxide, there is the further complication that it is a nominally planar material. As such, in-plane and out-of-plane lines of sight see very different types of bonding. This is significant because of the effects of so-called geometrical selection rules when promoting s-symmetry electrons into unoccupied p-symmetry states, which are discussed below. For planar materials, the cross-section of all bonds will be reduced depending on the angle of incidence θ of the incoming beam with respect to the plane of the sample.

$$I^{Renorm} = \frac{[IPXS_1]\cos^2\theta + [OPXS_1]\cos^2(\pi/2-\theta)}{[IPXS_2]\cos^2\theta + [OPXS_2]\cos^2(\pi/2-\theta)} \tag{3.15}$$

where $IPXS$ is the total cross-section density (cross-section per bond multiplied by bond density) of the in-plane bonds and $OPXS$ is the total cross-section density of the out-of-plane bonds. Because epoxides and hydroxyls are bonded to the top and bottom of a given graphene sheet, and carboxyls are bonded to the outer rim of the sheet generally in-plane, then the formula becomes:

$$I^{Renorm} = \frac{[n^C \cdot C(C)_1 + C(\sigma^*)_1]\cos^2\theta + [n^{H+E} \cdot C(H+E)_2 + C(\pi^*)_2]\cos^2(\pi/2-\theta)}{[n^C \cdot C(C)_1 + C(\sigma^*)_1]\cos^2\theta + [n^{H+E} \cdot C(H+E)_2 + C(\pi^*)_2]\cos^2(\pi/2-\theta)} \tag{3.16}$$

where $C(H+E)$, $C(\pi^*)$, $C(C)$, and $C(\sigma^*)$ are the ratios of the carbons bonded to epoxides and hydroxyls, carbons with π^* C=C bonds, carbons bonded to carboxyls, and σ-bonded carbons to the total number of carbons, respectively. n^{H+E} and n^C are the relative integrated per-unit DOS values of the out-of-plane functional bonds (epoxide and hydroxyl) and in-plane functional bonds (carboxyl). The formula has been simplified significantly from its most general form in Equation (3.14) by assuming that the π^* and σ^* C=C bonds have the same DOS per site.

The n values, the relative difference of total integrated intensity for each of the functional groups, should scale with core hole creation rate. As such, these values should be greater than one for the functional groups, because functionalized carbon has fewer electrons than neutral carbon because the C-O bonds are polarized. The n values account for the fact that carbon atoms, when bonded to functional groups add more spectral weight per atom than non-functionalized carbon. The degree of charge transfer from carbon to oxygen can be estimated from DFT calculations.

By using the symmetry of the system, as well as measured bond concentrations and relative DOS ratios taken from DFT calculations, one can determine what the ratio of the transition rates should be, and hence, how one should scale XES spectra, regardless of whether the XES spectrum is resonant or non-resonant. This can serve as a check to make sure that the ratios that one calculated experimentally are providing an accurate picture of what is happening.

3.3 Band Gap Determination

The band gap is highly sought physical quantity in condensed matter physics. It impacts a large number of macroscopic properties such as color, hardness, and electrical conductivity. As was shown earlier in Equation (2.3), the conductivity of a sample depends upon the

number of available charge carriers, n_e and n_h. As was also mentioned, the DOS, in particular, the DOS near the Fermi level, can affect this quantity. However, a charge carrier must be moved out of its ground state configuration if it is to conduct through the sample. In terms of band structure, an electron must be moved to the aptly-named conduction band (CB) from the valence band (VB), and a hole must be moved from the CB to the VB. This transition requires energy, and quantifying that energy theoretically has been an ongoing challenge for condensed matter physicists. The transition energy to move charge from the ground state into an excited state that leads to conduction is defined generally in Equation (3.17):

$$E^{Trans} = E^{EX}_{sys} - E^{GS}_{sys} \tag{3.17}$$

where E^{EX}_{sys} is the total energy of the excited state of the system, and E^{EX}_{sys} is the total energy of the ground state of the system.

The band gap is defined as the energy difference between the lowest point in the CB and the highest point in the VB, as defined by Equation (3.18).

$$E_{BG} = E^{min}_{CB} - E^{max}_{VB} \tag{3.18}$$

In the one-electron picture, electrons are treated as independent entities that can move with impunity within the background field generated by the lattice and the rest of the electrons without perturbing anything. If this approximation is accurate, then E^{Trans} and E_{BG} are the same, because the only energy that one needs to supply to the system is the energy needed to promote one electron across the band gap to the CB (or promote a hole across the band gap to the VB). This act will have no affect on the rest of the system. If the one-electron picture does not hold, however, then changing the energy and/or momentum of one electron will affect the rest. Thus, the energy that one must pay to force a charge carrier to conduct is the cost to redistribute charge in the system at large, which is typically much larger than the band gap. The Hubbard U, a non-*ab initio* energy parameter introduced by Mott and Hubbard through the tight-binding model framework, was implemented to try and explain the anomalously large band gap in transition metal oxides [43]. In such a system, where the electron interact in this manner, and they are said to be correlated.

In short, trying to find the band gap is only useful if the band gap is a useful quantity to know, which is generally the case only when the one-electron picture is a sufficiently accurate approximation. In the case of organic systems, this is a good assumption to make given that electron correlation effects that require the use of many-body models are typically a problem only with d and f shell electrons.

For graphene oxide, E_{BG} and E^{Trans} are comfortably equivalent concepts. All that remains is how to accurately find E_{BG}. As it turns out, XANES and XES spectra have the information that is required. According to Fermi's Golden Rule, the XANES and XES spectra are both proportional to the unoccupied and occupied pDOS, respectively. Thus, the band gap is the difference between the lowest point in the XANES spectrum and the highest point in the XES spectrum, assuming that both have been properly calibrated to sit on the same energy axis. Of course, the caveat is that these spectra are, in principle, measured with respect to the $1s$ core level which, in the case of the XANES spectrum, is only half-filled. To determine the ground state band gap using XANES and XES with the greatest level of accuracy, one must account for the core hole effect. One method is to simulate the ground state DOS and the excited, core-hole perturbed state DOS and compare them to find out how strongly the core hole perturbs the system [42]. However, for reasons that I cannot explain at this time, inclusion of the core hole for C $1s$ XANES spectra provides poor results as compared to XANES using the ground state DOS. All calculations reported in the attached papers were performed using WIEN2k, but inclusion of the core hole worsens the accuracy of theoretical results when using other codes as well, notably StoBe and FDMNES. Thus, calculation of the core hole effect is not a necessary step because it seems to have a marginal effect.

Thus, gleaning the lowest point in the XANES spectrum, and the highest point in the XES spectrum, will give the band gap without need of further processing. All that remains is exactly how to find where XANES spectrum begins and the XES spectrum ends. This, as it turns out, is a non-trivial task. There have been many suggested ways to find the band onsets, but a highly reliable and accurate way to determine the band onsets is the second derivative method.

The second derivative is useful, first and foremost because it emphasizes features that are

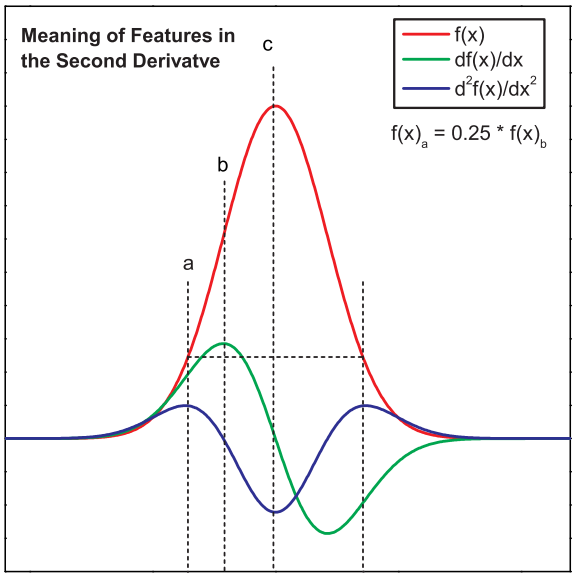

Figure 3.3: The 1st and 2nd derivatives of a Gaussian.

sharp. This allows features that have low intensity but strong curvature, such as one might find at the onset of a band, to be seen with much greater clarity than when buried in the spectrum. The choice is therefore whether to choose a local minimum or a local maximum for the beginning of the band. The choice is non-trivial, and depends upon the physics of the system under study.

Local maxima in the second derivative represent the point at which the curvature is most positive, and thus represent a strong upswing. For highly crystalline systems with relatively broad bands with high dispersion, this may be an appropriate choice because a local maximum in the second derivative will represent the point where the band becomes most obviously different from the background. For molecular, quasi-molecular, or highly disordered systems, however, the meaning of local maxima in the second derivative become harder to interpret. Although there will be bands, each band may be quite narrow. As such, local maxima in the second derivative may not accurately reflect band onsets, but rather, shoulders due to broadening, as is shown in Figure 3.3. Figure 3.3 shows a Gaussian profile, which is chiefly due to experimental broadening, but broadening of any sort will produce local

maxima at that have nothing to do with the electronic structure. Even lifetime broadening, which is due to the physics of the sample, is due to the lifetime of an excited state caused by the presence of a core hole. This obviously would not occur if one was attempting to use the material in an electronic device.

For highly disordered systems such a graphene oxide, local maxima in the second derivative do not provide a reliable way to estimate the beginning of either the conduction band or the valence band, because parsing the effects of true band shape from broadening is difficult. However, local minima in the second derivative can only be interpreted in one way: They represent features in the DOS. This is true for all systems, regardless of the degree of order. Thus, measuring the band gap using local minima is the safest course of action in a quasi-molecular system such as graphene oxide.

Chapter 4

Epoxide Speciation and Functional Group Distribution in Graphene Oxide Paper-Like Materials

The chaotic nature of graphene oxide makes it difficult to model with the standard toolbox of theoretical methods available to a condensed matter physicists, such as DFT. With this work, we sought to understand how it is that functional groups interact with one another. This work also served as a first look at the ways in which graphene oxide changes over time, because the samples were relatively old by the time that the spectra were measured; each sample had aged in air, at room temperature, for a significant period of time before its spectra were measured at the Advanced Light Source.

Three samples were under study: Graphene oxide paper (GOp), graphene oxide paper that had been intercalated with dodecylamine (iGOp), and graphene oxide paper that had been reduced with hydrazine (rGOp). There experiments were performed on each sample: C Kα RXES, O Kα RXES, and angular-resolved C 1s XANES. The C 1s XANES measurements showed results that were, for the most part, what was expected for the spectra of graphene oxide derivatives: prominent features around 285.2 eV, 287.4 eV, and 288.5 eV were all present, as expected, complete with appropriate relative intensities. However, there was one anomaly: There was a prominent feature in the rGOp spectrum at 288.2 eV that had not been seen before, and was not present (to the same degree) in all samples.

Measuring RXES spectra while resonantly exciting at 288.4 eV did not reveal the source of this feature, given that C Kα XES spectra are, typically, broadened to a large degree by VB lifetime effects that cannot be mitigated. The features in O Kα XES spectra, however, are

much easier to resolve. Thus, measuring an O Kα RXES spectrum while exciting the sample at the appropriate point on the O 1s edge would provide further information. This idea is based on the fact that bonded atoms share the many of the same states, so the absorption spectra of both sites should have many of the same features, even if the relative intensity of the features may not be the same on both thresholds. Thus, an excitation energy of roughly 534.3 eV is necessary to resonantly excite an O 1s core electron into the same unoccupied states that a C 1s core electron is promoted if excited at 288.2 eV. As it turned out, the 534.6 eV RXES spectrum did indeed possess a unique feature that could not be explained by the typical functional groups.

Using DFT simulations of ethylene oxide (to simulate the O states in an epoxide group) and dimethyl ether (to simulate the O states of an ether group), we found that the signature feature in the 534.6 eV spectrum was due to ether. The ether group is the result of epoxides lining up along the carbon basal plane and achieving a lower energy state by breaking C-C that completed the epoxide triangle. The aligning of the epoxides is not a natural starting state of GO, and as such, represents an aging effect.

Using TICS ratio analysis to scale the C Kα RXES spectra according to their relative DOS, we were able to conclude that iGOp was a more ordered structure because it had a higher contrast between emission from the σ- and π-symmetry states arising from graphene-like states. Not all excitation energies for iGOp exhibited the same higher contrast: If resonantly exciting hydroxyls at 286.0 eV or 286.4 eV, one does not see the higher contrast. Thus, we concluded that hydroxyl groups appear only in zones of dense functionalization because there was no signature from the graphene states. This verified the Lerf-Klinowski model that suggests that graphene does not oxidize uniformly, with the additional information that hydroxyl groups appear only in dense oxidization zones, whereas epoxides can appear anywhere.

This work has been published in the journal *Advanced Functional Materials* (Epoxide Speciation and Functional Group Distribution in Graphene Oxide Paper-Like Materials. *Advanced Functional Materials* **22** (2012) 3950-3957). Legal permission to reproduce this work is included in Appendix A. The following list delineates the contributions of each author to the complete paper.

A. Hunt:

- Measured the GOp O Kα and C Kα XES data, as well as all C 1s XANES spectra
- Made all figures, and wrote most of the text of the manuscript
- Derived the TICS ratio analysis methodology

D. Dikin:

- His group made all of the samples
- Measured the C:O ratios for all functional groups
- Contributed writing suggestions and editing

E. Kurmaev:

- Responsible for original motivation of the project and procurement of samples
- Wrote the original introduction
- Aided in literature review

T. Boyko:

- Measured the C Kα and O Kα RXES on iGOp and rGOp
- Helped with TICS ratio analysis
- Contributed to editing the manuscript

P. Bazylewski:

- Performed the bulk of the work to simulate the O Kα RXES spectra of dimethyl ether and ethylene oxide molecules
- Contributed writing suggestions and editing

G. S. Chang:

- Ph.D. supervisor for P. Bazylewski
- Aided in the simulation work
- Contributed strongly to the editing process

A. Moewes:

- Ph.D. supervisor of A. Hunt
- Integral to the writing of the first manuscript
- Aided in the interpretation of the spectra

4.1 Manuscript

Epoxide Speciation and Functional Group Distribution in Graphene Oxide Paper-like Materials

Adrian Hunt,[1*] Dmitriy A. Dikin,[2] Ernst Z. Kurmaev,[3] Teak D. Boyko,[1] Paul Bazylewski,[1] Gap Soo Chang,[1] Alex Moewes[1]

[1]Department of Physics and Engineering Physics, University of Saskatchewan, 116 Science Pl, Saskatoon, Saskatchewan, Canada S7N 5E2
[2]Department of Mechanical Engineering, Northwestern University, 2145 Sheridan Road, Evanston, Illinois, USA 60208-3111
[3]X-ray Emission Spectroscopy Lab, Institute of Metal Physics, RAS Ural Div., 18 Kovalevskoi Str., 620990 Yekaterinburg, Russia

*Corresponding author. Email: adrian.hunt@usask.ca (A. Hunt)

4.1.1 Abstract

The electronic structure and chemical bonding of three differently prepared samples of graphene oxide paper-like sheets are studied. Two are created by water filtration of fully oxidized graphene sheets, although one is later intercalated with dodecylamine. The third is created by reducing graphene oxide with hydrazine hydrate. The spectroscopic fingerprints of the aligned epoxide functional groups that unzip the carbon basal plane are found. This unzipping appears to be a result of aging, and the extent to which the basal plane is unzipped can be controlled via the preparation method. In particular, reduction with hydrazine enhances line defect formation, whereas intercalation inhibits the process. The hydroxyl functional group also has a tendency to gather in zones of dense oxidation on the carbon basal plane, a predilection that is not shared by the other prominent functional group species. Finally, the non-functionalized carbon sites exhibit very similar bonding despite the increase in the sp2/sp3 ratio, confirming that reduction alone is insufficient for producing pristine graphene from graphene oxide. These results are obtained by directly probing the electronic structure of the graphene oxide samples *via* X-ray absorption near-edge structure spectroscopy (XANES) and resonant X-ray emission spectroscopy (RXES). This work has important significance for the development of graphene oxide as a band gap-engineered elec-

tronic material, as preparation methodology strongly affects not only the initial condition of the sample, but how the electronic structure evolves over time.

4.1.2 Introduction

Graphene has attracted much interest of late as the first two-dimensional crystal ever experimentally realized [1]. Pristine graphene is a zero-band gap semiconductor with electrons behaving like massless Dirac fermions [4], although doped graphene will stray from this simple but elegant band structure [13]. Graphene is a material that has been suggested for use in supercapacitors [7], as a hydrogen storage medium [8–10], and even in integrated circuits as active components as well as interconnects. [6] If graphene were used as an interconnect, the ballistic transport properties alone would make it an excellent choice [5]. Organic photovoltaic researchers have also looked at graphene for use as an intermediate layer between two cells [61] However, the question of how to most efficiently synthesize graphene remains. One option is to first make graphene oxide by exfoliating graphite oxide in water or another polar solvent [16] then reduce the harvested graphene oxide sheets to make graphene [17]. This process is easily scalable to industrial production levels, and thus is a more cost-effective manufacturing method than the micro-mechanical exfoliation method used to first isolate graphene.

Beyond its use as a graphene precursor material, however, graphene oxide may prove to be a useful material in its own right. Graphene oxide, because of its solubility in common solvents, has been used to replace both the typical indium tin oxide (ITO) electrode [62, 63] and the equally ubiquitous soluble fullerene-derivative n-type organic semiconductor, PCBM, in organic solar cells [64, 65], and has even been shown to function as a photocatalyst [14]. Chemically-reduced graphene oxide has also been suggested as a detector for airborne molecules [15]. Perhaps one of the most ambitious suggestions for the use of graphene oxide is to employ this material in electronic devices, replacing silicon in integrated circuits. However, the lack of a noticeable band gap in graphene limits its utility for electronics applications. It is therefore important to develop methods to induce and control a band gap in graphene. A band gap may be created in graphene using one of two methods: by functionalizing graphene [66] or by chemically treating graphene oxide [19]. With the

natural tendency of graphene oxide to stack in ordered layers, and with pristine graphene functioning as highly conductive and chemically stable interconnects, a new era of carbon-based electronics may be realized [20]. However, many problems must be overcome before these goals may be realized, not the least of which being able to properly and reproducibly control the electronic and physical structure of graphene oxide. Many have theorized about the structure of graphene oxide and its precursor graphite oxide [21–25], and there have been many experimental studies using various techniques to characterize these materials [26–29]. In particular, X-ray absorption near-edge fine structure (XANES) studies of graphite oxide have been highly useful in elucidating the local electronic structure of the carbon and oxygen sites in graphene oxide [30–34].

Despite the impressive work done on graphene oxide, many questions persist as to the structure of this material. One particularly poignant question concerns the bond integrity of the carbon lattice under the strain of functional group bonding. The functional groups, originally attached to the 2D carbon plane to make graphene oxide soluble, may serve to alter the electronic and physical structure of graphene in a variety of beneficial or deleterious ways. The epoxide functional group has attracted special focus because some studies have suggested that this functional group may serve to unzip the C-C intraplanar bonds in graphene [23]. Line defects have been visually observed in HOPG [39], and unzipping carbon nanotubes to produce graphene nanoribbons is a very active area of research [40]. To answer some of these questions, we present an experimental comparison of three samples of graphene oxide paper, all prepared in different ways. These samples were studied using synchrotron-based X-ray absorption near-edge fine structure (XANES) and resonant X-ray emission spectroscopy (RXES), so that the oxygen and carbon states could be probed separately for detailed, element- and site-specific information.

4.1.3 Results and Discussion

Graphene research in general, and graphene oxide research in particular, has proceeded quickly down many different paths as researchers attempt to find the optimal ways to make, and use, these materials. This study focuses on three of the archetypal graphene oxide products: "fully" oxidized graphene oxide (GOp) and graphene oxide paper that has been reduced

Table 4.1: C:O ratios for all three samples at the time of synthesis. The overall ratio includes only the oxygen contained within functional groups bonded to the carbon basal plane, and does not account for any intercalated water.

Sample system	Overall ratio C(graphene):O	Ratios for oxygen-containing groups		
		Epoxide	Hydroxyl	Carbonyl/Carboxyl
GOp	2.9	4.9	19.3	11.15
rGOp	5.0	16.7	9.8	26.3
iGOp	2.6	5.8	18.6	6.3

with hydrazine hydrate (rGOp) [17], and graphene oxide paper that has been intercalated with dodecylamine (iGOp), all made into paper-like products. The preparation methodology used to make graphene oxide paper is described elsewhere [67, 68]. Table 4.1 below details the overall C:O ratio for each of the three samples, as well as the approximate C:O ratio for each functional group. Oxygen in water was not included in the C:O ratios.

To confirm and expand upon our understanding of the chemical structure of the three samples of graphene oxide paper, let us turn to angular-resolved XANES spectra of the three samples, measured while exciting upon the C $1s - 2p$ resonant absorption threshold. As mentioned earlier, aside from C $1s$ XPS, C $1s$ XANES experiments have thus far been the most prevalent method of characterizing graphene and graphene oxide systems using X-rays. Figure 4.1 presents the C $1s$ XANES spectra. Generally speaking, the spectra show many of the features that one expects to find in graphene oxide as found in previous studies [30–34], which are labeled according the anti-bond that is being resonantly filled at that energy. These features are generally attributed to different functional groups by comparison of the C $1s$ XANES spectra of graphene oxide to spectra of simpler systems with similar structure. As an example, consider benzoic acid, phthalic acid, pyrocatechol, and salicylic acid, which are compounds with carboxyl and/or hydroxyl functional groups attached to a benzene ring. The C $1s$ XANES spectra of these compounds clearly show a peak structure that changes according to the relative mix of hydroxyl and carboxyl bonding [56]. This allows one to assign the peaks seen in the C $1s$ XANES spectra of graphene oxide to the functional groups that gave rise to them in the spectra of the benzene-based acids.

There is, however, one marked difference between our spectra and those that have been published by others. The inset in Figure 4.1(e) shows a zoomed view of the rGOp spectra,

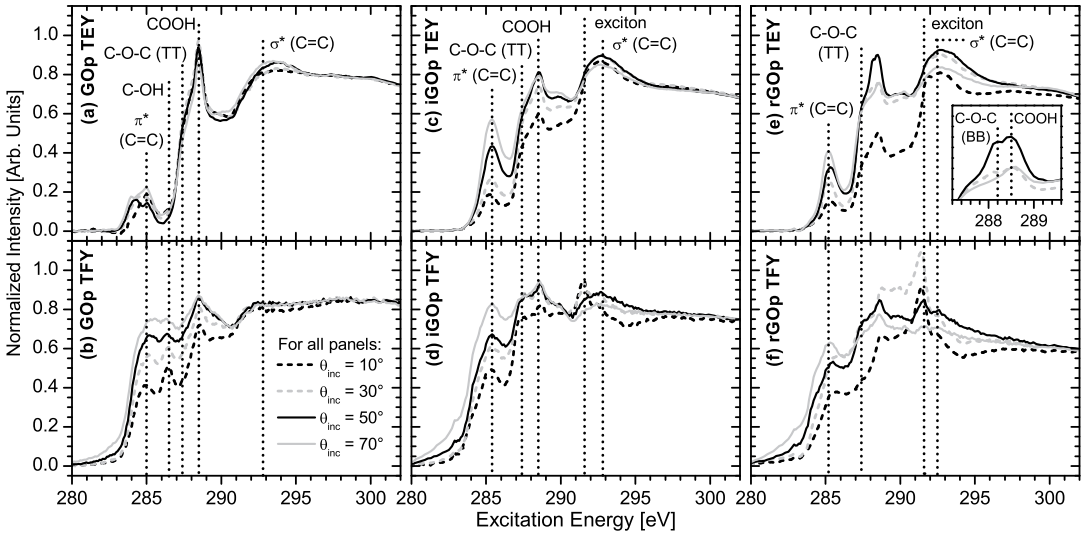

Figure 4.1: Angular-resolved XANES spectra, measured simultaneously in total electron yield (TEY) and total fluorescence (TFY) modes while the incident radiation was 30° from the surface normals of the samples. All of the spectra in a particular panel have been normalized to a common point at high energy. (a) TEY of GOp. (b) TFY of GOp, measured simultaneously with the TEY. (c) TEY of iGOp. (d) TFY of iGOp. (e) TEY of rGOp, with an inset zooming into the 288.5 eV resonance features. (f) TFY of rGOp.

focused on the region around 288.5 eV. It is quite clear that two features are resolved: one at 288.2 eV, and one at 288.5 eV. The 288.5 eV is a common and prominent feature in other reported XANES studies of graphene oxide and graphite oxide, but the 288.2 eV feature, to the best of our knowledge, has not previously been seen. It is not present, or at least not resolved, in the TEY spectra of either of the other two samples at any angle.

As we shall later show, this 288.2 eV feature is the spectral signature of a particular allotrope of epoxide that can occur if the normals of the surface defined by the C-O-C triangle of many epoxide groups align collinearly. This alignment makes spontaneous breaking of the C=C bond energetically favorable, forming a defect line [23, 69], although the mechanism powering the break is in dispute [39, 70]. This so-called 'unzipping' of the carbon basal plane can break graphene into pieces, possibly to the benefit of nanotechnological applications if controlled properly [71]. This type of epoxide we call broken bond epoxide (BB-epoxide). Given that BB-epoxide is most prominent in rGOp, it could be a product of the reduction

process, a functional species that was always present and has a higher resistance to hydrazine than other functional groups, or it is an aging effect.

Functional Group Dispersion and Ordering

More details are clearly needed in terms of the bonding, particularly concerning this newly observed functional group. Let us therefore turn to RXES. This technique allows one to resonantly excite the different functional groups and probe the local bonding environment that each sees. RXES spectra were measured while exciting the three differently-prepared samples of graphene oxide paper listed earlier at six distinct energies that include the approximate binding energies of the functional groups observed in Figure 4.1. Figure 4.2 shows the results of the RXES experiment.

Intuitively, the differences among the lineshapes of the three samples should indicate differences among the bonding environments seen by the sites probed by the incident X-rays. The question then becomes how one can appropriately normalize the spectra from the samples under scrutiny so that peak intensity differences are physically meaningful. The method chosen for this study is normalization by total integrated counts per second (TICS) ratio. A description of the calculation of experimental TICS is detailed in the Experimental section at the end of the manuscript. In short, normalizing spectra by a common TICS value allows quantitative comparison of peak intensities among spectra of different compounds by compensating for differences among the core hole creation rates of the samples. The ratio of TICS values between two samples gives the relative core hole creation rate.

The effect that each functional group has on the electronic structure is different, particularly when considering the optical properties that are so important to the application of graphene oxide to organic photovoltaic research [72]. Thus, the distribution of the functional groups and any remaining non-functionalized carbon becomes a key concern. This issue is particularly relevant to the reduction process because the different functional groups do not react with various reducing agents (in this case, hydrazine) to the same degree. The degree of homogeneity in functional group dispersion will thus directly impact the structure of the end product. Lerf and Klinowski [26, 27] have proposed that graphene oxide does not oxidize uniformly based upon ^{13}C NMR studies of graphite oxide. This idea has been supported by

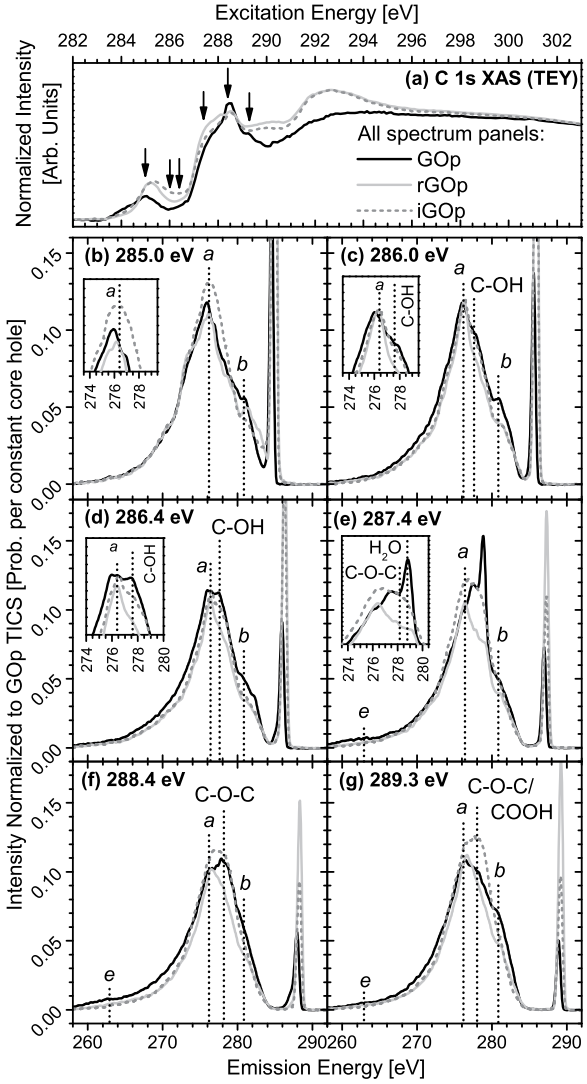

Figure 4.2: C Kα RXES spectra of graphene oxide paper. (a) XANES spectra of the three samples to indicate graphically where the excitation energies are on the threshold. (b) through (g) RXES spectra of GOp, rGOp, and iGOp measured while exciting each sample the energy indicated in the bold title block in the top left corner of each panel. All spectra had background counts subtracted and were smoothed with an 10-point FFT filter and normalized to calculated GOp TICS. Insets in panels (b) through (e) show a zoomed window of the spectra where differences are easier to see. Several prominent features are labeled with the functional group that is the most probable main contributor to the bulk of the measured spectral weight.

later studies on graphite oxide [73] and on graphene oxide [74,75], although it does contradict other proposed models [76].

Our results show that the Lerf-Klinowski non-uniform oxidation pattern holds, but with a further refinement. We show that dense oxidation zones contain most of the bonded hydroxyl groups, whereas epoxides and carboxyls are more evenly dispersed. Uncovering the evidence for this conclusion begins, perhaps paradoxically, with the study of the non-functionalized carbon sites, hereafter called pristine graphene-like (PG-like) states. The local bonding pDOS of these sites are detailed in the RXES spectra shown in Figure 4.2(b), measured while exciting the samples at 285.0 eV. This excitation energy is very close to the main π^* resonance in HOPG at 285.4 eV, but below the resonant excitation energies for the major functional groups (see Table 4.2). As one can see in Figure 4.2(b), the iGOp spectrum shows a higher a/b peak height ratio than either GOp or rGOp. The reason for this will be touched upon later, but for now, let us focus on the fact that peak a in iGOp is characteristically higher than that in the spectra of either GOp or rGOp. The intensity variation pattern of peak a in the 285.0 eV spectra is also seen in Figure 4.2(e), (f), and (g). However, this pattern is not seen in (c) or (d). The consensus among authors using XPS is that a photon with an energy that falls in the range of 286.0 eV to 286.4 eV will resonantly excite a C atom bound to a hydroxyl functional group [34, 77–85]. These XPS results are summarized in Table 4.2. It would seem that, when exciting a hydroxyl group, the PG-like states do not fluoresce nearly as strongly. It is clear that the hydroxyl functional groups electronically interact poorly with PG-like states. This suggests that hydroxyl groups bunch together in zones of dense oxidation, separated physically and electronically from zones of light oxidation where PG-like states occur. The other functional groups do not seem to experience this separation. Resonant excitation of epoxide (287.2-288.3 eV) and carboxyl (288.5 eV) shows the return of PG-like fluorescence.

The reason for the higher a/b peak height ratio in the 285.0 eV spectrum of iGOp is that intercalating dodecylamine between the graphene oxide planes produced a more ordered sample. In structures similar to graphite, peak a is due to emission from in-plane σ-symmetry bonds, and b is due to out-of-plane bonding. The out-of-plane bonding can either be σ-symmetry in $sp3$ bonding, or π-symmetry in $sp2$ bonding; at 285.0 eV, any $sp2$ bonding

Table 4.2: Literature C 1s XPS binding energies of functional groups in graphitic and graphenic systems

C-ring π^*	Hydroxyl C-O	Epoxide C-O-C	Carbonyl C=O	Carboxyl COOH	Carbonate CO_3	Reference
	286.7	287.2		288.2		77
285.0	286.4	287.2		289.4		34
284.9 - 285.1	286.3 - 286.9	287.2 - 287.8		289.0 - 289.6		78
284.6 - 285.1	286.3 - 287.0		287.5 - 288.1	289.3 - 290.0		79
284.1	286.7	288.3			290.0	80
284.8	286.2		287.8	289.0		81
284.5	286.5				290.5	82
284.6	286.1		287.5	289.2		83
284.6	286.6		288.5			84
284.3	286.1		287.4	288.1		85

present will be resonantly excited. Analogous to XANES spectra, a higher contrast between the σ and π emission lines means greater ordering. Thus, we can conclude that iGOp is a graphene oxide derivative that has more ordered planar structure. As we shall show later in the paper, this is because the carbon planes in iGOp have not been unzipped by suitably aligned epoxide functional groups.

Returning to Figure 4.2(b), one is struck by how similar are the spectra of GOp and rGOp. This shows that the PG-like states are qualitatively very similar in the two compounds. The significance of this observation is that, while chemical reduction does increase the $sp2/sp3$ ratio and thus increases the number of non-functionalized carbon atoms, reduction does not make the bound carbon states more graphene-like. The likely reason for this is that distortions to the carbon basal plane from oxidation remain after reduction.

Within Figure 4.2, characteristic emission lines from the different functional groups were highlighted. The assignment of a spectral feature in a C Kα spectrum to emission from a particular functional group was done simply by looking at which functional group was being resonantly excited at the excitation energy in question. For example, in reference to Figure 4.1, the resonant excitation energy needed to create core holes on carbon sites bonded to hydroxyl (the C-OH bond) is about 286.4 eV. It is therefore logical that the emission line seen at 277.6 eV is due to the C-OH bond. For excitation energies 287.4 eV and 288.4 eV, the

epoxide functional groups were resonantly excited. At these energies, the 277.6 eV feature seen previously was replaced by a feature at 278.2 eV due to emission from epoxide.

Epoxide Speciation

The C Kα spectra of Figure 4.2 have shown some important aspects of the bonding in graphene oxide, but the spectra measured while exciting at 288.4 eV show no discernible, characteristic emission line from the new functional group first detected at 288.2 eV binding energy in the XANES spectra of rGOp. The reason for this is likely a combination of the large number of carbon states contributing to the 288.4 eV spectra and the large lifetime broadening inherent to many carbon systems. Both of these problems are effectively mitigated by turning to O Kα RXES spectroscopy to probe the functional groups separately. This will be particularly effective for differentiating the two allotropes of epoxide, BB-epoxide and its more commonly understood cousin, total triangle epoxide (TT-epoxide).

Before the O Kα RXES experiment can be used to probe the different epoxide allotropes, however, the proper excitation energies are needed. The resonant excitation energy for TT-epoxide is 287.4 eV, and we suspect the resonant excitation energy of BB-epoxide to be 288.2 eV on the C 1s threshold. Equivalent resonant excitation energies on the O 1s threshold were determined by shifting the O 1s XANES spectrum of GOp by -246.1 eV so that it matched, peak for peak, its C 1s XANES spectrum as shown in Figure 4.3(a) and (b), under the constraint that the relative spacing between peaks lined up in this fashion would remain constant on both edges. The justification for this approach is that, regardless of which edge one is exciting, one is promoting core electrons into the same anti-bonding states that are shared when C and O atoms bond. The idea that the unoccupied states should align should also apply to the occupied states, because the valence C pDOS and O pDOS are also heavily hybridized. The comparisons between the C Kα and O Kα spectra (shifted down by 246.1 eV like the O 1s XANES spectra) of the three samples are shown in the bottom six panels of Figure 4.3. The excellent alignment of the elastic peaks and some prominent inelastic features shows how well the 246.1 eV shift brings the two edges together.

Applying the 246.1 eV shift to the C 1s binding energies of 287.4 eV and 288.2 eV needed to resonantly excite the TT-epoxide and BB-epoxide groups, one should excite at approxi-

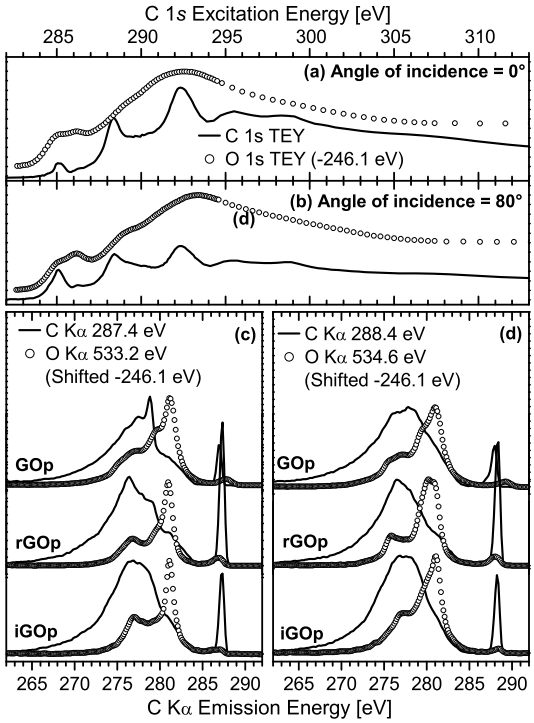

Figure 4.3: Threshold alignment of C and O states. High-resolution C 1s and O 1s XANES measured on GOp at (a) 0° and (b) 80°. Each O 1s XANES spectrum was shifted down in energy by 246.1 eV to line it up with its counterpart C 1s XANES spectrum. In panel (c), the O Kα spectra measured at 533.2 eV on GOp, rGOp, and iGOp, respectively, were shifted by -246.1 eV to compare to the C Kα spectra measured at 287.4 eV. Similarly, in (d), the O Kα spectra measured at 534.6 eV were shifted by -246.1 eV to compare to the C Kα spectra measured at 288.3 eV. Visual inspection shows that there are many peaks common between the two edges, which is what one would expect from strongly hybridized states shared by the oxygen and carbon sites.

mately 533.5 eV and 534.3 eV, respectively. In reality, after careful calibration of the data post-experiment, the samples were excited at 533.2 eV and 534.6 eV. The influence of carboxyl and water were qualified using spectra taken from published liquid cell experiments of acetic acid [86] and water [87]. Neither TT-epoxide nor BB-epoxide, however, have published representative O Kα RXES spectra, so the molecular DFT code StoBe was used to simulate spectra of these two functional groups using simple representative molecules. Figure 4.4 shows the comparison of the 533.2 eV and 534.6 eV O Kα RXES spectra measured from the graphene oxide paper samples against those real and simulated component spectra.

As expected, the simulated TT-epoxide molecule XES spectrum reproduced the peak structure that one sees at 533.2 eV excitation energy with surprising accuracy for all samples, despite the simplicity of the model, as Figure 4.4(c) clearly shows. The TT-epoxide simulation best models the spectrum of iGOp, but suffers when compared to GOp and rGOp largely because of peak *e*. Peak *e* at 533.2 eV emission energy lines up with the strong, narrow peak labeled H_2O in Figure 4.2(e), which suggests that peak *e* is also due to the chemisorption of water. This conclusion is strengthened by the fact that peak *e* is the most intense for GOp. A lessened peak *e* in iGOp thus suggests less water content per functional group in iGOp as compared to GOp and rGOp.

Proof that BB-epoxide is present in rGOp is seen in Figure 4.4(d). Comparisons to O Kα RXES spectra of water and acetic acid show these two functional groups do indeed contribute to the all three spectra. However, neither water nor carboxyl can explain peak *c*. Indeed, the only reasonable explanation for this feature is given by the BB-epoxide molecule simulation, which gives an intense feature at approximately this energy. (It should be noted that carbonate produces a strong spectral line at this energy as well, but carbonate has not been seen by any other author to the best of our knowledge.) The TT-epoxide model also shows this feature, but its relative intensity is too small to account for peak *c* in the 534.6 eV spectra of GOp and rGOp. The functional group that is resonantly excited at either 288.2 eV on the C 1*s* edge or 534.3 eV on the O 1*s* edge is clearly BB-epoxide.

There is a clear pattern seen. In a sample with a strong TT-epoxide signal, the BB-epoxide signal is weak (iGOp), whereas in a sample with a strong contribution from BB-epoxide, the TT-epoxide component is weak (rGOp). This pattern is unrelated to the initial chemistry

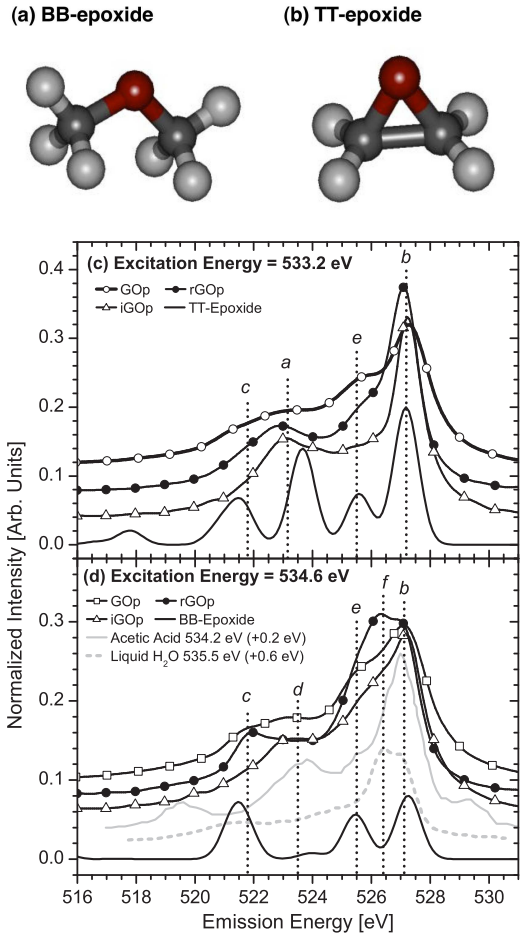

Figure 4.4: Component spectra that contribute to GOp, iGOp, and rGOp O Kα RXES spectra. (a) Broken bond epoxide (BB-epoxide) (b) Total triangle epoxide (TT-epoxide). In both panels, oxygen is colored black, carbon is dark grey, and hydrogen is light grey. Hydrogens were included to pacify the remaining carbon bonds. (c) Comparison of 533.2 eV O Kα spectra from all three samples to calculated TT-epoxide. (d) Comparison of 534.6 eV O Kα spectra from all three samples to calculated BB-epoxide, a digitized water spectrum from Ref. 87, and a digitized acetic acid spectrum from Ref. 86. The simulations in (c) and (d) were shifted such that the highest-intensity peaks in theory and experiment lined up.

of the samples because iGOp was not intercalated with dodecylamine until after the sample had been created in the same manner as GOp. If initial chemistry was the deciding factor, then iGOp and GOp should be very close. Thus, BB-epoxide is most likely the result of aging. Because epoxide is mobile at room temperature, epoxide functional groups can hop along the graphene lattice, if there is sufficient room, and align. As mentioned previously, the mechanism that promotes the unzipping of the graphene lattice is still in dispute. Li *et al.* calculated that epoxides would spontaneously diffuse together, line up, and fracture the lattice because alignment was energetically favorable [39]. Sun *et al.*, however, argue that an BB-epoxide trimer is necessary first as a nucleation site, which then will draw other epoxides near to continue the process [70]. Indeed, nucleation seems vital to many of the oxidation reactions involving graphene oxide, from the initial oxidation of graphite through to thermal reduction [88]. Other authors argue that unzipping begins at the surface [89]. Nevertheless, the fact that BB-epoxide intensity grows while TT-epoxide intensity shrinks fits with the idea that TT-epoxide is being consumed over time as BB-epoxide fractures form.

The conspicuous lack of BB-epoxide in the spectra of iGOp suggests that intercalation prevents the development of BB-epoxide. Although there is some debate about how the process is initiated, all authors agree that diffusion of epoxides or other atomic oxygen species is necessary for linear defects to form beyond the initial nucleation sites. It would seem that intercalation, in particular with dodecylamine, inhibits the diffusion process. Ultimately, more testing with intercalation is necessary, particularly with other suitable intercalants.

4.1.4 Conclusions

We have shown that hydroxyl functional groups have a tendency to bunch together in zones of dense functionalization, whereas epoxides (at least initially) disperse move evenly. This leaves the hydroxyl functional groups electronically isolated from the non-functionalized carbon sites. The non-functionalized carbon states, on the other hand, exhibit very similar spectral characteristics when comparing GOp and rGOp. This shows that the carbon states are substantively identical before and after reduction. Although reduction does increase the $sp2/sp3$ ratio, distortions that remain on the carbon lattice prevent the emergence of true pristine graphene states.

We have also identified BB-epoxide, an allotrope of the epoxide functional group that breaks the carbon basal plane in graphene, which has been theorized to exist and observed in other carbon allotropes such as nanotubes. The spectral fingerprint of BB-epoxides is distinct and easily resolvable when observed using C $1s$ XANES and O Kα RXES spectroscopic techniques. The advent of BB-epoxide is the result of epoxides hopping along the graphene sheet over time, and is thus an aging effect. Reduction serves to make this aging effect more pronounced, whereas intercalating graphene oxide paper with dodecylamine seems to stay the process. Intercalation also tends to produce a more ordered sample, which may be a result of the intercalation process directly or perhaps represents a benefit of inhibiting formation of BB-epoxide defect lines. The overall significance is that, unless this kind of aging effect is properly mitigated during graphene oxide-based device fabrication, or at least taken into account when considering the characteristics of the device over its full lifetime, then the performance of said device may suffer deleterious degradation.

The work presented here offers important insight into how the functional groups affect the graphene basal plane as well as how one may control the form in which the functional groups present themselves, particularly epoxide. However, graphene oxide research has not yet advanced to the point where one may reliably know parameters such as the band gap and carrier mobility within a graphene oxide sample without extensive characterization and analysis. More experimentation and accurate simulation is clearly needed, and the subject of ongoing research.

4.1.5 Experimental

Experimental measurements

The RXES measurements, as well as some of the XANES spectra, on the carbon and oxygen K edges were performed at Beamline 8.0.1 at the Advanced Light Source at the Lawrence Berkeley National Laboratory using the soft X-ray fluorescence (SXF) endstation [59]. Emitted radiation was measured using a Rowland circle type spectrometer with a large spherical grating and a photon-counting area detector. The total experimental resolution was 0.3 eV FWHM. The C K and O K XANES spectra were measured in total electron yield mode. The

fluorescence measurements were made using a depolarized configuration, which means that the vector E of the incidence beam lies at the scattering plane, i.e. p-polarization was used. The SXF endstation is configured such that the path of the emitted photons that can be detected by the spectrometer and the incident beam are perpendicular to each other. All C K and O K XANES spectra measured at the ALS were normalized to the current generated in a highly transparent gold mesh upstream of the sample.

High-resolution XANES spectra on the C K edge were measured at the Spherical Grating Monochromator (SGM) beamline at the Canadian Light Source. The spectra were measured in both total electron yield and total fluorescence yield modes. Instead of normalizing to an upstream mesh current, however, the spectra were instead normalized to the current generated in a photodiode. This photodiode current spectrum was not taken simultaneously with the sample spectrum, but rather directly afterwards. This technique allows one to directly measure the light intensity hitting the sample as a function of energy, which allows one to correct for the problem of a carbon-contaminated mesh introducing false features into carbon spectra.

Experimental TICS ratios

Normalization of a spectrum to its total integrated counts per second (TICS) is a very useful analytical technique as it provides a useful unit for the ordinate of a spectrum. Rather than simple counts, the ordinate is now the probability density of the energy that a photon will have per radiative decay event that involves spectator (valence) electrons. In the one-electron picture with no scattering, which holds remarkably well for non-correlated systems like organic compounds, the inelastic component of a spectrum is directly proportional to the occupied density of states of that system. Thus, the ordinate units can be interpreted as the probability density that an electron from a particular part of the density states will refill the core hole in a radiative decay event.

Each spectrum was normalized to its TICS value in the following way. The spectrum was first smoothed with an FFT filter. Background counts were then removed by subtraction of an appropriate parabolic background function as defined by the noise floor within the spectral measurement window but outside of the spectrum. Each spectrum was then normalized to

the integrated intensity of the inelastic portion of that particular spectrum. The elastic peak contributions were isolated and removed by Gaussian peak fitting.

If one were to stop here, then one could examine the distribution of the occupied states (valence electrons) in energy space within one system, and how that distribution differs from that of another system, but any quantitative comparison between systems at a given energy level is impossible. Therefore, each spectrum taken from samples rGOp and iGOp at a given energy was renormalized to the TICS of the GOp spectrum measured while exciting at the same energy. The TICS value is directly proportional to the rate of core hole creation, so by normalizing all spectra to the same TICS value, then the TICS values all reflect the probability of a photon being produced at a given energy level for the same core hole creation rate. In short, the ability of the system to absorb incoming photons is removed from the problem, and comparing RXES spectra measured on different samples takes on a quantitative aspect as one directly measures the relative differences in density of states at a given energy.

Theoretical calculations

The simulated XES spectra for BB-epoxide and TT-epoxide shown in Figure 4.4 were calculated using StoBe. This program implements Kohn-Sham DFT with both auxiliary and orbital basis sets based on the Huzinaga basis sets originally developed for Hartree-Fock calculations [90]. The orbital sets used were triple-ζ plus valence polarization (TZVP) sets containing sets of *s*-, *p*-, and *d*-type functions in the form $(ns/np/nd)$. The exact sets used are contained within the StoBe library and were (7111/411/1) for O and C, and (41/1*) for H. The auxiliary basis sets use blocks of *s*-type and *spd*-type functionals to model the density (d) and exchange correlation (ex) functionals in the form of (exs,$exspd$;ds,$dspd$), with (5,2;5,2) used for O and C, and (3,1;3,1) for H. For comparison with measurements, the simulated oxygen spectra were broadened by convolution with Gaussian functions with FWHM of 1.0 eV. Table 4.3 lists the coordinates of the atoms used in each of the simulations.

4.1.6 Acknowledgements

All samples were made by Sasha Stankovich (at the Department of Chemistry, Northwestern University, USA). We acknowledge support by the Natural Sciences and Engineering Re-

Table 4.3: Atomic coordinates for BB-epoxide and TT-epoxide simulations. All distances are given in Å from the origin.

TT-epoxide				BB-epoxide			
Atom	X	Y	Z	Atom	X	Y	Z
O1	-6.366	0.997	0.381	O1	-5.989	1.478	0.871
C1	-7.252	2.137	0.435	C1	-6.867	2.468	0.340
C2	-7.246	1.140	1.518	C2	-6.540	0.870	2.037
H1	-6.759	3.105	0.588	H1	-7.842	2.031	0.036
H2	-6.751	1.378	2.467	H2	-6.376	2.896	-0.546
H3	-8.058	0.404	1.580	H3	-7.060	3.277	1.073
H4	-8.069	2.133	-0.297	H4	-5.810	0.133	2.395
				H5	-7.496	0.353	1.816
				H6	-6.723	1.616	2.836

search Council of Canada (NSERC), the Canada Research Chair program and the Russian Foundation for Basic Research (Projects 11-02-00022). The Canadian Light Source is supported by NSERC, the National Research Council (NSC) Canada, the Canadian Institutes of Health Research(CIHR), the Province of Saskatchewan, Western Economic Diversification Canada, and the University of Saskatchewan. The Advanced Light Source is supported by the Director, Office of Science, Office of Basic Energy Sciences, of the U.S. Department of Energy under Contract No. DE-AC02-05CH11231.

Table 4.4: TICS and Incident Flux for GOp for all RXES and nRXES spectra

TICS and Incident Flux for GOp				
Excitation Energy [eV]	Total Intensity	Count Time [s]	TICS [s^{-1}]	Incident Flux [A]
285.0	9588	240	39.95	1.21E-08
286.0	16276	240	67.82	1.41E-08
286.4	17936	240	74.73	1.43E-08
287.4	18311	240	76.30	1.46E-08
288.4	20376	240	84.90	1.59E-08
289.3	19336	240	80.56	1.71E-08

Table 4.5: TICS and Incident Flux for rGOp for all RXES and nRXES spectra

GOp				
Excitation Energy [eV]	Total Intensity	Count Time [s]	TICS [s^{-1}]	Incident Flux [A]
285.0	9687	240	40.36	2.98E-08
286.0	13859	240	57.75	4.23E-08
286.4	14245	240	59.35	4.36E-08
287.4	14817	240	61.74	4.40E-08
288.4	15944	240	66.43	4.40E-08
289.3	16265	240	67.77	4.37E-08

4.2 Supplemental Analysis: TICS ratio details

The paper reports the use of TICS ratio analysis to arrive at appropriate scaling factors for comparison of the RXES spectra, but there was neither sufficient space nor cause to go into detail about how it is that it was accomplished. To compute the experimental renormalization factors I_{exp}^{Renorm}, both XES and XANES spectra of the samples under comparison (in this case, GOp, rGOp, and iGOp) must be analyzed to extract necessary information. To begin, Table 4.4, Table 4.6, and Table 4.5 detail the measured incident flux and calculated TICS for each spectrum. As in the paper, all samples will be renormalized with respect to GOp. Note that all spectra are displayed in the paper, and will not be replicated here.

Now we have the TICS and the flux. We now need the XANES spectra to extract η^{mass} and η^{rad}. As with the XES data, the XANES data are in the paper, and will not be reproduced here. The process used to arrive at these numbers is discussed in Section 3.2.2.

Table 4.6: TICS and Incident Flux for iGOp for all RXES and nRXES spectra

GOp				
Excitation Energy [eV]	Total Intensity	Count Time [s]	TICS [s^{-1}]	Incident Flux [A]
285.0	7748	180	43.05	2.97E-08
286.0	10934	180	60.75	3.55E-08
286.4	11607	180	64.48	4.38E-08
287.4	13382	180	74.35	4.42E-08
288.4	13896	180	77.20	4.56E-08
289.3	14210	180	78.95	4.61E-08

Table 4.7: Calculation of η^{mass} and η^{rad} to be used for computation of I_{exp}^{Renorm}

Sample	η^{rad}	η^{mass}
GOp	0.695	0.795
iGOp	0.221	0.816
rGOp	0.220	0.797

Table 4.7 lists the results of the computation of the necessary efficiencies.

Assuming that the efficiency of the spectrometer does not change between samples, we now have all of the necessary information to compute the experimental probability ratios, I_{exp}^{Renorm}. The results are shown later in Table 4.9.

Next, these results must be compared to theoretical results computed within the framework built in Section 3.2.3. According to Equation (3.16), the relative functional group populations are required. As stated in the paper, the C:O ratios, as determined by D. Dikin, are listed in Table 4.8. The relative bond populations for a given symmetry axis can be derived using this information. The $\hat{z}$-axis is populated by C-OH (hydroxyl), C-O-C (epoxide), and π-symmetry C-C bonds, whereas the xy plane contains C-COOH (carboxyl) and σ-symmetry unfunctionalized C-C bonds. The relative bond populations are shown in Table 4.9.

We also require the relative occupancy of the unoccupied C pDOS states for each of the groups, given that this will affect the efficiency of core hole creation. Carbon that is functionalized with an oxidizing group will have fewer electrons in the valence shell due to charge transfer, so the value of n_i in Equation (3.16) will be greater than one. Using simulations from WIEN2k, carbon atoms bonded to hydroxyl groups lose about 0.45 electrons,

Table 4.8: C:O Characterization for GOp, rGOp, and iGOp

Sample system	Overall ratio C(graphene):O	Ratios for oxygen-containing groups		
		Epoxide	Hydroxyl	Carbonyl/Carboxyl
GOp	2.9	4.9	19.3	11.15
iGOp	2.6	5.8	18.6	6.3
rGOp	5.0	16.7	9.8	26.3

Table 4.9: Comparison of I_{exp}^{Renorm} and I_{theo}^{Renorm} calculations. The ratios were computed with respect to GOp. Relative bond populations for each of the major functional group types for the calculation of I_{theo}^{Renorm}

Ratio	$C(H+E)$	$C(\pi^*)$	$C(C)$	$C(\sigma^*)$	I_{exp}^{Renorm}	I_{theo}^{Renorm}	I_{theo}^{Renorm} (x2 n_i)
GOp	0.46	0.54	0.09	0.91	1.00	1.00	1.00
iGOp	0.40	0.60	0.16	0.84	1.01	1.00	1.03
rGOp	0.22	0.78	0.04	0.96	0.90	0.98	0.90

whereas carbons bonded to epoxides lose about 0.40 electrons. In both cases, the C:O ratio was kept to 2:1. No simulation using carboxyl has been done, so a quantitative estimation of the graphene-to-carboxyl charge transfer was not possible. Assuming that carboxyl does not oxidize as strongly as either an epoxide or an hydroxyl group, we estimated the charge transfer at about 0.2 electrons. Using the relative bond populations and the relative electron density, the theoretical probability ratios I_{theo}^{Renorm} can be computed; the results are shown in Table 4.9 in the column labeled I_{theo}^{Renorm}.

The experimental and theoretical probability ratios compare reasonably well, particularly for the iGOp/GOp renormalization factor. The rGOp factor is 8% too high, but this can be fixed by doubling the n_i factors. (These results are shown in the last column of Table 4.9. Doubling the n_i factors does not imply that the carbon sites have lost extra charge, but rather, it is a mathematical way of introducing the idea that the overall C:O ratios reported in Table 4.8 are too low. Indeed, two of the manuscripts included in this thesis have shown that water has a relatively strong impact on the DOS *via* non-covalent functionalization. The water content was not included in the C:O ratios. The model as reported is too simple to include water, but inclusion of water would undoubtedly gives stronger weight to the functional groups. The x2 factor is meant to account for the further oxidization of the carbon

basal plane due to other, unreported interactions with water and possibly other functional groups not yet considered.

Regardless of treatment method, the iGOp/GOp ratio was always very close. This is encouraging, given the fact that the two samples are so similar in terms of functionalization. The fact that the two samples have such dissimilar electronic structure emphasizes the fact that the effects of interaction between groups cannot be understated. Although the number of states may be the same, the distribution of those states (in other words, the DOS) may be entirely different.

Chapter 5

Modulation of the band gap of graphene oxide: The role of AA-stacking

If one stacks sheets of graphene to make graphite, the interaction between sheets of graphene causes a significant difference in the band structure of the material: The Dirac cone near the Fermi level in graphene is lost, and with it many of the remarkable properties that define graphene. However, different stacking modes affect the multilayered graphene in different ways. Stacking GO sheets into multilayered GO also has a significant effect on the electronic structure of the overall material. Just like with graphene, the different stacking modes do not change the multilayered GO in the same way. If one controls the stacking mode appropriately, one can control the band gap.

The two main stacking modes found in graphite are AA-stacking and AB-stacking, shown in the manuscript in Figure 5.1. AB-stacking, also called Bernel stacking, is energetically favoured and will be the dominant phase in HOPG. However, AA-stacking will also be present. Whether or not one considers AA-stacking to be a defect is a matter of perspective. Multilayered graphene that is made through chemical vapour deposition (CVD), the amount of AA-stacking can be quite significant simply because of the way in which is it created.

We performed DFT simulations of the electronic structure of graphite, in both AA-stacking and AB-stacking modes, as well as bilayered graphene, to understand how stacking affects the DOS. The results for both the bulk AA-stacked graphite and AA-stacked graphene showed that the density of near-Fermi states, states that ultimately control the band gap, is not affected overmuch. However, the main π^* resonance at 285.4 eV is strongly affected. In short, AA-stacking causes the π^* states to flatten and spread out. The degree to which the π^* states spread is controlled by the interlayer spacing: The closer the AA-stacked graphene

sheets are to one another, the broader the π^* feature becomes. AA-stacked graphene sheets prefer to be farther apart than if stacked in an AB configuration. But, if AA-stacked graphene sheets were forced to assume the interplanar distance of AB-stacked graphite - roughly 3.348 $\mathring{A}$ - then features arise at roughly 284.8 eV, and 285.6 eV.

C 1s XANES measurements of multilayered pristine graphene show that stacking does build states at those energies. Eight samples were compared: two each of graphene, bilayer graphene, a third sample with 4 to 6 layers of graphene, and a fourth with 10 or more layers, referred to as Gr, 2Gr, 4Gr, and 10Gr. One set was taken as is, and the second set was annealed at 900 °C. The growth of DOS around 284.8 eV and again at around 285.6 eV in the spectra of both of the 10Gr samples showed strong evidence that the features are a result of stacking. The simulations show that these features are due to AA-stacking, specifically, AA-stacked graphene that has been forced close to one another.

Although interesting, the effect of AA-stacking on the band structure of multilayered graphene matters not in terms of the band gap, for the band gap is determined not by the width of the π^* feature. For the band gap of graphene oxide, however, the shape of the π^* resonance strongly affects the band gap because because the π^* resonance forms the bottom of the CB in highly oxidized samples. This is because all of the near-Fermi states that give graphene its status as a zero band gap semiconductor have all been removed to form bonds with oxidizing functional groups. C 1s XANES measurements of both GO and reduced GO (rGO) show features at 284.6 eV and 285.4 eV, about where the π^* resonance is predicted to divide if under the influence of AA-stacking.

Not surprisingly, remnants of the π-conjugated network of non-functionalized carbon states still determine the band gap, even in a highly oxidized environment. However, non-functionalized does not mean unaffected. The near-Fermi states have been removed due to oxidization, but the π^* feature remains, and therefore its width determines the band gap. AA-stacking is clearly an important piece of the puzzle. In the case of rGO, removal of functional groups *via* reduction with hydrazine has allowed for some reconstruction of π-conjugation and a concomitant decrease in the band gap because more near-Fermi states are present. The width of the π^* feature no longer determines the width of the band gap. Nevertheless, AA-stacking features are quite strong in the rGO XANES spectrum, suggesting

that AA stacking is the dominant mode of stacking in multilayered graphene oxide.

This work has been published in the journal *Carbon* (Modulation of the band gap of graphene oxide: The role of AA-stacking. *Carbon* **66** (2014) 539–546). Legal permission to reproduce this work is included in Appendix A. The following list delineates the contributions of each author to the complete paper.

A. Hunt:

- Measured all C Kα nRXES data and all C 1s XANES spectra for both samples
- Made all figures, and wrote most of the text of the manuscript
- Performed all WIEN2k simulations and second derivative analysis

D. Dikin:

- His group made the rGO and GO samples
- Contributed writing suggestions and editing

E. Kurmaev:

- Responsible for original motivation of the project and procurement of the GO samples
- Wrote the original introduction
- Aided in literature review

Y. H. Lee:

- Ph.D. supervisor for N. V. Luan
- Contributed to the direction and purpose of the manuscript

N. V. Luan:

- Made the multilayered pristine graphene samples and transported them from Korea
- Helped measure the spectra at the SGM beamline
- Originally suggested looking at AA-stacking as a possible contributor to the spectra based upon his knowledge of the sample creation methods

G. S. Chang:

- Close collaborator with Y. H. Lee
- Contributed strongly to the editing process
- Aided in the analysis

A. Moewes:

- Ph.D. supervisor of A. Hunt
- Integral to the writing of the first manuscript
- Aided in the interpretation of the spectra
- Provided all necessary resources

5.1 Manuscript

Modulation of the band gap of graphene oxide: The role of AA-stacking

A. Hunt,[1] D. A. Dikin,[2] E. Z. Kurmaev,[3] Y. H. Lee,[4] N. V. Luan,[4] G. S. Chang,[1] A. Moewes[1]

[1]Department of Physics and Engineering Physics, University of Saskatchewan, 116 Science Pl, Saskatoon, Saskatchewan, Canada S7N 5E2
[2]Department of Mechanical Engineering, Northwestern University, 2145 Sheridan Road, Evanston, Illinois, USA 60208-3111
[3]X-ray Emission Spectroscopy Lab, Institute of Metal Physics, RAS Ural Div., 18 Kovalevskoi Str., 620990 Yekaterinburg, Russia
[4]Department of Energy Science (DOES), Sungkyunkwan University, Suwon, 440-746, Korea

*Corresponding author. Email: adrian.hunt@usask.ca (A. Hunt)

5.1.1 Abstract

The unique electronic properties of graphene make it an advantageous material for use in many applications, except those that require a band gap. Much work has been done to introduce an appropriately tuned band gap into graphene, including uniaxial strain and oxidation, with varying levels of success. We report here that the stacking configuration of the sheets in multilayered graphene oxide can have a significant impact on the band gap. Through comparison of X-ray absorption near-edge spectra of multilayered pristine graphene sheets with spectra simulated using DFT, we have found that AA-stacking pushes unoccupied states closer to the Fermi level than AB-stacking by widening the π^* resonance in both graphene oxide and graphene. If the near-Fermi states have been removed such that the nearest unoccupied state to the Fermi level is the π^* band, then AA-stacked multilayered graphene oxide will have a smaller band gap than AB-stacked graphene oxide. We have confirmed this by measuring the band gap of graphene oxide and reduced graphene oxide indirectly using X-ray absorption near-edge spectroscopy and X-ray emission spectroscopy. Controlling the stacking configuration of multilayered graphene oxide may provide a novel method for tuning its band gap.

5.1.2 Introduction

Graphene is a monolayer of graphite wherein the carbon atoms form a two-dimensional (2D) hexagonal structure (the honeycomb lattice). The material is of great interest because of its exceptional electrical, mechanical and thermal properties. Graphene has been suggested for use in technological applications such as nanoelectronics, sensors, supercapacitors, and hydrogen storage [6, 91, 92]. In applications to photovoltaics, graphene-based materials have been used as a light collector in organic solar cells [65], as a transparent conductor to replace the ubiquitous ITO [83], and as a intermediate conducting layer in tandem solar cells [61]. Many techniques have been developed to make graphene sheets, such as mechanical cleavage of graphite, chemical vapor deposition, and thermal fusion of polycyclic aromatic hydrocarbons. Among them, the most promising method for mass production of graphene is exfoliation of graphite oxide in a polar solvent, followed by reduction of the harvested graphene oxide (GO) sheets, although many methods have been proposed to accomplish this [93, 94]. However, more than just a precursor material for graphene, GO itself has very interesting properties and can be used in polymer composites [95] and dielectric layers in electronic devices [96]. Indeed, GO has shown to be a better transparent conducting film than graphene in solar cell applications [97,98]. GO can be applied used in various biological applications [99], for example, GO-Fe_3O_4 nanoparticles can be used for drug delivery and release [100].

For electronic device applications [20], a band gap is required to control the type and concentration of carriers, however, graphene is a zero-gap semiconductor [2]. There are numerous methods by which one may introduce a band gap into graphene [89,101]. However, a natural point where one may study how to engineer the band gap of graphene is GO, given its role in the preparation of graphene. GO has a finite electronic band gap due to oxidization of the carbon basal plane by oxygen-containing functional groups: phenol, hydroxyl, and epoxide groups on the plane and carboxylic groups at the lateral edge [26, 27]. Interestingly, the effect that the stacking arrangement of the graphene oxide sheets has on the band gap of multilayered GO has not been studied, despite the fact that $\pi-\pi$ overlap between graphene and functionalizing adsorbed aromatics is known to alter electrical characteristic of graphene [102]. There are many possible graphene stacking configurations, but two of the

most important are the AB-stacking (Bernel stacking) and the AA-stacking configurations. The two stacking configurations are shown in Fig. 5.1. The images in Fig. 5.1 were made using VESTA [103]. AB-stacking is the lowest-energy configuration, and this is the dominant stacking mode found in highly-oriented pyrolytic graphite (HOPG). It is known that the way in which graphene sheets stack has a significant impact on the vibronic structure of multilayered graphene sheets [104]. Given that the states that frame the band gap in GO will also be located in the interplanar region, it stands to reason that the way in which the layers interact will affect the band gap. This work studies that very interaction.

We have been studying the many facets of the electronic and physical structure of graphene oxide [44]. Here, we probe the band gap of multilayered GO (simply referred to as GO henceforth) and GO that has been reduced with hydrazine hydrate (rGO). The band gap is studied indirectly through a combination of X-ray absorption near-edge fine structure (XANES), to probe the unoccupied partial density of states (pDOS), and non-resonant X-ray emission spectroscopy (XES), to probe the occupied pDOS. Plotted on a common energy scale with respect to the core hole, the band gap is the energy separation between XES and XANES. These techniques boast site- and chemical-specificity that other techniques do not possess, and the transition probabilities are not modified by Franck-Condon factors like optical gap measurements, allowing for a detailed and unambiguous study of the carbon states that populate the near-Fermi energy regime.

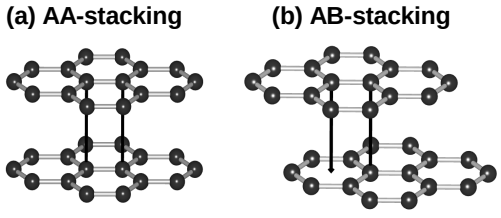

Figure 5.1: The AA- and AB-stacking configurations for graphite and multilayered graphene.

5.1.3 Experimental

XES Measurements

The XES measurements on the carbon 1s edges were performed at Beamline 8.0.1 at the Advanced Light Source at the Lawrence Berkeley National Laboratory using the soft X-ray fluorescence (SXF) endstation [59]. Emitted radiation was measured using a Rowland circle type spectrometer with a large spherical grating and a photon-counting area detector. The total experimental resolution was 0.3 eV FWHM. The fluorescence measurements were made using a depolarized configuration, which means that the vector E of the incidence beam lies at the scattering plane, i.e. p-polarization was used. The SXF endstation is configured such that the path of the emitted photons that can be detected by the spectrometer and the incident beam are perpendicular to each other.

XANES Measurements

High-resolution XANES spectra on the C 1s edge were measured at the Spherical Grating Monochromator (SGM) beamline at the Canadian Light Source [105]. The GO X-ray absorption near-edge spectra (XANES) were measured in total electron yield (TEY) and total fluorescence yield (TFY) modes. The graphene XANES spectra, however, were also measured in partial fluorescence yield (PFY) mode. The PFY spectra were measured using a silicon drift detector (SDD) that acted as a very low-resolution spectrometer (FWHM $\approx$ 150 eV). Integrating all counts detected by the SDD would yield a TFY spectrum, whereas isolating only the emission line from carbon produces a C 1s PFY spectrum. This was necessary in this case because the graphene and multilayered graphene samples were mounted on SiO_2 substrates. Second order contamination from the monochromator allows for near-resonant excitation of the O sites in the SiO_2 substrate, as the O 1s absorption threshold lies at nearly twice the energy of the C 1s edge. Although second order light from the monochromator is significantly weaker than the first order light that resonantly excites the graphene, the SiO_2 substrate has orders of magnitude more oxygen than the graphene layers has carbon. Thus, O Kα from the substrate strongly competes with the C Kα emission from the graphene.

For normalization, in all cases, the PFY, TFY, and TEY spectra were normalized to

the current generated in a photodiode when this photodiode was exposed to the incident beam. This photodiode current spectrum was not taken simultaneously with the sample spectrum, but rather directly afterwards. This technique allows one to directly measure the light intensity hitting the sample as a function of energy. This method allows one to correctly account for intensity fluctuations in the incident beam due to carbon contamination on all optically active beamline components. Such contamination can introduce false features into carbon spectra.

Graphene synthesis

Eight samples of pristine graphene mounted on SiO_2 substrates were prepared: two each of graphene, bilayered graphene, multilayered graphene with four to six layers, and multilayered graphene with ten or more layers. One sample from each of the four pairs was annealed at 900° C. The graphene samples were grown using the atmospheric pressure chemical vapor deposition (APCVD) method. Copper foil (from Nilaco, 99.96%) with a thickness of 100 μm was used as the substrate for monolayer graphene growth; bilayer and multilayer graphene was grown on 70 μm copper foil. The chamber was preheated to 1060° C with 1000 sccm of Ar and 200 sccm of H_2 and annealed for 40 min. After that, the rate of gas injection was altered depending on the desired characteristics of the graphene film. In the case of monolayer graphene, the H_2 gas injection rate was reduced to 10 sccm from 200 sccm, and 3 sccm of methane gas was injected. For bilayer graphene, the H_2 and methane gas injection rates were 70 sccm and 30 sccm, respectively. The growth time for both mono and bilayer graphene was 5 minutes. For multilayered graphene, we maintained 200 sccm of H_2 gas flow and injected only 3 sccm of methane. Growth time was increased to 15 min. Methane and H_2 gas inflows were then stopped and the sample was cooled down to room temperature. After growth, the finished samples were transferred to SiO_2 substrates using copper etchant.

5.1.4 Results

The GO sample was prepared as in the manner of GO paper from water filtration. The rGO sample was prepared as the first, but during the process, the water was substituted with DMF and hydrazine was added. The sample was heated and reduced in solution, then finally

filtered. Further details on the general synthesis technique are published elsewhere [17, 67]. These samples were chosen because reduction of GO is a necessary step if one wishes to achieve graphene from graphene oxide. Incomplete reduction can provide a way to modulate the oxidization level, and thus the band gap of GO.

As mentioned earlier, we probed the electronic states of the two samples using XES and XANES for the purposes of determining the band gap. The XES spectra were measured at Beamline 8.0.1 at the Advanced Light Source [59], while the XANES spectra were measured at the SGM beamline at the Canadian Light Source [105]. Fig. 5.2 shows the results of our experiments. In this Figure, the non-resonant C Kα XES spectrum and the C 1s XANES spectrum from each sample is plotted on the same energy axis, each in a separate panel. In terms of the energy axis, both the C 1s XANES and the C Kα XES spectra are both measured with respect to the C 1s core state. Thus, aligning the XANES and XES spectra on the same energy axis simply requires each to be calibrated to a known reference. All XANES spectra shown in this work were aligned to a sequentially measured XANES spectrum of HOPG. All XES spectra were similarly aligned to HOPG.

The XANES spectra were measured in both total electron yield (TEY) and total fluorescence yield (TFY) modes. The TEY technique involves counting electrons emitted from the sample via Auger decay, whereas the TFY technique requires one to count the photons emitted from the sample via radiative decay. Ideally, the intensity of emission of both electrons and photons scales linearly with the number of core holes created. When this holds true, TEY and TFY are both direct measures of the true absorption profile. In practice, however, there are two important caveats. The escape depth of Auger electrons is very shallow, which means that TEY spectra are very surface-sensitive. TFY is much more bulk-sensitive due to the longer escape depth of the emitted photons. However, when exciting the sample on a strong resonance, such as the C $1s - 2\pi^*$ feature in graphite, the rate of core hole creation does not increase linearly with a concomitant increase in absorption cross-section, and the TFY signal saturates at strong resonance features [54]. This leads to a characteristic 'squishing' of high-intensity features. In order to correct for saturation effects, the displayed TFY spectra have been treated using the correction method of Eisebitt *et al* [106, 107].

The second derivative method was chosen to analyze the band gap of GO. The second

derivative is particularly useful for analyzing the pre-edge of a spectrum because weak but sharp features show much more prominently in the second derivative than broad yet strong features. This property helps to extract details from the near-Fermi portions of the XES and XANES spectra. Other researchers have successfully determined the band gaps of various materials indirectly using a combination of XANES and XES [108–110]. Calculating the second derivatives of XANES and XES spectra has proven to be an accurate and highly reproducible method of finding the band onsets, and thus the band gaps [41, 111–113].

Minima in the second derivative correspond to features (maxima) in the spectrum. The band gap is therefore the energy separation between the highest-energy minimum in the second derivative of an XES spectrum (denoted d^2XES/dE^2) and the lowest-energy minimum in second derivative of an XANES spectrum. Depending on how the XANES spectrum is measured (TEY or TFY), the second derivative is denoted d^2TEY/dE^2 or d^2TFY/dE^2.

With this understanding of the second derivative method in mind, let us turn to the d^2XES/dE^2, d^2TEY/dE^2, and d^2TFY/dE^2 spectra of GO and rGO, displayed within the insets of each panel in Fig. 5.2. Before a discussion concerning the band gaps of the samples can begin, however, the differences in the d^2TEY/dE^2 and d^2TFY/dE^2 spectra of each sample is striking, particularly in the 284.5 to 286.5 eV range. For both samples, the d^2TEY/dE^2 shows only one minimum, at about 285.2 eV, whereas the d^2TFY/dE^2 shows a double-dip structure, with one minimum at 284.6 eV, the other at 285.6 eV. This double-dip structure in the TFY is not due to saturation, as saturation cannot introduce structure into a spectrum [54]. Neither is the difference in shape due to a normalization artifact from a contaminated mesh, as all XANES spectra were normalized using an asynchronously measured photodiode spectrum of the incident light to act as a background reference [114]. Thus the difference in shape between the TEY and TFY spectra is real and inherent. For rGO, there is a similar structure in the 284.5 to 286.5 eV range as indicated by dashed lines in Fig. 5.2, but the problem does not affect the determination of the band gap because both d^2TFY/dE^2 and d^2TEY/dE^2 have minima at 283.3 eV. This leads to a band gap of about 0.3 eV. However, the determination of the band gap for GO is not so simple, as it is not obvious, at this point, which minima of the three available one should use. The three possible band gaps, based upon the three candidate minima at 284.6 eV, 285.2 eV, and 285.6 eV, are labeled

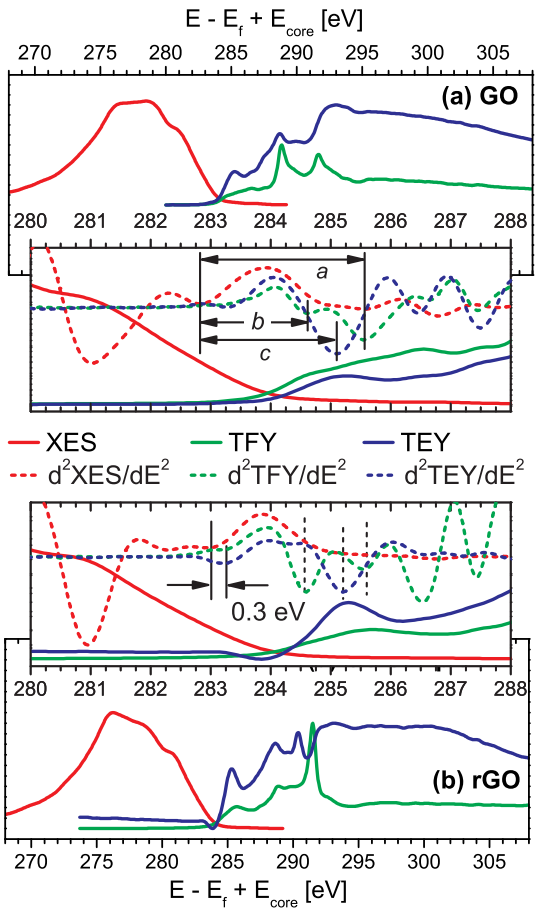

Figure 5.2: Experimental determination of the band gap of GO and rGO. In each panel, an inset is provides a magnified look at the states near the Fermi level. Within these insets, the second derivatives for each of the TEY, TFY, and XES spectra are shown. The three horizontal arrows in the inset of panel (a) indicate the three possible band gaps. They are labeled *a*, *b*, and *c* in order of increasing gap size. Note that the relative scaling of the TEY, TFY, and XES spectra is different in the insets as compared to the main panel; this was done purely for aesthetic purposes.

with arrows in panel (a) in Fig. 5.2.

Note that Fig. 5.2 shows many spectral differences between the spectra of GO and rGO, particularly in the range between 287 eV and 290 eV. This energy range is home to the spectral signatures of oxidizing functional groups [32, 33, 44, 115]. The 287-290 eV energy range holds key information about the chemical character of the sample in question, but it is not relevant to a study of the band gap of graphene oxide. Therefore, we do not discuss it.

We thus present two fundamental questions: 1) Why do the TEY and TFY spectra have such different structure, as shown by their second derivatives? 2) Which local minimum does one use for the determination of the band gap of GO? Neither question can be answered until it is known what is causing the double-dip structure in the TFY of both samples. As we shall show later, the answers to both of these questions involves the AA-stacking mode, and in particular, how this configuration behaves when subjected to pressure within the bulk of a material.

Pristine Graphene

The first step to answer the two questions stated above is to determine whether the double-dip structure is due to functionalization, or if one can see this structure in pristine multilayered graphene. To test this possibility, eight samples of pristine graphene mounted on SiO_2 substrates were prepared: two each of graphene, bilayered graphene, multilayered graphene with four to six layers, and multilayered graphene with ten or more layers, hereafter referred to as Gr, 2Gr, 4Gr, and 10Gr. The first set taken as is, and the second was annealed at 900°; further details of the synthesis can be found in the Experimental section. Fig. 5.3 displays XANES spectra measured from the samples with different numbers of pristine graphene layers, as well as HOPG. The spectra of the multilayered graphene samples were recorded in both TEY and PFY modes; the fluorescence spectrum of HOPG was recorded in TFY mode. The reason for the difference in fluorescence measurement technique is explained in the Experimental section.

As one can clearly see, there are very few features in the 287-290 eV energy range in the graphene spectra, particularly for the annealed samples. This marks a sharp contrast with the GO samples, but the difference is expected. No spectral features within this energy range

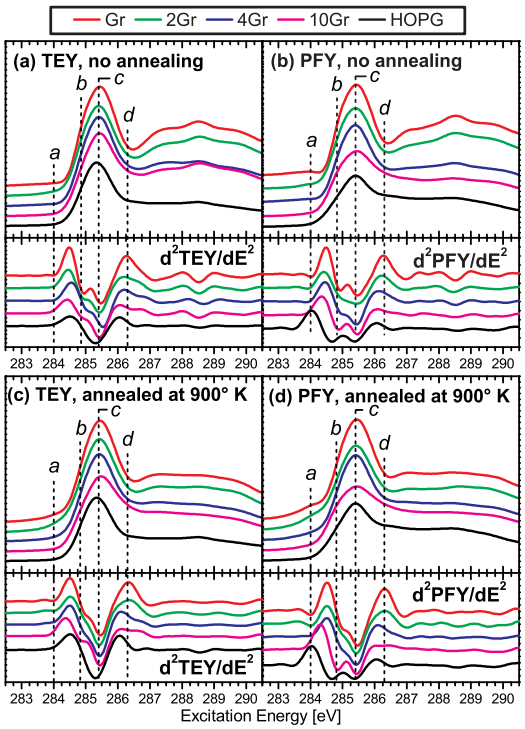

Figure 5.3: XANES spectra of Gr, 2Gr, 4Gr, and 10Gr, measured in TEY and PFY modes. XANES spectra of HOPG, measured in TEY and TFY mode, is included as a reference. The graphene spectra were all measured with an angle of incidence of 80° from the sample surface normal. The top two panels show the spectra measured from samples that were not annealed; the bottom two panels show spectra that were measured from samples annealed at 900° C. The second derivatives of each group of spectra are shown in the bottom halves of each of the panels.

indicate that the samples have not been functionalized. However, there is another marked difference between the graphene and GO samples worthy of mention: The PFY and TEY spectra of the graphene samples are very similar in shape. This similarity is to be expected because of the thinness of the graphene samples. The saturation effects that strongly distort the TFY spectra of GO in Fig. 5.2 are only problematic for samples that are thicker than the penetration depth of the incident radiation, which is on the order of 100-200 nm for soft X-rays.

Saturation effects do not distort the PFY spectra of the graphene samples and thus the PFY and TEY spectra are much similar in shape. However, the PFY and TEY spectra are not identical, particularly when comparing the PFY and TEY spectra of the multilayered graphene samples. One can immediately see that features *b* at 284.8 eV and *c* at 285.4 eV that constitute the double-dip structure in the d^2TFY/dE^2 of GO shown earlier are seen again. The double dip is seen most strongly in the d^2PFY/dE^2 spectra of both 10Gr samples. It would seem that, as one adds layers, the double-dip structure becomes more prominent in the d^2PFY/dE^2 spectra measured from the sample. This trend is strongly supported by the HOPG results. However, another pattern also emerges. In the second derivative, the minimum at 284.8 eV becomes prominent while the largely positive feature at 286.3 eV (feature *d*) is suppressed; the two spectral changes happen simultaneously, suggesting a common cause. As layers are added, spectral weight is being added at both 284.8 and 286.3 eV.

It is therefore clear that, as one adds more graphene layers, more states are added at both 284.8 eV and 286.3 eV. Indeed, HOPG also shows prominent dips in its d^2TFY/dE^2 at these energies, a sample that is highly non-functionalized and has been subjected to none of the chemicals involved in either the creation of GO, or the transfer of graphene. An as-yet unidentified layer-dependant phenomenon is affecting these changes. Note that other researchers have noticed features in the 284.6 eV to 286.3 eV energy range. Indeed, the d^2TEY/dE^2 and d^2PFY/dE^2 spectra of the non-annealed monolayer graphene sample also show a feature a dip 284.9 eV. In this case, the feature at 284.8 eV is likely caused by another effect, such as scattering from point defects, or doping from adsorbed gases or solvents. Whatever the source, it is mitigated by annealing, as this feature is sharply reduced

in the spectra from the annealed monolayer graphene. Spectral weight in the 284.6 eV to 284.9 eV energy range is thus likely a composite from many contributions, but it is the layer-dependent one that we seek here.

5.1.5 Discussion and Analysis

The double-dip structure has now been seen in GO, rGO, and multilayered pristine graphene if one stacks up 10 or more layers. Given that this structure occurs in pristine graphene and HOPG, it is not due to oxidation. This conclusion is supported by the fact that all prevalent functional groups identified on graphene oxide, namely carboxyl, hydroxyl, epoxide, and carbonyl, all have their characteristic resonances in the oxidation zone between 286 eV and 290 eV, and this energy region quite devoid of features. If the double-dip structure is not a chemical artifact, could it be due to structural differences, such as the interplanar stacking order?

We present a theoretical study of the effect of the stacking order on the electronic structure of multilayered graphene, in which we explicitly consider the AA- and AB-stacking configurations. Fig. 5.4 shows simulated XANES spectra of several structures, including graphene, AB- and AA-stacked bilayer graphene, and AB- and AA-stacked graphite; all simulations were performed using the WIEN2k code using the local density approximation (LDA) exchange-correlation functional. For all multilayered configurations, the interplanar spacing was optimized. The AB-stacked graphite had an optimized interplanar spacing that was very close to the experimental value of 3.348 Å, which is the reason why the LDA functional was chosen. The Perdew-Burke-Ernzerhof generalized gradient approximation (PBE-GGA) exchange-correlation functional did not report an optimal interplanar spacing. The AB-stacked bilayer graphene also had a calculated optimal interplanar spacing very close to the known value for bulk graphite. This result agrees with previous studies [116]. However, the AA-stacked configurations all preferred to be much further apart. Separate calculations at 3.348 Å, the interplanar spacing preferred by AB-stacked graphite, and at the optimized spacing of $\sim$ 3.6 Å were performed.

The simulations in Fig. 5.4 show three very important results. First, the π^* band of graphene, as well as that of bilayer and infinite layer stacked graphene (graphite) in the AB-

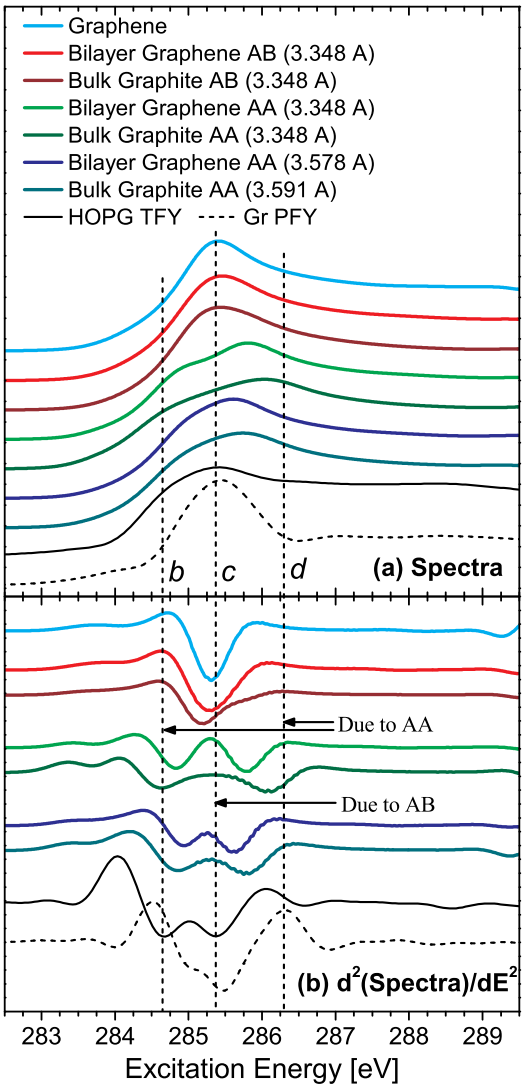

Figure 5.4: Simulated XANES spectra for graphene, bilayer graphene in AA- and AB-stacking configurations, and bulk graphite in AA- and AB-stacking. These simulations are compared to experimental spectra of graphene and HOPG. Vertical lines highlight important features in the experimental spectra; for consistency, the features are labeled identically to those in Fig. 5.3.

stacking configuration, has one major feature. In the second derivative, this feature produces one minimum in each case. Second, the π^* band of bilayer and infinite layer graphene (graphite) shows a much broader lineshape; in the second derivative, this yields two local minima. Third, the relative spacing of the AA-stacked minima (and hence the width of the π^* band) increases with an increasing number of layers and a decreasing interplanar spacing. If one were to increase the spacing to infinity, the double peak structure in the second derivatives of the bilayer graphene simulated XANES spectra would eventually coalesce into one feature, as one expects from graphene. In the AA-stacking bulk limit, when the interplanar distance equals that of AB-stacked graphite of 3.348 Å, the minima in the second derivative of the simulation line up quite well with the minima at 284.7 eV and 286.4 eV of the d^2TFY/dE^2 of highly-oriented pyrolytic graphite (HOPG), as shown in Fig. 5.4. Thus, it would seem that they layer-dependant effect that produces spectral weight at 284.7 eV and 286.4 eV is due to interactions between AA-stacked graphene sheets, whereas the minimum at 285.4 eV is due to AB-stacking.

The evidence is clear that that double dip structure seen in the d^2PFY/dE^2 of multilayered graphene, as well as that seen in the d^2TFY/dE^2 of multilayered GO, is due to spectral contributions from both AA-stacking and AB-stacking. We are now ready to answer the question concerning which local minimum one should use out of the three possibilities seen in the d^2TEY/dE^2 and d^2TFY/dE^2 spectra of GO shown in Fig. 5.2: One should use the lowest peak in the TFY due to AA-stacking (the band gap illustrated by arrow *b*). GO therefore shows a band gap of 1.8 eV. The AA-stacking order provides more states closer to the Fermi level, the implication of which is immediate: Controlling the stacking configuration of a multilayered GO samples gives the device fabricator another means by which the band gap may be tuned, in addition to simply controlling the oxidation level [46, 117]. In short, the stacking order adjusts the width of the π^* band, which therefore controls the band gap if the sample is oxidized and the near-Fermi states have been removed.

AA-stacked GO therefore has a smaller band gap than AB-stacked GO. However, there is more to the story. The theoretical results displayed in Fig. 5.4 clearly show that the π^* band widens as one brings sheets of graphene together in an AA-stacked order, which is markedly different behavior than that exhibited by the AB-stacked variety. The implications of this

are immediate. If the π^* band widens if AA-stacked sheets are brought closer to one another, then if one has a primarily AA-stacked sample of multilayered graphene oxide, then one may widen the π^* band and thus narrow the band gap simply by applying external pressure along the c-axis. In short, AA-stacking may provide a way to externally control the band gap of GO.

Indeed, the sensitivity of the width of the π^* feature in AA-stacked multilayered graphene to pressure along the c-axis explains why it is that the characteristic AA-stacked signal is not seen in TEY spectra. As mentioned earlier, multilayered graphene, if stacked in the AA configuration, is in its lowest energy state if the sheets are farther apart (about 3.58 Å) than if stacked in the AB configuration. The AA-stacked zones do not transition to AB-stacking; there is no phase change. Rather, the AA-stacked zones near the surface have the freedom to expand and have larger interplanar spacing. This larger spacing, in keeping with the results shown in Fig. 5.4, allows for a smaller π^* bandwidth, and thus the near-surface AA-stacked regions show XANES spectra that look much like the AB-stacked zones. TEY is highly surface sensitive, and would see only the expanded AA-stacked zones. Deeper within the sample, however, the freedom to expand would not exist for any AA-stacked region. Such AA-stacked zones would be forced by the neighboring AB-stacked majority to assume a nominal layer separation of 3.348 Å, which leads to the detectable widening of the π^* resonance feature in the bulk-sensitive TFY and PFY spectra of multilayered graphene, HOPG, and GO.

However, there is still an issue to address. The double-dip structure that is supposedly due to AA-stacking is an important component of the GO TFY spectra shown in Fig. 5.2 despite the fact that multilayered GO is known to have much greater interplanar spacing to accommodate the attached functional groups. The mechanism that allows for AA-stacking characteristics to appear in multilayered GO with large interplanar spacing is not understood at this time. However, it is clear that after reduction, minima at 284.6 eV and 286.5 eV become very prominent in the d^2TFY/dE^2 of rGO. Minima at these energies are due to AA-stacking, as we have already shown. It would appear that AA-stacking is perhaps the dominant stacking order in GO, much more so than in multilayered graphene. The reason for the preferred AA-stacking order, as well as the extent of the interplanar interaction in

highly oxidized GO samples, are subjects that require further study.

5.1.6 Conclusions

We have found that the stacking configuration of the sheets in multilayered graphene and GO has a strong effect on the shape of the main π^* feature. Fluorescence yield XANES measurements of graphene, multilayered graphene, and HOPG have shown that spectral weight at 286.3 eV and 284.7 eV arises as a function of number layers. Through DFT simulations, we have shown this spectral weight is due to AA-stacking. Although there are other effects that can introduce spectral weight at either 286.3 eV or 284.7 eV, AA-stacking can explain both simultaneously, given that they arise simultaneously. AA-stacking widens the normally sharp π^* feature in multilayered GO as well, bringing more states closer to the Fermi edge. If the near-Fermi states have been lost due to oxidation, then one can tune the band gap by controlling the stacking. The stacking configuration allows for an additional degree of freedom when designing an appropriate band gap.

The sensitivity of the band structure of AA-stacked multilayered graphene, and by extension the band structure of AA-stacked multilayered GO, to interplanar spacing leads to an exciting possibility: A band gap that is easily modulated by the external pressure along the c-axis. There has been much research into opening a band gap in graphene or bilayer graphene using stress, but most efforts have been to stress the sheet in a direction within the basal plane [118–121]. There also has been some theoretical work into introducing a band gap in bilayer graphene using stress parallel to the surface normal, but the strains necessary were in the range of 30% to 50% [122]. However, we suggest going in the opposite direction: Beginning with a wide band gap, apply stress to close it. According to our results, a device constructed of few-layered GO, if constructed in an AA-stacking regime, would have a tuneable band gap. This gap may close as the layers are compressed in the c-axis direction, because adding external compression on the AA-stacked GO would push more states towards the Fermi level, as the simulations in Fig. 5.4 suggest. Comparing the two AA-stacked graphite calculations (one with an interplanar spacing of 3.348 Å, the other with 3.578 Å), a strain of 7% could potentially close the band gap by 0.2 eV.

5.1.7 Acknowledgements

All samples were made by Sasha Stankovich (at the Department of Chemistry, Northwestern University, USA). We acknowledge support by the Natural Sciences and Engineering Research Council of Canada (NSERC), the Canada Research Chair program, Canada Foundation for Innovation (CFI), and the Russian Foundation for Basic Research (Projects 11-02-00022). We further acknowledge the financial support from the WCU program (R31-2008-000-10029-0) through the NRF funded by MEST of Korea. The Canadian Light Source is supported by NSERC, the National Research Council (NSC) Canada, the Canadian Institutes of Health Research(CIHR), the Province of Saskatchewan, Western Economic Diversification Canada, and the University of Saskatchewan. The Advanced Light Source is supported by the Director, Office of Science, Office of Basic Energy Sciences, of the U.S. Department of Energy under Contract No. DE-AC02-05CH11231. We also acknowledge Compute Canada for the use of their computational resources, because the electronic structures of graphene, as well as AA- and AB-stacked bilayer graphene, were simulated on the Grex cluster at the University of Manitoba. The Grex cluster is part of Westgrid.

Chapter 6

Pronounced, reversible, and in situ modification of the electronic structure of graphene oxide via cooling below 160 K

Cooling multilayered graphene oxide produces some remarkable results. If one cools GO below 160 K, in particular to 120 K, then the π^* feature at 285.2 eV that is present in all GO spectra is strongly suppressed. In most samples, it simply disappears altogether. Simultaneously, features at 287.4 eV and 288.5 eV show remarkable increase in spectral weight. This trend is completely reversible. If one warms the sample back to room temperature, the π^* feature returns while the functional group signatures again are reduced. This trend strongly suggests that the remaining π^* network is spontaneously oxidized at low temperatures, only to spontaneously reduce again at higher temperatures.

Multilayered GO, particularly GO made by the modified Hummers method, typically contains a lot of water. The source of this water is under debate, partly because the amount present is difficult to quantify. A significant amount of any intercalated water will be leftover from the sample preparation process, but there have been reports that water can spontaneously generate within a GO sample due to the reactions of epoxides with adsorbed hydrogen, hydroxyls with hydrogen, and hydroxyls with other hydroxyls.

Water is an excellent candidate as a non-covalent functionalizing species due to its very strong hydrogen bonds. The strength of its interaction with the GO lattice is strongly enhanced at low temperatures because, when one cools the sample far enough, the water can form an amorphous solid water (ASW) phase that enhances the effect. The ASW also seems to interact with the carbon sites that have not been directly oxidized. To test if water

can induce the observed effects, we performed DFT simulations of water interacting with graphene and lightly oxidized GO. Although the results are not perfect, the best simulations do indeed reduce the π^* spectral weight significantly, then add that weight to the functional group resonances.

Graphene is a fascinating material in its own right, but it is not well-suited for all applications. Chemically altering graphene *via* attaching various types of functional groups allows one to tailor the electronic properties of graphene, but typically at the cost of ruining the physical structure of the carbon lattice. Non-covalent functionalization of graphene allows for many exciting possibilities, because it changes the electronic structure without permanently changing the physical structure.

A note concerning the structure of the paper: It was written for a Letters-format journal published by Wiley, which means that it does not have clearly delineated sections other than an Acknowledgments section at the end of the paper.

The following list delineates the contributions of each author to the complete paper.

A. Hunt:

- Measured the GOp O Kα and C Kα XES data, as well as all C 1s XANES spectra
- Made all figures, and wrote most of the text of the manuscript
- Derived the TICS ratio analysis methodology

D. Dikin:

- His group made all of the samples
- Contributed writing suggestions and editing

E. McDermott:

- Measured the C Kα and O Kα RXES on iGOp and rGOp
- Helped with TICS ratio analysis
- Contributed to editing the manuscript

E. Kurmaev:

- Responsible for original motivation of the project and procurement of samples
- Wrote the original introduction

A. Moewes:

- Ph.D. supervisor of A. Hunt
- Integral to the writing of the first manuscript
- Aided in the interpretation of the spectra

6.1 Manuscript

Pronounced, reversible, and in situ modification of the electronic structure of graphene oxide via cooling below 160 K

Adrian Hunt,[1*] Dmitriy A. Dikin,[2], Eamon G. McDermott,[1] Ernst Z. Kurmaev,[3] and Alex Moewes[1]

[1]Department of Physics and Engineering Physics, University of Saskatchewan, 116 Science Pl, Saskatoon, Saskatchewan, Canada S7N 5E2
[2]Department of Mechanical Engineering, Northwestern University, 2145 Sheridan Road, Evanston, Illinois, USA 60208-3111
[3]X-ray Emission Spectroscopy Lab, Institute of Metal Physics, RAS Ural Div., 18 Kovalevskoi Str., 620990 Yekaterinburg, Russia

*Corresponding author. Email: adrian.hunt@usask.ca (A. Hunt)

6.1.1 Abstract

We have measured C s X-ray absorption near-edge spectra when the sample is below 160 K, and we have observed a pronounced change to the carbon density of states. Through comparison of the experimental spectra to theoretical DFT calculations, we have concluded that these changes are due to strong non-covalent functionalization of the residual π-conjugated graphene-like carbon sites by amorphous solid water. This change is completely reversible. Direct, covalent functionalization of graphene produces a carbon basal plane that is quite damaged, and our results show that it is possible to avoid this fate.

6.1.2 Main Body of the Paper

Graphene is a stable two-dimensional crystal, made of carbons atoms arranged in a hexagonal structure [1]. To say that research on graphene has been panoptic and effulgent would perhaps yet be understating the matter, however it is not hard to understand the interest this material commands. Pristine graphene is a zero band gap semiconductor, and the charge carriers near the Fermi level are massless Dirac fermions, which give graphene unprecedented electronic properties [123]. Graphene, and its derivatives such as graphene oxide, have been

implemented in a wide-ranging number of electronic and optoelectronic applications [124–126]. Graphene also has superior mechanical properties, and as such has also been effectively used in composite materials [95, 127]. Although graphene possesses many amazing qualities, however, it does not have a band gap, which means that pristine graphene is inappropriate in many applications that require a true semiconductor. Significant oxidation of graphene does open a semiconducting band gap, but unfortunately destroys the π-conjugated network that grants graphene its unique characteristics, even after chemical reduction to remove some of the functional groups [44]. Thus, one must either repair the damage to the carbon basal plane [18], or modify the electronic structure of graphene without damaging it, such as by non-covalent functionalization [45].

Repairing the damaged carbon basal plane is often done at elevated temperatures, but it is clear from the literature that temperature and graphene oxide (GO) have a complex relationship. When heated, the presence of water has been shown to catalyze the decomposition of graphene into CO_2 [37,128]. When multilayered GO is stored oxide at room temperature, the interplanar water content increases over time as epoxide and hydroxyl groups both react with chemisorbed hydrogen [38]. The low temperature range, namely below 0 °C, has also shown some interesting phenomena. Su *et al.* have found that the Young's modulus of graphene oxide paper varies with temperature with a peculiar hysteresis curve below 25 °C [129]. Huang *et al.* found that the conductivity of multilayered graphene oxide was strongly dependant on temperature. Their samples transitioned between semiconducting and insulating behavior at several different temperatures [12], a phenomenon which they attributed to water. Below 10 °C, the sample was an insulator. Hauptmann *et al.*, however, showed no such change in the conduction behavior of their samples. Over the range that Hauptmann *et al.* considered, the change in conductivity as a function of temperature did not deviate from that of a material that obeys a variable range hopping model of conduction [130]. Although it is clear that GO does undergo some change at low temperatures, an understanding of what occurs is not consistent in the literature; there is only scant information available, and the few studies that have been published paint a contradictory picture of what actually occurs when GO is cooled.

We seek here to explain why the electronic structure of GO changes at low tempera-

Table 6.1: Details concerning the preparation of the four GO samples.

Sample	Method of Manufacture
GOa	GO paper from water filtration
GOb	GO paper intercalated with hexylamine and dried
GOc	GO-water suspension; water was substituted with DMSO and filtered
GOd	GO-water suspension; water was substituted with DMSO and heated in solution, subsequently filtered

tures. To this end, we have performed X-ray absorption near edge spectroscopy (XANES) experiments upon four multilayered GO samples, each synthesized differently, and analyzed the results using density functional theory (DFT). The four samples are labeled GOa, GOb, GOc, and GOd, and important points of information concerning the preparation of these four samples is detailed in Table 6.1. The preparation methodology used to make our samples of multilayered graphene oxide paper is detailed elsewhere [67, 68]. We chose these samples because each has a different interlayer chemistry, although all were derived from the same GO base material, made via the modified Hummers method and subsequent water filtration.

We have probed four samples of graphene oxide paper (GO) using C 1s and O 1s XANES. The C 1s and O 1s XANES spectra represent the core hole-perturbed unoccupied partial density of states (pDOS) near to the C and O sites, respectively. All XANES spectra were measured at the Spherical Grating Monochromator (SGM) beamline at the Canadian Light Source [105]. The GO X-ray absorption near-edge spectra (XANES) were measured in total fluorescence yield (TFY) mode. For normalization, the O 1s and C 1s spectra were treated differently. For the O 1s spectra, the measured spectra were normalized to a signal generated simultaneously in a highly-transparent gold mesh upstream of the sample; this gold mesh current is necessary and sufficient to quantify the incident flux. For the C 1s spectra, however, carbon contamination on all upstream optical components precludes the use of this elegant system. Instead, all carbon spectra were normalized to the current generated in a photodiode placed in the incident beam, which allows one to asynchronously, but accurately, measure

the flux incident upon the sample [114].

The samples were first cooled to 120 K under ultra high vacuum (UHV) conditions, and the O 1s and C 1s XANES spectra were measured on all samples. The samples were then warmed in 40 K increments to 160 K, 200 K, and finally 240 K, with spectra recorded at each step. To mitigate radiation damage effects, all spectra were measured in fast scanning mode. This mode collects data constantly while rapidly moving through the energy range of the scan. Each XANES spectrum shown in Fig. 6.1 was measured in only 20 seconds. Additionally, each spectrum was measured while irradiating a new spot on the sample in question. Once the samples had returned to room temperature, still within UHV, the samples were cooled to 240 K, and back down to 120 K in 40 K steps. On the cooling cycle, we measured only the C 1s spectra as we were primarily interested in the hysteresis of the C partial density of states (pDOS). The results of the experiment are shown in Fig. 6.1.

There are two observations that are immediately clear from the C 1s data in Fig. 6.1: 1) The unoccupied C pDOS changes significantly, and 2) there is a clear hysteresis effect with temperature. Concerning the hysteresis, the samples all seem to retain high temperature (HT) characteristics until reaching some threshold transition temperature between 160 K and 120 K. Upon warming, the electronic structure of the samples retain much low temperature (LT) character until they have been fully warmed. Between the two extremes, a metastable state seems to exist where characteristics of both HT and LT states are present, although the dominant member of the mix depends which temperature extreme has been most recently experienced by the sample.

Concerning the electronic structure of the samples, there are two significant changes in the C unoccupied pDOS as one cools the sample. First, there is significant suppression of the residual π^* resonance at 285.2 eV (feature b in Fig. 6.1), with a concomitant enhancement of the main functional group resonances around 288.4 eV (feature c). This is true for all samples. GOd, however, uniquely possesses feature d. At 291.5 eV, this is the σ^* resonance of sp2 bonded carbon, which means that the HT state of GOd sees a stronger sp2 network than the other samples. This is fitting considering that GOd was the only sample to be heated after treatment (see Table 6.1). The fact that the cooling effect suppresses both residual π^* and σ^* states is significant, as it would seem that it targets the residual sp2

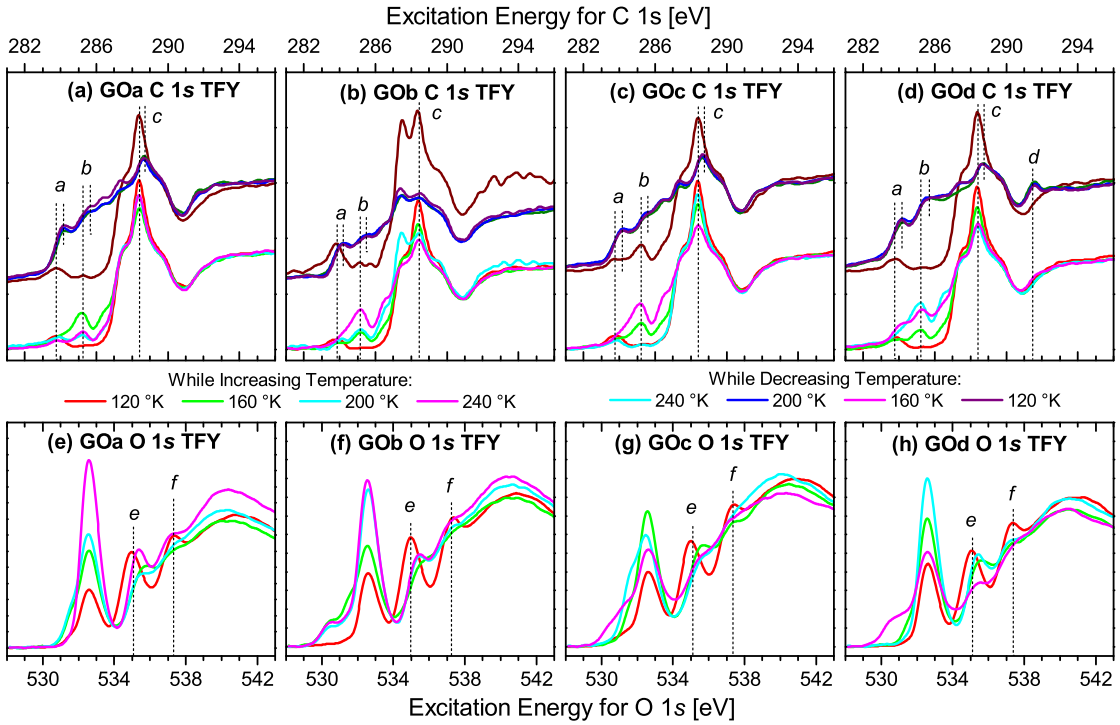

Figure 6.1: C 1*s* and O 1*s* XANES spectra of four samples of GO, measured at various temperatures. The top row of spectra are the C 1*s* spectra, while the bottom row holds the O 1*s* spectra. All black-colored spectra were measured after first cooling the samples to 120 K, then warming sequentially to 240 K. All grey-colored spectra were measured by cooling the samples from room temperature to 120 K. Only C 1*s* spectra were measured on the cooling cycle.

bonded carbon. There is also a general shift in energy for the π^* and functional group spectral features. With the exception of GOb, all of the easily-resolvable resonances are redshifted by 0.3 to 0.4 eV at LT as compared to their HT counterparts. There are two exceptions to this rule. Feature c in GOb does not shift, even as a and b do. However, it is also clear that the functional group chemistry of this sample is significantly different given the feature at 287.5 that is not present to any great degree in the other samples. Given that GOb is the only sample intercalated with hexylamine, it would seem that the initial cooling cycle permanently changed how hexylamine interacts with the host GO. The nature of this interaction is unknown.

The suppression of the π^* and σ^* states with a simultaneous enhancement of functional group states, particularly at 288.4 eV, suggests that residual carbon sp2 network is being functionalized. The question is: by what? The first clue to understanding this phenomenon may be seen in the O $1s$ spectra for the samples. Although there are some minor differences between the spectra from the four samples, one trend holds true: In all cases, feature e at 535.1 eV, and feature f at 537.3 eV, are very prominent at 120 K and fade as one approaches room temperature. The speed of the decay of these features as a function of temperature depends upon the sample, but it occurs for all. Features e and f at LT are distinctive, and they match similarly sharp features seen in the O $1s$ XANES spectra of amorphous solid water (ASW) [131, 132]. Theoretical simulations of water also show strong features at the appropriate energies, but only when broken hydrogen bonds (specifically with dangling hydrogens) are present [133].

Thus, previous work on ASW shows many spectroscopic similarities to the O $1s$ data in Fig. 6.1. Other research into the interaction between water and organic systems has shown that, in the presence of organic materials with a mosaic of hydrophobic and hydrophilic zones, like GO, water can form exotic structures [134]. In particular, the glass transition of water is below 160 K, which is the temperature range in which we see the dramatic change in electronic structure [135]. These reports apply here because GO synthesized with the modified Hummers method has significant amounts of intercalated water that is residue from the initial synthesis process. Given that the electronic structure change seems to impact the residual sp2 domains the strongest, we have attempted to simulate the change in electronic structure

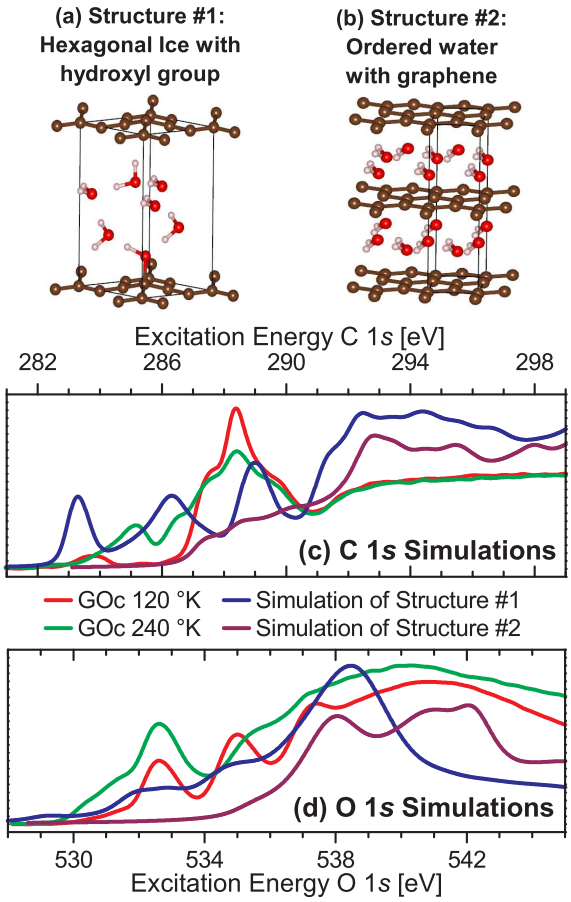

Figure 6.2: Comparison of DFT simulations with experimental C 1*s* and O 1*s* XANES spectra from GOd. Panels (a) and (b) show the structures that provide the most accurate simulated spectra. Panel (c) displays the comparison of the calculated C 1*s* XANES to the experimental XANES; panel (d) does likewise, but for the O 1*s* edge.

in GO at low temperatures by introducing ice between layers of graphene, as well as lightly oxidized graphene. The electronic structure simulations were performed using WIEN2k, a full-potential *ab initio* DFT code that uses linearly augmented plane wave (LAPW) formalism to describe the non-core states [136]. The structures that provided the results that most accurately represented the spectra are: 1) Hexagonal ice with a hydroxyl group (HI), and 2) ordered water with graphene (OW). The structures, and the corresponding electronic structure simulations, are presented in Fig. 6.2. The structures, in CIF format, are available in the Supporting Information.

Our criterion for evaluating the success of a simulation was straight forward: Given that it is the residual π-conjugated states that are most affected as one cools the samples, does the candidate structure modify the graphene and/or lightly oxidized graphene unoccupied pDOS in such a way as to explain the changes in spectral shape? We do not intend for our simulations to fully reproduce the GO spectra. Note that GO is a patchwork quilt of lightly oxidized zones interspersed among zones of dense functionalization [44], so the lightly oxidized states can be treated somewhat independently. With this in mind, the purpose of the simulations is only to try to reproduce the trend in the spectra as a function of temperature as the graphene-like states are altered, i.e. a much increased weighting around 288.4 eV with a simultaneously reduced π^* feature around 285.4 eV. This goal does not require a simulation of the heavily oxidized graphene states that seem to be affected less strongly by LT conditions. The changed states in the lightly oxidized graphene system will therefore stack with the unaffected, heavily oxidized parts of the graphene basal plane.

With this criterion in mind, both simulations reproduce the changes in the C $1s$ spectra reasonably well, although the HI structure is overzealous around 286 eV. The HI structure, however, does not reproduce the O $1s$ structure well at all. The OW structure provides a reasonable boost to the states around 288.4 eV, and has no spectral weight near 285.4 eV, which is a necessary state for success. It also reproduces a couple of the features in the O $1s$ spectra. In general, the OW structure provides the kind of change to the π-conjugated states that we need, and thus seems the clear winner, with the following caveat: The structure does not survive structure optimization. Upon optimization, the structure changes in such a way as to restore the (relatively) unperturbed graphene pDOS. It is almost a given that WIEN2k does not capture the dynamics of this system very well. Water systems are notoriously difficult to properly simulate [135], and thus much more work needs to be done.

The differences between the two simulations are significant in terms of the changes to the graphene DOS that each one ultimately represents. The HI structure strongly modifies the graphene electronic structure via non-covalent functionalization; the π-conjugated states are altered because of interaction between the water molecules and the graphene states. The hydroxyl group provides an 'anchor' of sorts to root the ordered water in place. The OW structure, on the other hand, produces the displayed C unoccupied pDOS through an en-

tirely different process. The shape of the C unoccupied pDOS remains relatively unchanged, however the Fermi level and the C $1s$ core level shift in energy; the Fermi level blueshifts in energy, whereas the $1s$ core level deepens. The blueshifting of the C $1s$ spectrum is thus the net result of these two phenomena, given that the energy axis on a given C $1s$ spectrum represents the difference between the unoccupied states and the core level from where the promoted electron originates. Regardless of which model is ultimately correct, they both see a significant drop in the density of π^* states - a necessary condition if the sample is to become less conductive, as observed by Huang *et al.* [12].

In summary, we have found that, upon cooling four differently prepared samples of GO to 120 K, a pronounced change in the C and O unoccupied pDOS occurs. This low temperature state has no remaining π-conjugated states, unlike the high temperature state of GO. Between 120 K and room temperature, the two states seemingly can coexist. Similarities between our O $1s$ XANES spectra and spectra of ASW suggest that water intercalated between the GO sheets underwent a phase change, a conclusion that is corroborated by the fact that the change in the O $1s$ spectra occurs around the glass transition temperature for water. DFT simulations of water intercalated between oxidized and pristine graphene suggests that intercalated ordered water can dramatically change the C unoccupied pDOS. This change is entirely reversible, albeit with a significant hysteresis curve that results from the aforementioned metastability of the HT and LT states in the temperature region between room temperature and 120 K.

The phase change between amorphous solid water and liquid water thus induces a dramatic change, via covalent functionalization, in the nominally lightly oxidized graphene sites in GO. The obvious benefit is that one can induce a pronounced, yet reversible, change in the electronic structure of graphene, under *in situ* conditions, without needing to damage the physical structure of graphene *via* the usual covalent functionalization techniques. In short, one can have either a conductor or a semiconductor, merely by changing the temperature. Working at such low temperatures is not desirable in a working device, however, polar solvents other than water are available. With sufficient research, perhaps it will be possible to find an appropriate combination of solvent and degree of functionalization such that one may use glass transitions to promote reversible, significant, and *in situ* band structure changes in

GO to suit the situation at hand at a temperature more easily achievable than 120 K.

6.1.3 Acknowledgements

All samples were synthesized by Sasha Stankovich while at the Department of Chemistry, Northwestern University, USA. We acknowledge support by the Natural Sciences and Engineering Research Council of Canada (NSERC), the Canada Research Chair program, Canada Foundation for Innovation (CFI), and the Russian Foundation for Basic Research (Projects 11-02-00022). The Canadian Light Source is supported by NSERC, the National Research Council (NRC) Canada, the Canadian Institutes of Health Research (CIHR), the Province of Saskatchewan, Western Economic Diversification Canada, and the University of Saskatchewan. We also acknowledge Compute Canada for the use of their computational resources, because the electronic structures of the reported structures, as well as many other failed candidates, were simulated on the Grex cluster at the University of Manitoba. The Grex cluster is part of Westgrid.

Chapter 7

A Reevaluation of the Role of Functional Groups in Modifying the Electronic Structure of Graphene Oxide

The Lerf-Klinowksi model for graphene oxide holds that the carbon basal plane is oxidized chiefly with epoxide, hydroxyl, and carboxyl functional groups, with contributions from ketone and carbonyl groups at defect sites and along the edges of the plane. Other experimental techniques that are sensitive to the physical structure, such as Fourier transform infrared (FTIR) spectroscopy and ^{13}C nuclear magnetic resonance (^{13}C NMR) spectroscopy, have verified this model. However, exactly how these functional groups change the density of states is still open to debate.

Accurately simulated the electronic structure of GO for the purposes of simulated the DOS has proven to be quite challenging for the GO research community. Using WIEN2k, we have simulated the electronic structure of GO using a linear combination of simulated X-ray XANES spectra from four different candidate structures:

1. Graphene
2. An epoxide structure with a C:O ratio of 2:1
3. An epoxide structure with a C:O ratio of 4:1
4. A hybrid epoxide/hydroxyl structure with a C:O ratio of 8:3

The fourth item, the epoxide/hydroxyl structure, began as a 4x4x1 supercell of graphene with 16 non-equivalent hydroxyls within it. Upon allowing force minimization, however, 4 of the hydroxyls (two above the plane, two below) had taken hydrogens from neighboring

hydroxyls (which then became epoxide groups), then floated away from the graphene plane to become interplanar free water molecules. The simulation was performed using only force minimization techniques. It was not a molecular dynamics simulation, so the kinetics of the problem were not computed. We do not know at this time whether this particular path for the evolution of graphene oxide can spontaneously happen at room temperature.

Upon adding the four theoretical spectra together and comparing the result to a XANES spectrum of GO, it was clear that the simulations had reproduced the DOS well. The exception is the zone around 288 eV, which is reproduced relatively poorly. Given that three of the four simulation involved epoxide, hydroxyls, or both, the validity of the Lerf-Klinowski model is assured. However, the source of the low-energy features in a typical GO spectrum is not at all what was expected. The presence of the epoxide and hydroxyl functional groups do indeed generate features at all the right energies, but for all features lower in energy than 288.5 eV, the primary sources of the spectral weight is not the carbon atoms bonded directly to the functional groups in question. The low-energy XANES features are, in fact, due to non-functionalized carbon sites that are near to, but not bonded directly with, the epoxide and/or hydroxyl groups.

The zone around 288 eV was not reproduced well in our simulations, for two reasons. First, we did not include carboxyl groups, which are difficult to model given the fact that they are chiefly bonded to the edges of the graphene plane; these particular functional groups are believed to have a strong resonance at 288.5 eV.

Second, we did not include any adsorbed molecules, like water. From our work shown in the manuscript *Pronounced, reversible, and in situ modification of the electronic structure of graphene oxide via cooling below 160 K*, we strongly suspect that water has a role to play in this energy region. Thus, we believe that physiosorbed atmospheric gases, such as O_2 or water, may add a not insignificant amount of spectral weight in this region, but we have not yet shown this conclusively *via* DFT simulations. Measurements of the same sample of HOPG at different times and at different beamlines have shown that features at 288.5 eV and 287.4 eV show up only at the SGM beamline. This beamline has the highest chamber pressure and lowest incident beam intensity (in [ph/s/m^2]) of all three beamlines at which we have measured C 1s XANES on HOPG (SGM, BL8, and REIXS). Thus, more

physiosorbed atmospheric gases would remain trapped in HOPG than with the other two beamlines, because the higher pressure and decreased local heat loading from the diffuse incident beam would not boil the gases out as quickly.

The Lerf-Klinowski model is correct, but it tells the GO researcher only what is affecting the electronic structure of GO, but not how it being affected, nor what to expect if the type and/or distribution of functional groups were altered. This work makes it clear that there is more work to be done to understand the fundamentals of graphene oxide.

A note concerning the structure of the paper: It was written for a Letters-format journal, which means that it does not have clearly delineated sections other than an Experimental section and an Acknowledgments section at the end of the paper.

The following list delineates the contributions of each author to the complete paper.

A. Hunt:

- Measured the GO C $1s$ and O $1s$ XANES data
- Made all figures, and wrote most of the text of the manuscript
- Performed all simulations

D. Dikin:

- His group made all of the samples
- Contributed writing suggestions and editing

E. Kurmaev:

- Responsible for original motivation of the project and procurement of samples
- Contributed writing suggestions and editing

A. Moewes:

- Ph.D. supervisor of A. Hunt
- Integral to the writing of the first manuscript
- Aided in the interpretation of the spectra

7.1 Manuscript

A Reevaluation of the Role of Functional Groups in Modifying the Electronic Structure of Graphene Oxide

A. Hunt,[1*] D. A. Dikin,[2] E. Z. Kurmaev,[3] and A. Moewes[1]

[1]Department of Physics and Engineering Physics, University of Saskatchewan, 116 Science Pl, Saskatoon, Saskatchewan, Canada S7N 5E2
[2]Department of Mechanical Engineering, Northwestern University, 2145 Sheridan Road, Evanston, Illinois, USA 60208-3111
[3]X-ray Emission Spectroscopy Lab, Institute of Metal Physics, RAS Ural Div., 18 Kovalevskoi Str., 620990 Yekaterinburg, Russia

*Corresponding author. Email: adrian.hunt@usask.ca (A. Hunt)

7.1.1 Abstract

If one wishes to engineer the electronic structure of graphene via functionalization, then one must first understand how said electronic structure changes upon chemical treatment. Up until now, the main method by which one would characterize the alterations was to compare the X-ray photoemission or X-ray absorption spectrum of functionalized graphene, in this case graphene oxide, to model spectra and find the common resonances. We show that a much more accurate method by which one may understand the electronic structure of graphene oxide is the use of appropriate density functional theory calculations in conjunction with X-ray absorption near edge spectroscopy measurements. Our results show that, in the case of graphene oxide, all states between 286 eV and 288 eV are from non-functionalized carbon sites, not from C-O-C or C-OH bonds as previously reported. We also show that physiosorbed atmospheric gases can add non-trival spectral weight at 287.5 and 288.5 eV.

7.1.2 Main Body of the Paper

Graphene is the first stable two-dimensional (2D) crystal ever found, a feat for which its discovers received the Nobel Prize in 2010 [1]. This fascinating material has carbon atoms arranged in a hexagonal lattice, and it is of great interest because because of its exceptional

electrical and mechanical properties. The physical structure of graphene forces the bands near the Fermi level into a Dirac cone with its vertex at the Fermi level, a peculiar state that gives rise to massless charge carriers near the Fermi level [123]. Graphene is a zero band gap semiconductor with unprecedented carrier mobility, and thus has been suggested for use in many different electronic and technological applications [6, 124, 126]. Graphene is, not surprisingly, highly transparent, and one very active avenue of research is developing graphene for use in optoelectronic and photovoltaic applications [125, 137].

Although the properties of graphene are exciting, graphene is not perfectly suited for all situations. If one wishes to use graphene for electronic device applications, a band gap must be introduced [20]. Using graphene for a transparent conducting electrode in organic solar cells requires that the energy levels of graphene align more favorably with those of the molecules in the active layer of the device to improve overall performance [45]. Many different ways to engineer the band structure of graphene have been proposed and successfully demonstrated [18,89,101]. However, the oxidization of graphene to make graphene oxide (GO), although one of the first methods tried, still promises to be first among the methods of graphene manufacture that will provide the highest yields for industrial-level manufacturing. If graphene-based products are indeed going to start from some form of GO, then understanding how the electronic structure of GO changes with chemical treatment from starting stock to final product is therefore an extremely important, and multifaceted, question.

To understand how the electronic structure of GO changes, one must first find an experimental method with which one may probe said electronic structure. A powerful technique for probing the electronic structure is X-ray absorption near-edge spectroscopy (XANES), given that it is site- and element-selective. This allows the experimentalist to individually probe the different non-equivalent sites within graphene oxide. With great success, XANES has been used to study how chemical modification leads to electronic structure modulation and physical structure evolution [32–34, 44, 47–49, 138]. However, having a powerful and appropriate experimental technique is not enough; one must also have a model framework within which one may analyze the experimental results and characterize the system under scrutiny.

Up until this point, features in XANES spectra of GO have usually been assigned by correlating the feature positions to binding energy values extracted from X-ray photoemis-

sion (XPS) spectra of simpler systems containing similar functional groups. XANES spectra of simpler model systems, like phthalic acid, can be used rather than XPS [56]. However, the database of XANES spectra to which one may compare a GO XANES spectrum is significantly smaller, which makes the task more challenging. The fundamental problem with the model system approach is that one must assume that each functional group remains an isolated unit, and thus retains its spectral identity. In extended, bulk systems like GO, particularly if it is multilayered, this assumption seems specious. Ideally, one would use an *ab initio* theoretical framework, such as density functional theory (DFT), to model the electronic structure. However, the electronic structure of graphene oxide is notoriously difficult to model because it is a highly chaotic, non-stoichiometric system, and thus a successful simulation of the electronic structure of GO, and subsequent comparison to experimental XANES measurements, has not previously been available.

Using density functional theory (DFT), we have simulated the electronic structure of four model structures for the purposes of performing a weighted sum to reproduce an experimental measurement. The simulations were computed using WIEN2k, a full-potential muffin tin (DFT) code that uses a linearized augmented plane wave (LAPW) basis set [136]. The structures simulated are graphene and three different forms of GO, named sGO1, sGO2, and sGO3. A simulation of pristine graphene was included to model those parts of GO that are very lightly functionalized. sGO1 is a simple structure consisting of only epoxide groups with a C:O ratio of 2:1; in this structure, all carbon atoms are functionalized. sGO2 is another epoxide-only structure with a C:O ratio of 4:1. Both structures were allowed to relax via internal force minimization. The final structure, sGO3, will be the subject of further research on its own. Beginning as a 4x4 supercell of graphene bonded with hydroxyls in a C:O 2:1 ratio, the structure was allowed to completely relax *via* force minimization. The unit cell began with 16 hydroxyl groups, but four absconded with hydrogen atoms from neighboring hydroxyl groups to form free-floating water molecules. The four deprotonated hydroxyl groups became epoxide groups. This spontaneous process of water formation from hydroxyl reaction has previously been theorized, and has been seen again here [139]. This theoretical evolution of the chemical structure is very interesting, however it is the electronic structure of the final product, rather that the dynamics of the reaction process, that is the

focus of this report.

We have calculated the C 1s XANES spectrum that each structure provides and added them to form a composite lineshape, to which we have compared an experimental XANES measurement of a sample of GO in Figure 7.1(a). The XANES measurement was performed at the SGM beamline at the Canadian Light Source (CLS) [105]; a brief explanation is supplied in the Experimental section at the end. The sample was positioned such that its normal made a 30° with respect to the propagation vector of the incident beam. The details of the preparation of the sample are published elsewhere [67]. The component simulated lineshapes are also included in Figure 7.1(a) to show how each contributed to the summation. The different components were weighted as follows: Graphene 30%, sGO1 25%, sGO2 25%, and sGO3%. With this mix, the overall theoretical C:O ratio is about 3.8.

As one can see, the agreement between theory and experiment in Figure 7.1 is good, in the sense that almost all of the main experimental features, highlighted and labeled as a through f, appear in the composite spectrum. Even the relative peak intensities are reasonably well-reproduced. The one problem is feature e, at 288.6 eV; this will be discussed later. As explained previously, the only functional groups included are epoxides and hydroxyls, which are the main groups in the Lerf-Klinowski model of graphene oxide [26]. The difficulty of the simulation notwithstanding, it therefore is not overly surprising that a theoretical model that includes epoxides and hydroxyls does indeed reproduce the electronic structure of graphene oxide. However, a closer look at the results of the simulations does show something unexpected: The non-equivalent C sites that give rise to the spectral features commonly seen in GO C 1s XANES spectra, particularly below 288 eV, are not the C sites bonded to functional groups. The sites that give a GO spectrum its characteristic appearance are, in fact, the interstitial C sites that exist between the functional groups.

Panels (b), (c), and (d) in Figure 7.1 show each calculation broken down into the individual spectra that arise from each non-equivalent (NEQ) C site in the unit cell in question. The NEQ spectra are arranged into three distinct categories: 1) Those spectra arising from carbon atoms bonded to epoxides, 2) those from carbon atoms bonded to hydroxyls, and 3) those from carbon atoms bonded to no functional group. In each panel is an image of one unit cell for that simulation; the carbon atoms are color-coded so that the color of the atom in

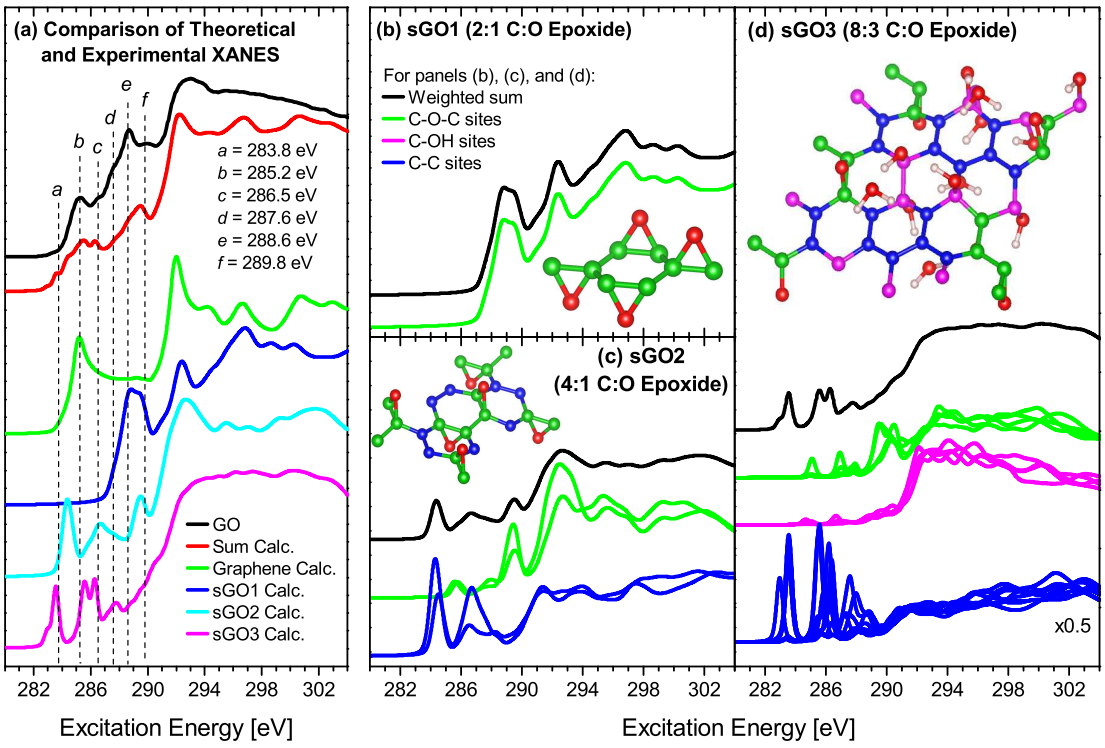

Figure 7.1: CComparison of experimental XANES spectra of GO to theoretical XANES. Displayed in panel (a) is a comparison of experimental XANES to the sum of four theoretical spectra: graphene, sGO1, sGO2, and sGO3. Panels (b), (c), and (d) show the sGO1, sGO2, and sGO3 simulated spectra, respectively. In each of these three latter panels, the spectrum of interest is broken down into a maximum of three components, and each component is given a different color. The spectral components due to those NEQ carbon sites bonded to epoxide groups (C-O-C) are colored green, those components due to hydroxyl groups (C-OH) are colored magenta, and those components due to non-functionalized carbon sites (C-C) are colored blue. The oxygen atoms are red. Each type of NEQ carbon site in the images of each unit cell is given the same color as its corresponding spectral component. The oxygen atoms are red, and the hydrogen atoms are pink.

the unit cell matches the color of the corresponding calculated spectrum. So, for example, carbon atoms colored blue are not bonded to any functional group, therefore the spectra from non-functionalized NEQ C sites are also blue. As one can quickly see, all of the spectral features below 288 eV are due to non-functionalized C sites.

These results directly contradict conventional thinking on how one should label features in GO C 1s XANES spectra. According to our calculations, the states near the main π^* resonance at 285.4 eV, which are vital to the electronic and optical performance of GO, are nearly entirely due to the non-functionalized C sites. It is clear that, even if not directly bonded to the functional groups in question, they are still strongly affected by the presence of the functional groups. It is not clear how the local unoccupied states at the non-functionalized sites are being modulated, but the effect is pronounced. It is this last point that provides the bridge between our results and those that have come before: Although the feature at 286.5 eV is not due to resonantly exciting a core electron into a C-OH bond, it is nevertheless the presence of that hydroxyl group that makes that transition possible.

What then about the resonance at 288.6 eV, where the discrepancy between theory and experiment is the strongest? The source of this particular feature has engendered the strongest controversy of any peak that one may find in a C 1s XANES spectrum measured from GO. This debate is encapsulated in the discussion between Pacilé *et al.*, who assigned this feature to interlayer states [30], and Jeong *et al.*, who ascribed it the influence of carboxyl functional groups bonded to the edge of the graphene flakes [34, 46]. We submit that the feature at 288.6 eV may be due to the presence of carboxyl. Our simulations did not include carboxyl groups, so we have no basis to either support or refute this interpretation. However, as we show in Figure 7.2, C 1s XANES spectra of highly oriented pyrolytic graphite can exhibit spectral weight at 288.5 eV and 287.5 eV - but not consistently.

Consider the C 1s XANES of highly oriented pyrolytic graphite (HOPG), measured in TEY mode, that are shown in Figure 7.2. This Figure compares spectra of HOPG. The variables that change between spectra are: The beamline at which the spectra were measured, the date of measurement, the angle of the sample surface normal with respect to the incident radiation propagation vector, and the preparation technique (freshly cleaved or not cleaved at all). Strong features occur at 287.5 and 288.5 eV in only two spectra, and the only common

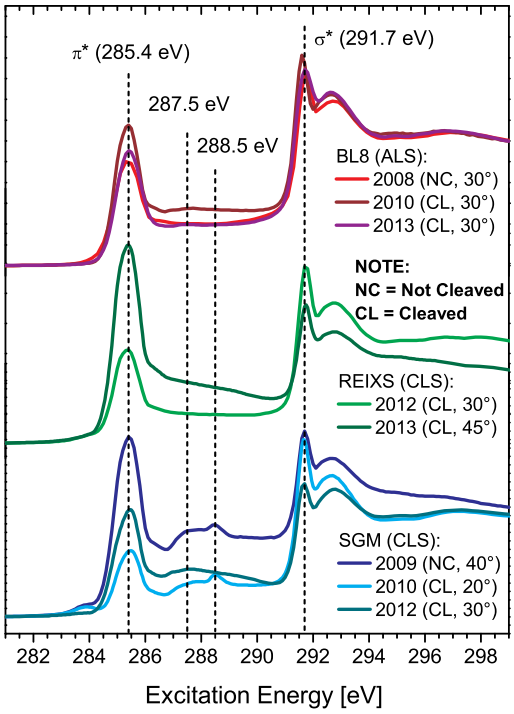

Figure 7.2: HOPG TEY spectra that were measured at different times, different beamlines, and different angles. The beamlines are denoted as follows: BL8 (ALS) refers to Beamline 8.0.1 at the Advanced Light Source; REIXS (CLS) refers to Resonant Elastic and Inelastic X-ray Scattering beamline at the Canadian Light Source; SGM (CLS) refers to the Spherical Grating Monochromator beamline at the Canadian Light Source. As noted in the Figure, CL is short for Cleaved, and NC is short for Not Cleaved.

variable is that both were measured at the SGM beamline. However, these features are not an artifact of the beamline apparatus; another spectrum, measured at another time, shows much reduced spectral weight. Given that the presence of the feature is not common to all spectra, despite the reproducibility of the HOPG C 1s XANES spectrum in all other respects, we submit that this feature is not due to interlayer states, nor any other state that arises from pure graphite. If a feature at 288.5 eV was indicative of interlayer states, then its should be universally reproducible.

As further evidence that the features at 287.5 eF and 288.5 eV are not due to the instrumentation at the SGM beamline, note that these features have been seen before in graphite.

Brandes *et al.* did a detailed STXM study of well-ordered natural graphite, and they saw features with similar shape at identical energies [140]. However, they did not see the features in every spectrum. Using the high spatial resolution that STXM can provide, they were able to correlate the existence of these states to damaged sections of the graphite structure. Well-ordered, relatively undamaged sections of their sample showed no additional spectral weight at either 287.5 eV or 288.5 eV whatsoever.

We propose that the spectral features at 287.5 eV and 288.5 eV, witnessed here and by Brandes *et al.*, are due to physiosorbed atmospheric gases, possibly O_2 or water. Justification for this explanation begins with the fact that the spectral signatures in question happen in damaged graphite. Damage to the graphite crystal structure will proliferate places to which atmospheric gas molecules may physiosorb [141]. The reason why spectra of HOPG measured at the SGM contain the very same spectral signatures, but not the spectra measured at BL8 or REIXS, is that the SGM beamline does not promote the desorption of the trapped gasses nearly as strongly as either BL8 or REIXS for two reasons. First, the SGM has the smallest flux density of all three beamlines. y as strongly as either BL8 or REIXS for two reasons. First, the SGM has the smallest flux density of all three beamlines. The flux densities are roughly 2x10^8 photons $\cdot$ s^{-1} $\cdot$ μm^{-2}, 6x10^9 photons $\cdot$ s^{-1} $\cdot$ μm^{-2}, and 4x10^7 photons $\cdot$ s^{-1} $\cdot$ μm^{-2} for BL8, REIXS, and SGM, respectively. This is important because higher flux density means greater energy density deposited in the sample, and therefore, greater heat loading that will promote offgassing. Second, REIXS and BL8 each have better vacuum in the measurement chamber than SGM. The pressure at the RIXS endstation on the REIXS beamline is maintained at a low 10^{-8} Torr, and the SXF endstation on the BL8 beamline is usually a low 10^{-9} Torr, whereas the XANES endstation on the SGM beamline is often in a middle-range 10^{-7} Torr. Lesser heat loading and higher pressure, when taken together, means that HOPG will hold more of its physiosobed gasses when studied at SGM.

The XANES experiment on HOPG show that the features around 288 eV, which have caused such debate, are due in no small part to physiosorbed atmospheric gasses. Given that our GO samples already contain a lot of water, the likely culprit is water. As others have suggested, the 288.5 eV feature likely has spectral weight that is due to resonantly exciting carboxyl functional groups. However, the interlayer states interpretation does not fit, given

that its presence is not reproducible when measuring the same sample of HOPG.

In conclusion, we have analyzed the C 1s XANES spectrum of a typical sample of GO using DFT, and we have found that the changes to the electronic structure of graphene brought about by oxidization through functionalization is more complicated than has been envisioned to date. Our DFT simulations included epoxide and hydroxyl groups, and they reproduce all of the spectral features in a typical GO spectrum, except for the strong resonance at 288.6 eV. This confirms the legitimacy of the Lerf-Klinowski model, and lends credence to the accuracy of our results. However, all spectral features below 288 eV are mostly due to C sites that are not directly bonded to a functional group, yet have their local states modified by the nearby functional groups. On the other hand, states arround 288 eV are likely strongly influenced by physiosorbed atmospheric gases, notably water. This significantly impacts the efforts of any researcher attempting to accurately engineering the electronic structure of graphene, because the use of spectra from simpler systems to analyze the results of an experiment does not appropriately account for the complexity of the interactions between non-equivalent sites in GO.

7.1.3 Experimental

GO and HOPG C 1s XANES spectra were measured at the Spherical Grating Monochromator (SGM) beamline at the Canadian Light Source [105]. The exit slit to the monochromator was set to 25 μm, which gives the incident light an energy resolution better than 0.1 eV. The spectra were measured in both total electron yield mode and total fluorescence mode. C 1s XANES spectra of HOPG were also performed at Beamline 8.0.1 at the Advanced Light Source at the Lawrence Berkeley National Laboratory [59]. Although this beamline is principally used for X-ray emission (XES) measurements, one can perform XANES experiments as well. The monochromator entrance and exit slits were set to 20 μm and 30 μm, respectively, to give a total experimental resolution was 0.1 eV FWHM. For both the SGM and BL801 beamlines, the light is linearly polarized, and the electric field component of the incoming light lies in the plane of incidence. REIXS is similar in configuration to the previous two beamlines, except that the insertion device at REIXS is an elliptically polarizable undulator. For the purposes of our experiment, the undulator was set to provide linearly polarized light

with the electric field vector in the plane of incidence. The resolving power of the REIXS monochromator is also superior, providing resolution at the C 1s edge of approximately 0.05 eV with the exit slit set to 25 μm.

In all cases but one, the HOPG spectra were normalized by a current generated in a highly transparent gold mesh that is upstream of the sample, thus providing a measure of the incident photon flux. The one exception is the 2012 spectrum measured at the SGM. Instead, this spectrum was instead normalized to the current generated in a photodiode [114]. This photodiode current spectrum was not taken simultaneously with the sample spectrum, but rather directly afterwards. This was necessary because the gold mesh on the SGM had become highly contaminated by carbon at that time, and was no longer able to provide an accurate measure of the incident photon flux.

7.1.4 Acknowledgement

We acknowledge support by the Natural Sciences and Engineering Research Council of Canada (NSERC), the Canada Research Chair program and the Russian Foundation for Basic Research (Projects 11-02-00022). The Canadian Light Source is supported by NSERC, the National Research Council (NSC) Canada, the Canadian Institutes of Health Research (CIHR), the Province of Saskatchewan, Western Economic Diversification Canada, and the University of Saskatchewan. The Advanced Light Source is supported by the Director, Office of Science, Office of Basic Energy Sciences, of the U.S. Department of Energy under Contract No. DE-AC02-05CH11231.

Chapter 8

The Influence of Sample Preparation Methodology on the Band Gap of Graphene Oxide Paper

This manuscript is a follow-up to the paper entitled, *Modulation of the Band Gap of Graphene Oxide: The Role of AA-Stacking*, which is now published in *Carbon*. The first paper outlined the methodology and justification for determining which feature is at the bottom of the CB. In this manuscript, we use that process to determine the band gaps for six differently-prepared samples of GO, all based upon the modified Hummers method.

There are many different ways to prepare GO in order to illicit a certain modification to the DOS, and in particular, the band gap. Intercalating the sample with hexylamine increased the band gap to 2.1 eV, in comparison to the regular GO band gap of 1.8 eV, by moving the occupied states deeper in energy. Replacing water with DMSO, however, shrunk the band gap by 0.2 eV to 1.6 eV. However, the two processes that changed the band gap by the greatest amount were heating and chemical reduction.

Heating also had the side effect of generating a resonance at 290.3 eV in two of the three samples that were heated. This feature at 290.3 eV is due to carbonate, or more accurately, carbonic acid that is created when GO reacts with water to form CO_2. The one sample that did not have the feature at 290.3 eV is also the sample that had water replaced by DMSO. Without water to make carbonic acid, the CO_2 simply diffused out of the sample much faster. In any case, the heating lead to a smaller band gap for two reasons: 1) The heat drove a reaction in which water reacts with GO to removing functional groups, and 2) heating GO helps to repair carbon basal plane damage by smoothing wrinkles and rebuilding

broken π-conjugated bond networks.

The electrical conductivity was measured using a DC four-probe arrangement. Comparing the measured conductivities with the band gaps, it would seem that the exhibited decrease in band gap for the heated samples did not lead to an expected increase in conductivity, if the population of the CB is driven by Fermi-Dirac statistics. In other words, either the band gaps are actually bigger than what we determined, or the conductivity is being restricted by something else. The latter option is the most likely, because conduction in GO is not a simple matter. The damage to the carbon basal plane due to functionalization, even after reduction, leads to charge trapping and broken π-conjugated networks. This means that conduction is likely better modeled by a hopping mechanism than by a band mechanism.

The following list delineates the contributions of each author to the complete paper.

A. Hunt:

- Measured all C Kα XES and C 1s XANES spectra
- Analyzed the spectra to find the band gap
- Made all figures, and wrote most of the text of the manuscript

D. Dikin:

- His group made all of the samples
- His group performed the DC four-probe measurements

E. Kurmaev:

- Responsible for original motivation of the project and procurement of samples
- Aided in the literature search

A. Moewes:

- Ph.D. supervisor of A. Hunt
- Integral to the writing of the first manuscript

8.1 Manuscript

The Influence of Sample Preparation Methodology on the Band Gap of Graphene Oxide Paper

A. Hunt,[1*] D. A. Dikin,[2] E. Z. Kurmaev,[3] and A. Moewes[1]

[1]Department of Physics and Engineering Physics, University of Saskatchewan, 116 Science Pl, Saskatoon, Saskatchewan, Canada S7N 5E2
[2]Department of Mechanical Engineering, Northwestern University, 2145 Sheridan Road, Evanston, Illinois, USA 60208-3111
[3]X-ray Emission Spectroscopy Lab, Institute of Metal Physics, RAS Ural Div., 18 Kovalevskoi Str., 620990 Yekaterinburg, Russia

*Corresponding author. Email: adrian.hunt@usask.ca (A. Hunt)

8.1.1 Abstract

The method with which one creates a sample of graphene oxide paper has a strong impact on its electronic structure. Using X-ray emission spectroscopy and X-ray absorption spectroscopy to indirectly measure the band gap, we have found that intercalation with hexylamine increases the band gap, while replacing water with DMSO decreases the band gap. Reduction with hexylamine sharply decreases the band gap as expected, but we have also found that heating the sample reduces the band gap to the same degree. This band gap reduction is due to defunctionalization of graphene oxide *via* reaction with water that produces CO_2. DC four-probe conductivity measurements show that the decrease in band gap width leads to a lower-than-expected increase in conductivity, likely because the heat-induced defunctionalization process destroys the graphene sheet and reduces overall carrier mobility.

8.1.2 Main Body of the Paper

Graphene is a stable two-dimensional crystal [1] that shows a distinct characteristic in its band structure: the bands near the Fermi level form a Dirac cone that results in massless charge carriers near the Fermi level that propagate through the crystal at the speed of

light [123]. The vertex of this cone sits at the Fermi level, which means graphene is a zero band gap semiconductor, and thus has been suggested for use in many different electronic and technological applications [6,124,126]. If one requires graphene to conduct charge carriers, it is perfectly suited for this task. However, the lack of band gap means that graphene cannot be used in devices designed to perform digital logic because a band gap is required to provide distinct 'on' and 'off' conduction states [20]. Oxidizing graphene to produce graphene oxide introduce this necessary band gap is an obvious choice, particularly because reducing and repairing graphene oxide (GO) to produce graphene still promises to be first among the methods of graphene manufacture that will provide the highest yields for industrial-level manufacturing. Thus, GO is not only a useful product in its own right, but is also the precursor for graphene. Understanding how the electronic structure of GO changes with chemical treatment is therefore an extremely important question.

We present here a study of the electronic structure of graphene oxide as a function of the chemical modification of graphene oxide. We probe the electronic properties of six differently-synthesized samples of graphene oxide using X-ray absorption near-edge fine structure (XANES), to probe the conduction band (CB), and non-resonant X-ray emission spectroscopy (XES), to probe the valence band (VB). These techniques boast site- and chemical-specificity that other techniques do not possess, allowing for a detailed study of the carbon states that populate the near-Fermi energy regime. In addition to detailed chemical information about the samples, these spectra indirectly provide the band gap because the band gap is the energy difference between the top of the VB (highest energy state in the XES spectrum) and the bottom of the CB (lowest energy state in the XANES spectrum). Others have accurately determined the band gaps of various materials using a combination of XANES and XES [108–110]. Our experimental band gaps are compared to DC four-probe conductivity measurements.

As mentioned previously, we experimented on six samples, each prepared slightly differently. The samples are called graphene oxide sample A, B, C, D, E, and F (shortened to GOa, GOb, GOc, GOd, GOe, GOf, respectively). All six samples were made from the same base material, then five were subjected to some additional treatment. The samples were further subdivided into three sets of two; in each set, two samples were made in exactly the same

Table 8.1: Details concerning the manufacture of the six graphene oxide samples. The six samples are split into three groups of two, with one sample functioning as the control sample for a second, identically-prepared sample that was subjected to an additional procedure.

Set	Sample	Method of Manufacture	Notes [eV]
Set 1	GOa	GO paper from water filtration	Control for all
	GOb	GO-water suspension, water was substituted with DMF, added hydrazine, heated and reduced in solution; finally, it was filtered.	
Set 2	GOc	GO paper intercalated with hexylamine and dried.	Control for GOf
	GOf	GO paper intercalated with hexylamine, dried, then annealed in air.	
Set 3	GOd	GO-water suspension; water was substituted with DMSO and filtered.	Control for GOe
	GOe	GO-water suspension; water was substituted with DMSO and heated in solution, after that filtered.	

manner, but one sample of the set was subjected to an additional procedure to which the other was not, thus making one sample a control used to study the effects of the additional procedure. The details are summarized in Table 8.1.

Figure 8.1 shows the results of our experiments, as well as our analysis of the spectra for the purpose of determining the band gap. In this figure, the non-resonant XES spectrum and the XANES spectrum is plotted on the same energy axis, each in a separate panel for each sample. The XES spectra were measured at Beamline 8.0.1 at the Advanced Light Source [59], while the XANES spectra were measured at the SGM beamline at the Canadian Light Source [105]; abbreviated details on the experimentation apparatuses are included in the Experimental section. The XANES spectra were measured in both total electron yield (TEY) and total fluorescence yield (TFY) modes. The TFY spectra that are displayed have been treated using the method of Eisebitt *et. al*, which takes into account, and partially counteracts, the effects of saturation that can severely distort the lineshape of TFY spectra [106, 107]. As an added benefit, in the weak near-Fermi energy range, this method suppresses the even weaker noise component, thus allowing for unambiguous determination

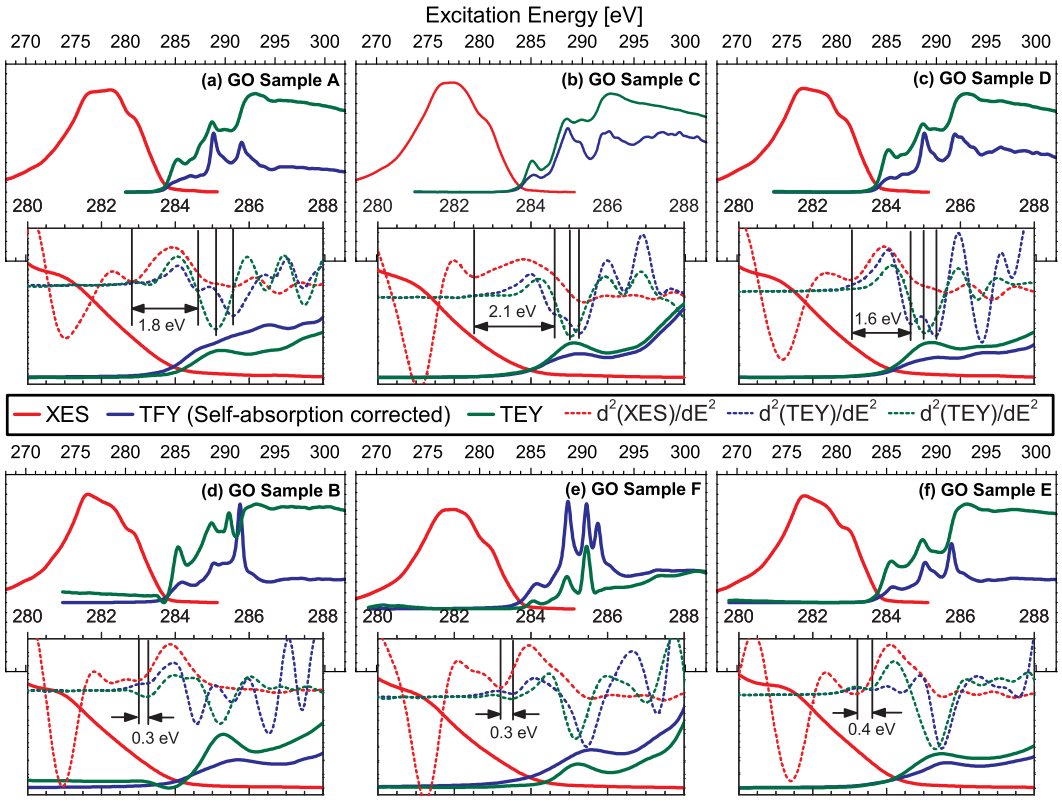

Figure 8.1: Experimental determination of the band gap of six samples of graphene oxide. Each panel is labeled with the sample in the top right corner, and the band gap in the bottom left corner. In each panel, an inset is provides a magnified look at the states near the Fermi level; it is here that the band gap is labeled.

of real features.

The shapes of the spectra from the six samples hold much information, which will be discussed later. Let us first discuss the band gaps of the samples. As with other spectroscopic methods for determining the band gap, the question of where the bands actually start is central to the accuracy of the analysis. The method chosen here to find the band edges the second derivative method, because weak sharp features, such as localized molecular orbitals and sharp band onsets, show much more prominently than broad features. This is true even if the broad feature has much greater spectral weight. This property helps to extract

details from the near-Fermi portions of the XES and XANES spectra. The centroids of peaks in a spectrum become local minima in the second derivative of that spectrum. Thus, the band gap is defined as the energy difference between the highest-energy local minimum in the second derivative of the XES spectrum (denoted d^2XES/dE^2) and the lowest-energy minimum in second derivative of the XANES spectrum (denoted either d^2TEY/dE^2 or d^2TFY/dE^2, as appropriate). The second derivative method has proven to be an accurate and highly reproducible way to determine experimental band gaps from X-ray spectra [41, 111–113]. Whether the gap is direct or indirect cannot be determined from this method without the aid of other analysis techniques.

The second derivatives of the XES, TFY, and TEY spectra of the six samples were computed for the purpose of determining the band gap, and all are displayed in the appropriate insets in Figure 8.1. As one can see in the insets, for no sample does its d^2TEY/dE^2 and d^2TFY/dE^2 agree as to the placement of local minima. Invariably, the d^2TFY/dE^2 has the lowest-energy feature, and in many cases, the d^2TFY/dE^2 has more local minima. This particular problem has been addressed in previous work, and the feature at roughly 284.6 eV that makes such a prominent minimum in the d^2TFY/dE^2 spectrum for each sample is due to AA-stacking interactions between GO sheets, whereas the feature that sits somewhere between 285.3 and 285.5 eV is due to AB-stacking [78] (also self citation here, once published). The latter is the preferred stacking arrangement in graphite. As we have established, the lowest-energy peak, due to AA-stacking interactions in GO, determines the upper boundary of the band gap.

Using this minimum, the three control samples (GOa, GOc, and GOd) show a band gap between 1.6 eV and 2.1 eV. These band gaps are typically smaller than those reported in the literature [142, 143] although there is some disagreement [144]. This is to be expected, however. Unlike with optical absorption techniques, the site-selectivity of XANES allows one to directly probe the defect states. The three samples that were subjected to some post-processing (GOb, GOe, and GOf) have significantly reduced band gaps, with values around 0.3 eV. Table 8.2 shows the measured conductivities and the measured band gaps of the six samples. The inverse correlation between the width of the gap and the conductivity of the sample shows that the chosen method of second derivative comparison XES and XANES

Table 8.2: Experimental conductivities and band gaps of the six samples of graphene oxide (GOa, GOb, GOc, GOd, GOe, and GOf), arranged by set. The conductivity measurements were performed using a DC 4-probe configuration.

Set	Sample	Conductivity [S/m]	Band Gap [eV]
Set 1	GOa	$< 10^{-3}$	1.8 ± 0.2
	GOb	265 ± 33	0.3 ± 0.2
Set 2	GOc	$< 10^{-3}$	2.1 ± 0.2
	GOf	52 ± 9	0.3 ± 0.2
Set 2	GOd	$< 10^{-3}$	1.6 ± 0.2
	GOe	184 ± 24	0.4 ± 0.2

produced reasonable results for the band gap.

Among GOa, GOc, and GOd, the variation in band gap comes strictly from the position of the local minimum in the XES spectrum; the unoccupied state that defines the top of the band gap remains fixed. In particular, the increase in the band gap in GOc could be interpreted as a result of the hexylamine molecules increasing the separation between GO nanosheets. Greater separation limits π-π overlap and hence decreases the effective conjugation length of the remaining π-conjugated network. The band gap closure for GOb, GOe, and GOf, however, is a result of movement of both the occupied and unoccupied states. In these three samples, the VB has states higher in energy, while the CB simultaneously shows states lower in energy, than GOa, GOc, or GOd. This result is consistent with an interpretation that holds that the closure of the band gap is due to restoration of the π-conjugated network, which is in turn due to lessened functionalization of the graphene sheets [142, 143]. In short, the near-Fermi π-symmetry occupied and unoccupied states are removed as the samples are functionalized, and restored as functionalization is lessened.

An analysis of the CB and VB shapes indicates that GOb, GOe, and GOf have smaller band gaps due to lessened functionalization. For GOb, the reason for this reduced functionalization is the application of hydrazine. However, the reason for the reduced state of GOe and GOf is less obvious. A clue to the reason for partial restoration of π-conjugation in GOf is found in the higher-energy CB states. Figure 8.2 displays the TEY spectra of GOb and GOf, as well as the other four samples, for the purpose of comparing their unoccupied states. For the most part, the XANES spectra from all six samples are largely what we have

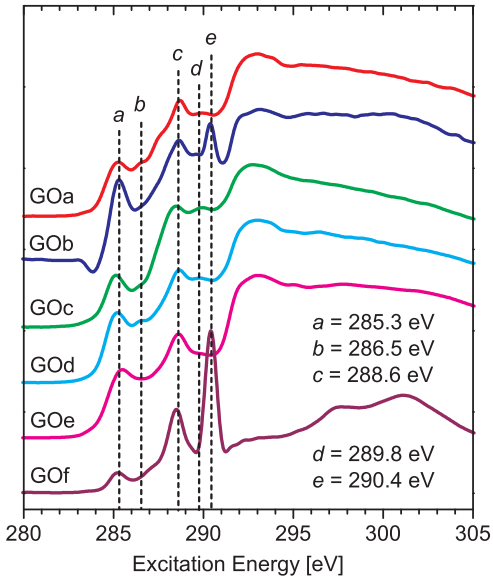

Figure 8.2: Comparison of the TEY spectra measured from GOa, GOb, GOc, GOd, GOe, and GOf. Five major spectral features are labeled *a*, *b*, *c*, *d*, and *e*; the energies of these features are listed in the figure.

come to expect from GO. Features *a*, *b*, *c* and *d* in Figure 8.2 have been seen often before, although the true meaning of these features is yet open to debate [30, 47, 49, 145]. However, the spectrum from GOf is quite distinct, because it has a very strong resonance, feature *e*, at roughly 290.4 eV. This peak is present only in the spectra of GOf and GOb.

This resonance at 290.4 eV is very likely due to carbonate [82], or more likely in this case, carbonic acid that arises from CO_2 interacting with water intercalated between the graphene oxide layers. It has been shown that, when GO is subjected to heat, water can react with some functional groups and release CO_2 [37]. This process results in a carbon basal plane that is less oxidized and thus has a smaller band gap, but is also more damaged, because the basal plane is the source of the carbon in the ejected CO_2. If this interpretation for the source of the carbonate peak is correct, then this feature signifies defunctionalization of graphene oxide, and thus should accompany a reduction in band gap. This is exactly what we observe. Only two samples were simultaneously processed in water and heated; both of these samples show the carbonate peak, and both have a small band gap.

Note that GOe was also heated, and also shows a small band gap. GOd, the other sample that was suspended in DMSO, had the smallest band gap of all three non-heated samples, so it may be that DMSO-containing GO is simply prone to having a smaller band gap for similar functionalization levels. However, GOe does not show the carbonate peak at 290.4 eV. There are two possible explanations for this. The first is that there is a DMSO/GO reaction mechanism that, upon heating, lessens functionalization like H_2O/GO, only it does not produce CO_2. There is no literature, to the best of our knowledge, that discusses such an interaction, so we can explore it no further at this time. The second explanation is that there is no carbonate peak simply because GOe has no water with which CO_2 may be dissolved. Whatever water that remained after it was replaced with DMSO would have been free to react with graphene oxide as the solution was heated, just like in the cases of GOb and GOf. However, there would not have been enough water to dissolve the resultant CO_2 and form carbonic acid, thus leaving behind no spectral trace.

In conclusion, we have explored how the electronic structure of multilayered GO changes as a function of sample preparation. The width of the band gap is widened by intercalating hexylamine into the structure, but it is narrowed if DMSO is used as a solvent instead of H_2O. The strongest band gap change, however, is due to heating, because heating the samples promotes defunctionalization of the carbon basal plane *via* reaction with water and subsequent release of CO_2, which narrows the gap but further damages the carbon basal plane. This is likely the reason why the conductivity did not improve as much as one would expect given the much smaller band gaps that appear after heating. Although the band gap may be smaller, structural defects in the basal plane hinder proper conduction.

8.1.3 Experimental

The GO XES spectra were performed at Beamline 8.0.1 at the Advanced Light Source at the Lawrence Berkeley National Laboratory using the soft X-ray fluorescence (SXF) endstation [59]. Emitted radiation was measured using a Rowland circle type spectrometer with a large spherical grating and a photon-counting area detector. The total experimental resolution was 0.3 eV FWHM. The fluorescence measurements were made using a depolarized configuration, which means that the vector E of the incidence beam lies at the scattering plane. The SXF

endstation is configured such that the path of the emitted photons and the incident beam are perpendicular.

High-resolution C 1s XANES spectra on the C K edge were measured at the Spherical Grating Monochromator (SGM) beamline at the Canadian Light Source [105]. The incident light had a resolution of 0.1 eV. The spectra were measured in both total electron yield and total fluorescence yield modes. Instead of normalizing to an upstream mesh current, however, the spectra were instead normalized to the current generated in a photodiode [114]. This photodiode current spectrum was not taken simultaneously with the sample spectrum, but rather directly afterwards. This technique allows one to directly measure the light intensity hitting the sample as a function of energy, which allows one to correct for the problem of a carbon-contaminated mesh introducing false features into carbon spectra.

8.1.4 Acknowledgement

We acknowledge support by the Natural Sciences and Engineering Research Council of Canada (NSERC), the Canada Research Chair program and the Russian Foundation for Basic Research (Projects 11-02-00022). The Canadian Light Source is supported by NSERC, the National Research Council (NSC) Canada, the Canadian Institutes of Health Research (CIHR), the Province of Saskatchewan, Western Economic Diversification Canada, and the University of Saskatchewan. The Advanced Light Source is supported by the Director, Office of Science, Office of Basic Energy Sciences, of the U.S. Department of Energy under Contract No. DE-AC02-05CH11231.

References

[1] K. Novoselov, A. Geim, S. Morozov, D. Jiang, Y. Zhang, S. Dubonos, I. Grigorieva, A. Firsov, *Science* **2004**, *306*, 666–669.

[2] P. Wallace, *Phys. Rev.* **1947**, *71*, 622–634.

[3] T. Land, T. Michely, R. Behm, J. Hemminger, G. Cosma, *Surf. Sci.* **1992**, *264*, 261–270.

[4] K. Novoselov, A. Geim, S. Morozov, D. Jiang, M. Katsnelson, I. Grigorieva, S. Dubonos, A. Firsov, *Nature* **2005**, *438*, 197–200.

[5] X. Du, I. Skachko, A. Barker, E. Y. Andrei, *Nat. Nanotech.* **2008**, *3*, 491–495.

[6] A. K. Geim, K. S. Novoselov, *Nat. Mater.* **2007**, *6*, 183–191.

[7] H. Wang, Q. Hao, X. Yang, L. Lu, X. Wang, *Electrochem. Commun.* **2009**, *11*, 1158–1161.

[8] J. O. Sofo, A. S. Chaudhari, G. D. Barber, *Phys. Rev. B* **2007**, *75*, 153401.

[9] M. Z. S. Flores, P. A. S. Autreto, S. B. Legoas, D. S. Galvao, *Nanotech.* **2009**, *20*, 465704.

[10] S. H. Lee, D. H. Lee, W. J. Lee, S. O. Kim, *Adv. Funct. Mater.* **2011**, *21*, 1338–1354.

[11] D. Angmo, F. C. Krebs, *J. Appl. Polym. Sci.* **2013**, *129*, 1–14.

[12] X. Huang, Z. Zeng, Z. Fan, J. Liu, H. Zhang, *Adv. Mater.* **2012**, *24*, 5979–6004.

[13] A. Bostwick, F. Speck, T. Seyller, K. Horn, M. Polini, R. Asgari, A. H. MacDonald, E. Rotenberg, *Science* **2010**, *328*, 999–1002.

[14] T.-F. Yeh, J.-M. Syu, C. Cheng, T.-H. Chang, H. Teng, *Adv. Funct. Mater.* **2010**, *20*, 2255–2262.

[15] J. T. Robinson, F. K. Perkins, E. S. Snow, Z. Wei, P. E. Sheehan, *Nano Lett.* **2008**, *8*, 3137–3140.

[16] D. Li, M. B. Mueller, S. Gilje, R. B. Kaner, G. G. Wallace, *Nat. Nanotech.* **2008**, *3*, 101–105.

[17] S. Stankovich, D. A. Dikin, R. D. Piner, K. A. Kohlhaas, A. Kleinhammes, Y. Jia, Y. Wu, S. T. Nguyen, R. S. Ruoff, *Carbon* **2007**, *45*, 1558–1565.

[18] Y. Zhu, D. K. James, J. M. Tour, *Adv. Mater.* **2012**, *24*, 4924–4955.

[19] K.-H. Liao, A. Mittal, S. Bose, C. Leighton, K. A. Mkhoyan, C. W. Macosko, *ACS Nano* **2011**, *5*, 1253–1258.

[20] P. Avouris, Z. Chen, V. Perebeinos, *Nat. Nanotech.* **2007**, *2*, 605–615.

[21] D. W. Boukhvalov, M. I. Katsnelson, *J. Am. Chem. Soc.* **2008**, *130*, 10697–10701.

[22] J. T. Paci, T. Belytschko, G. C. Schatz, *J. Phys. Chem. C* **2007**, *111*, 18099–18111.

[23] Z. Xu, K. Xue, *Nanotech.* **2010**, *21*, 045704.

[24] J.-A. Yan, L. Xian, M. Y. Chou, *Phys. Rev. Lett.* **2009**, *103*, 086802.

[25] R. J. W. E. Lahaye, H. K. Jeong, C. Y. Park, Y. H. Lee, *Phys. Rev. B* **2009**, *79*, 125435.

[26] A. Lerf, H. He, M. Forster, J. Klinowski, *J. Phys. Chem. B* **1998**, *102*, 4477–4482.

[27] H. He, J. Klinowski, M. Forster, A. Lerf, *Chem. Phys. Lett.* **1998**, *287*, 53–56.

[28] J. Chattopadhyay, A. Mukherjee, C. E. Hamilton, J. Kang, S. Chakraborty, W. Guo, K. F. Kelly, A. R. Barron, W. E. Billups, *J. Am. Chem. Soc.* **2008**, *130*, 5414+.

[29] K. A. Mkhoyan, A. W. Contryman, J. Silcox, D. A. Stewart, G. Eda, C. Mattevi, S. Miller, M. Chhowalla, *Nano Lett.* **2009**, *9*, 1058–1063.

[30] D. Pacile, M. Papagno, A. F. Rodriguez, M. Grioni, L. Papagno, *Phys. Rev. Lett.* **2008**, *101*, 066806.

[31] M. Papagno, A. F. Rodriguez, C. O. Girit, J. C. Meyer, A. Zettl, D. Pacile, *Chem. Phys. Lett.* **2009**, *475*, 269–271.

[32] V. Lee, L. Whittaker, C. Jaye, K. M. Baroudi, D. A. Fischer, S. Banerjee, *Chem. Mater.* **2009**, *21*, 3905–3916.

[33] V. Lee, C. Park, C. Jaye, D. A. Fischer, Q. Yu, W. Wu, Z. Liu, S.-S. Pei, C. Smith, P. Lysaght, S. Banerjee, *J. Phys. Chem. Lett.* **2010**, *1*, 1247–1253.

[34] H. K. Jeong, H. J. Noh, J. Y. Kim, M. H. Jin, C. Y. Park, Y. H. Lee, *Europhys. Lett.* **2008**, *82*, 67004.

[35] L. Wang, Y. Y. Sun, K. Lee, D. West, Z. F. Chen, J. J. Zhao, S. B. Zhang, *Phys. Rev. B* **2010**, *82*, 161406.

[36] B. Huang, H. Xiang, Q. Xu, S.-H. Wei, *Physical Review Letters* **2013**, *110*, 085501.

[37] M. Acik, C. Mattevi, C. Gong, G. Lee, K. Cho, M. Chhowalla, Y. J. Chabal, *ACS Nano* **2010**, *4*, 5861–5868.

[38] S. Kim, S. Zhou, Y. Hu, M. Acik, Y. J. Chabal, C. Berger, W. de Heer, A. Bongiorno, E. Riedo, *Nat. Mater.* **2012**, *11*, 544–549.

[39] J. Li, K. Kudin, M. McAllister, R. Prud'homme, I. Aksay, R. Car, *Phys. Rev. Lett.* **2006**, *96*, 176101.

[40] D. B. Shinde, J. Debgupta, A. Kushwaha, M. Aslam, V. K. Pillai, *J. Am. Chem. Soc.* **2011**, *133*, 4168–4171.

[41] T. D. Boyko, E. Bailey, A. Moewes, P. F. McMillan, *Phys. Rev. B* **2010**, *81*, 155207.

[42] T. D. Boyko, A. Hunt, A. Zerr, A. Moewes, *Phys. Rev. Lett.* **2013**, *111*, 097402.

[43] S. Hüfner, *Photoelectron Spectroscopy: Principles and Applications*, of *Advanced Texts in Physics*, Springer, **2003**.

[44] A. Hunt, D. A. Dikin, E. Z. Kurmaev, T. D. Boyko, P. Bazylewski, G. S. Chang, A. Moewes, *Adv. Funct. Mater.* **2012**, *22*, 39503957.

[45] H. Y. Mao, Y. H. Lu, J. D. Lin, S. Zhong, A. T. S. Wee, W. Chen, *Prog. Surf. Sci.* **2013**, *88*, 132–159.

[46] H. K. Jeong, H. J. Noh, J. Y. Kim, L. Colakerol, P. A. Glans, M. H. Jin, K. E. Smith, Y. H. Lee, *Phys. Rev. Lett.* **2009**, *102*, 099701.

[47] A. Ganguly, S. Sharma, P. Papakonstantinou, J. Hamilton, *J. Phys. Chem. C* **2011**, *115*, 17009–17019.

[48] D. Zhan, Z. Ni, W. Chen, L. Sun, Z. Luo, L. Lai, T. Yu, A. T. S. Wee, Z. Shen, *Carbon* **2011**, *49*, 1362–1366.

[49] V. Lee, R. V. Dennis, B. J. Schultz, C. Jaye, D. A. Fischer, S. Banerjee, *J. Phys. Chem. C* **2012**, *116*, 20591–20599.

[50] C. Kittel, *Introduction to Solid StatePhysics*, Wiley, **1996**.

[51] A. C. Thompson, J. Kirz, D. T. Attwood, E. M. Gullikson, M. R. Howells, J. B. Kortright, Y. Liu, A. L. Robinson, J. H. Underwood, K.-J. Kim, I. Lindau, P. Pianetta, H. Winick, G. P. Williams, J. H. Scofield, *Center for X-ray Optics and Advanced Light Source X-ray Data Booklet 3rd ed.*, Center for X-ray Optics and Advanced Light Source, **2009**.

[52] P. Phillips, *Advanced solid state physics*, of *Frontiers in Physics Series*, Westview Press, **2003**.

[53] D. J. Griffiths, *Introduction to Electrodynamics (3rd Edition) 3rd ed.*, Benjamin Cummings, **1999**.

[54] F. de Groot, M. Arrio, P. Sainctavit, C. Cartier, C. Chen, *Solid State Commun.* **1994**, *92*, 991–995.

[55] J. MacNaughton, A. Moewes, E. Kurmaev, *J. Phys. Chem. B* **2005**, *109*, 7749–7757.

[56] I. Christl, R. Kretzschmar, *Environ. Sci. Technol.* **2007**, *41*, 1915–1920.

[57] J. A. Carlisle, E. L. Shirley, E. A. Hudson, L. J. Terminello, T. A. Calcott, J. J. Jia, D. L. Ederer, R. C. C. Perera, F. J. Himpsel, *Phys. Rev. Lett.* **1995**, *74*, 1234–1237.

[58] J. McLeod, *From personal correspondance* **2012**.

[59] J. J. Jia, T. A. Callcott, J. Yurkas, A. W. Ellis, F. J. Himpsel, M. G. Samant, J. Stohr, D. L. Ederer, J. A. Carlisle, E. A. Hudson, L. J. Terminello, D. K. Shuh, R. C. C. Perera, *Rev. Sci. Instrum.* **1995**, *66*, 1394–1397, 5th International Conference on Synchrotron Radiation Instrumentation, Stony Brook, NY, Jul 18-22, 1994.

[60] A. C. Thompson, D. Vaughan (Eds.), *X-ray Data Booklet 2nd ed.*, Lawrence Berkeley National Laboratory, University of California, **2001**.

[61] S. W. Tong, Y. Wang, Y. Zheng, M.-F. Ng, K. P. Loh, *Adv. Funct. Mater.* **2011**, *21*, 4430–4435.

[62] X. Wang, L. Zhi, K. Muellen, *Nano Lett.* **2008**, *8*, 323–327.

[63] J. Wu, H. A. Becerril, Z. Bao, Z. Liu, Y. Chen, P. Peumans, *App. Phys. Lett.* **2008**, *92*, 263302.

[64] Q. Liu, Z. Liu, X. Zhang, N. Zhang, L. Yang, S. Yin, Y. Chen, *App. Phys. Lett.* **2008**, *92*, 223303.

[65] Q. Liu, Z. Liu, X. Zhong, L. Yang, N. Zhang, G. Pan, S. Yin, Y. Chen, J. Wei, *Adv. Funct. Mater.* **2009**, *19*, 894–904.

[66] R. A. Nistor, D. M. Newns, G. J. Martyna, *ACS Nano* **2011**, *5*, 3096–3103.

[67] D. A. Dikin, S. Stankovich, E. J. Zimney, R. D. Piner, G. H. B. Dommett, G. Evmenenko, S. T. Nguyen, R. S. Ruoff, *Nature* **2007**, *448*, 457–460.

[68] S. Stankovich, D. A. Dikin, O. C. Compton, G. H. B. Dommett, R. S. Ruoff, S. T. Nguyen, *Chem. Mater.* **2010**, *22*, 4153–4157.

[69] W. Zhang, V. Carravetta, Z. Li, Y. Luo, J. Yang, *J. Chem. Phys.* **2009**, *131*, 244505.

[70] T. Sun, S. Fabris, *Nano Lett.* **2012**, *12*, 17–21.

[71] P. Ajayan, B. Yakobson, *Nature* **2006**, *441*, 818–819.

[72] P. Johari, V. B. Shenoy, *ACS Nano* **2011**, *5*, 7640–7647.

[73] W. Cai, R. D. Piner, F. J. Stadermann, S. Park, M. A. Shaibat, Y. Ishii, D. Yang, A. Velamakanni, S. J. An, M. Stoller, J. An, D. Chen, R. S. Ruoff, *Science* **2008**, *321*, 1815–1817.

[74] A. Bagri, C. Mattevi, M. Acik, Y. J. Chabal, M. Chhowalla, V. B. Shenoy, *Nat. Chem.* **2010**, *2*, 581–587.

[75] C. Gomez-Navarro, J. C. Meyer, R. S. Sundaram, A. Chuvilin, S. Kurasch, M. Burghard, K. Kern, U. Kaiser, *Nano Lett.* **2010**, *10*, 1144–1148.

[76] D. W. Lee, L. De Los Santos, V, J. W. Seo, L. L. Felix, A. Bustamante D, J. M. Cole, C. H. W. Barnes, *J. Phys. Chem. B* **2010**, *114*, 5723–5728.

[77] H.-K. Jeong, L. Colakerol, M. H. Jin, P.-A. Glans, K. E. Smith, Y. H. Lee, *Chem. Phys. Lett.* **2008**, *460*, 499–502.

[78] H.-K. Jeong, Y. P. Lee, R. J. W. E. Lahaye, M.-H. Park, K. H. An, I. J. Kim, C.-W. Yang, C. Y. Park, R. S. Ruoff, Y. H. Lee, *J. Am. Chem. Soc.* **2008**, *130*, 1362–1366.

[79] S. Biniak, G. Szymanski, J. Siedlewski, A. Swiatkowski, *Carbon* **1997**, *35*, 1799–1810.

[80] V. Datsyuk, M. Kalyva, K. Papagelis, J. Parthenios, D. Tasis, A. Siokou, I. Kallitsis, C. Galiotis, *Carbon* **2008**, *46*, 833–840.

[81] D. R. Dreyer, S. Park, C. W. Bielawski, R. S. Ruoff, *Chem. Soc. Rev.* **2010**, *39*, 228–240.

[82] C. Hontoria-Lucas, A. Lopez-Peinado, J. Lopez-Gonzalez, M. Rojas-Cervantes, R. Martin-Aranda, *Carbon* **1995**, *33*, 1585–1592.

[83] C. Mattevi, G. Eda, S. Agnoli, S. Miller, K. A. Mkhoyan, O. Celik, D. Mostrogiovanni, G. Granozzi, E. Garfunkel, M. Chhowalla, *Adv. Funct. Mater.* **2009**, *19*, 2577–2583.

[84] C.-Y. Su, Y. Xu, W. Zhang, J. Zhao, X. Tang, C.-H. Tsai, L.-J. Li, *Chem. Mater.* **2009**, *21*, 5674–5680.

[85] Z.-S. Wu, W. Ren, L. Gao, B. Liu, C. Jiang, H.-M. Cheng, *Carbon* **2009**, *47*, 493–499.

[86] T. Tokushima, Y. Horikawa, Y. Harada, O. Takahashi, A. Hiraya, S. Shin, *Phys. Chem. Chem. Phys.* **2009**, *11*, 1679–1682.

[87] T. Tokushima, Y. Harada, O. Takahashi, Y. Senba, H. Ohashi, L. G. M. Pettersson, A. Nilsson, S. Shin, *Chem. Phys. Lett.* **2008**, *460*, 387–400.

[88] T. Sun, S. Fabris, S. Baroni, *J. Phys. Chem. C* **2011**, *115*, 4730–4737.

[89] X. Li, W. Cai, J. An, S. Kim, J. Nah, D. Yang, R. Piner, A. Velamakanni, I. Jung, E. Tutuc, S. K. Banerjee, L. Colombo, R. S. Ruoff, *Science* **2009**, *324*, 1312–1314.

[90] K. Hermann, L. G. M. Pettersson, *Documentation for StoBe 2011, 3rd ed.*, **2011**.

[91] F. Schedin, A. K. Geim, S. V. Morozov, E. W. Hill, P. Blake, M. I. Katsnelson, K. S. Novoselov, *Nat. Mater.* **2007**, *6*, 652–655.

[92] L. Dai, D. W. Chang, J.-B. Baek, W. Lu, *Small* **2012**, *8*, 1130–1166.

[93] V. C. Tung, M. J. Allen, Y. Yang, R. B. Kaner, *Nat. Nanotech.* **2009**, *4*, 25–29.

[94] J. Liu, Z. Lin, T. Liu, Z. Yin, X. Zhou, S. Chen, L. Xie, F. Boey, H. Zhang, W. Huang, *Small* **2010**, *6*, 1536–1542.

[95] S. Stankovich, D. A. Dikin, G. H. B. Dommett, K. M. Kohlhaas, E. J. Zimney, E. A. Stach, R. D. Piner, S. T. Nguyen, R. S. Ruoff, *Nature* **2006**, *442*, 282–286.

[96] S. Myung, J. Park, H. Lee, K. S. Kim, S. Hong, *Adv. Mater.* **2010**, *22*, 2045+.

[97] H. He, X. Li, J. Wang, T. Qiu, Y. Fang, Q. Song, B. Luo, X. Zhang, L. Zhi, *Small* **2013**, *9*, 820–824.

[98] Z. Yin, S. Wu, X. Zhou, X. Huang, Q. Zhang, F. Boey, H. Zhang, *Small* **2010**, *6*, 307–312.

[99] X. Sun, Z. Liu, K. Welsher, J. T. Robinson, A. Goodwin, S. Zaric, H. Dai, *Nano Res.* **2008**, *1*, 203–212.

[100] X. Yang, X. Zhang, Y. Ma, Y. Huang, Y. Wang, Y. Chen, *J. Mater. Chem.* **2009**, *19*, 2710–2714.

[101] D. A. Siegel, S. Y. Zhou, F. El Gabaly, A. V. Fedorov, A. K. Schmid, A. Lanzara, *App. Phys. Lett.* **2008**, *93*, 243119.

[102] T. S. Sreeprasad, V. Berry, *Small* **2013**, *9*, 341–350.

[103] K. Momma, F. Izumi, *J. Appl. Crystallogr.* **2011**, *44*, 1272–1276.

[104] A. C. Ferrari, J. C. Meyer, V. Scardaci, C. Casiraghi, M. Lazzeri, F. Mauri, S. Piscanec, D. Jiang, K. S. Novoselov, S. Roth, A. K. Geim, *Phys. Rev. Lett.* **2006**, *97*, 187401.

[105] T. Regier, J. Krochak, T. Sham, Y. Hu, J. Thompson, R. Blyth, *Nucl. Instrum. Meth. A* **2007**, *582*, 93–95.

[106] S. Eisebitt, T. Boske, J. Rubensson, W. Eberhardt, *Phys. Rev. B* **1993**, *47*, 14103–14109.

[107] A. J. Achkar, T. Z. Regier, H. Wadati, Y. J. Kim, H. Zhang, D. G. Hawthorn, *Phys. Rev. B* **2011**, *83*, 081106.

[108] C. Dong, C. Persson, L. Vayssieres, A. Augustsson, T. Schmitt, M. Mattesini, R. Ahuja, C. Chang, J. Guo, *Phys. Rev. B* **2004**, *70*, 195325.

[109] C. McGuinness, C. Stagarescu, P. Ryan, J. Downes, D. Fu, K. Smith, R. Egdell, *Phys. Rev. B* **2003**, *68*, 165104.

[110] C. Pao, P. Babu, H. Tsai, J. Chiou, S. Ray, S. Yang, F. Chien, W. Pong, M. Tsai, C. Hsu, L. Chen, C. Chen, K. Chen, H. Lin, J. Lee, J. Guo, *App. Phys. Lett.* **2006**, *88*, 223113.

[111] E. Z. Kurmaev, R. G. Wilks, A. Moewes, L. D. Finkelstein, S. N. Shamin, J. Kunes, *Phys. Rev. B* **2008**, *77*, 165127.

[112] C. Braun, M. Seibald, S. L. Boerger, O. Oeckler, T. D. Boyko, A. Moewes, G. Miehe, A. Tuecks, W. Schnick, *Chem. Eur. J* **2010**, *16*, 9646–9657.

[113] T. D. Boyko, C. E. Zvoriste, I. Kinski, R. Riedel, S. Hering, H. Huppertz, A. Moewes, *Phys. Rev. B* **2011**, *84*, 085203.

[114] B. Watts, L. Thomsen, P. Dastoor, *J. Electron Spectrosc. Relat. Phenom.* **2006**, *151*, 105–120.

[115] D. Pacile, J. C. Meyer, A. F. Rodriguez, M. Papagno, C. Gomez-Navarro, R. S. Sundaram, M. Burghard, K. Kern, C. Carbone, U. Kaiser, *Carbon* **2011**, *49*, 966–972.

[116] S. B. Trickey, F. Muller-Plathe, G. H. F. Diercksen, J. C. Boettger, *Phys. Rev. B* **1992**, *45*, 4460–4468.

[117] I. Jung, D. A. Dikin, R. D. Piner, R. S. Ruoff, *Nano Lett.* **2008**, *8*, 4283–4287.

[118] O. Frank, M. Bousa, I. Riaz, R. Jalil, K. S. Novoselov, G. Tsoukleri, J. Parthenios, L. Kavan, K. Papagelis, C. Galiotis, *Nano Lett.* **2012**, *12*, 687–693.

[119] Z. H. Ni, T. Yu, Y. H. Lu, Y. Y. Wang, Y. P. Feng, Z. X. Shen, *ACS Nano* **2008**, *2*, 2301–2305.

[120] Z. H. Ni, H. M. Wang, Y. Ma, J. Kasim, Y. H. Wu, Z. X. Shen, *ACS Nano* **2008**, *2*, 1033–1039.

[121] Y. Li, X. Jiang, Z. Liu, Z. Liu, *Nano Res.* **2010**, *3*, 545–556.

[122] B. Verberck, B. Partoens, F. M. Peeters, B. Trauzettel, *Phys. Rev. B* **2012**, *85*, 125403.

[123] A. H. Castro Neto, F. Guinea, N. M. R. Peres, K. S. Novoselov, A. K. Geim, *Rev. Mod. Phys.* **2009**, *81*, 109–162.

[124] X. Huang, C. Zhi, P. Jiang, D. Golberg, Y. Bando, T. Tanaka, *Nanotech.* **2012**, *23*, 455705.

[125] H. Chang, H. Wu, *Adv. Funct. Mater.* **2013**, *23*, 1984–1997.

[126] G. Kucinskis, G. Bajars, J. Kleperis, *J. Power Sources* **2013**, *240*, 66–79.

[127] R. J. Young, I. A. Kinloch, L. Gong, K. S. Novoselov, *Compos. Sci. Technol.* **2012**, *72*, 1459–1476.

[128] S. Eigler, C. Dotzer, A. Hirsch, M. Enzelberger, P. Mueller, *Chem. Mater.* **2012**, *24*, 1276–1282.

[129] Y. Su, H. Wei, R. Gao, Z. Yang, J. Zhang, Z. Zhong, Y. Zhang, *Carbon* **2012**, *50*, 2804–2809.

[130] J. R. Hauptmann, T. Li, S. Petersen, J. Nygard, P. Hedegard, T. Bjornholm, B. W. Laursen, K. Norgaard, *Phys. Chem. Chem. Phys.* **2012**, *14*, 14277–14281.

[131] C. Laffon, S. Lacombe, F. Bournel, P. Parent, *J. Chem. Phys.* **2006**, *125*, 204714.

[132] G. Marcotte, P. Ayotte, A. Bendounan, F. Sirotti, C. Laffon, P. Parent, *J. Phys. Chem. Lett.* **2013**, *4*, 2643–2648.

[133] M. Cavalleri, H. Ogasawara, L. Pettersson, A. Nilsson, *Chem. Phys. Lett.* **2002**, *364*, 363–370.

[134] V. Gun'ko, V. Turov, V. Bogatyrev, V. Zarko, R. Leboda, E. Goncharuk, A. Novza, A. Turov, A. Chuiko, *Adv. Colloid Interface Sci.* **2005**, *118*, 125–172.

[135] C. Angell, *Chem. Rev.* **2002**, *102*, 2627–2649.

[136] P. Blaha, K. Schwarz, G. K. H. Madsen, D. Kvasnicka, J. Luitz, *WIEN2k, An Augmented Plane Wave + Local Orbitals Program for Calculating Crystal Properties*, Karlheinz Schwarz, Techn. Universitat Wien, Austria, **2001**.

[137] D. Angmo, F. C. Krebs, *J. Appl. Polym. Sci.* **2013**, *129*, 1–14.

[138] A. Hunt, D. A. Dikin, E. Z. Kurmaev, Y. H. Lee, N. V. Luan, G. S. Chang, A. Moewes, *Carbon* **2014**, *66*, 539–546.

[139] N. Ghaderi, M. Peressi, *J. Phys. Chem. C* **2010**, *114*, 21625–21630.

[140] J. A. Brandes, G. D. Cody, D. Rumble, P. Haberstroh, S. Wirick, Y. Gelinas, *Carbon* **2008**, *46*, 1424–1434.

[141] S. Ryu, L. Liu, S. Berciaud, Y.-J. Yu, H. Liu, P. Kim, G. W. Flynn, L. E. Brus, *Nano Lett.* **2010**, 4944–4951.

[142] T.-F. Yeh, F.-F. Chan, C.-T. Hsieh, H. Teng, *J. Phys. Chem. C* **2011**, *115*, 22587–22597.

[143] H. K. Jeong, C. Yang, B. S. Kim, K.-J. Kim, *EPL* **2010**, *92*, 37005.

[144] B. R. Lee, J.-W. Kim, D. Kang, D. W. Lee, S.-J. Ko, H. J. Lee, C.-L. Lee, J. Y. Kim, H. S. Shin, M. H. Song, *ACS Nano* **2012**, *6*, 2984–2991.

[145] H. K. Jeong, M. H. Jin, K. P. So, S. C. Lim, Y. H. Lee, *J. Phys. D Appl Phys* **2009**, *42*, 65418.

Appendix A

Permissions to Reproduce

Two of the manuscripts in this thesis, *Epoxide Speciation and Functional Group Distribution in Graphene Oxide Paper-Like Materials* and *Modulation of the band gap of graphene oxide: The role of AA-stacking* have already been published in *Advanced Functional Materials* and *Carbon*, respectively. So that the copyrighted work contained in these journals may be reproduced, permission has been sought from Bettina Loycke, Senior Rights Manager with Wiley, the company that publishes *Advanced Functional Materials*, and from Hop Wechsler, Permissions Helpdesk Manager with Elsevier, the company that publishes *Carbon*. The email exchanges with these individuals have been included here. The record shows that I have permission from both companies to reprint their copyrighted work as part of this thesis. Additionally, a printout to the website to which Mr. Wechsler refers, at http://www.elsevier.com/journal-authors/author-rights-and-responsibilities, is included as well. It clearly states that I am within my rights to reproduce the accepted manuscript as part of this thesis.

Hunt, Adrian

From: Rights DE [RIGHTS-and-LICENCES@wiley-vch.de]
Sent: April-29-13 12:32 AM
To: Hunt, Adrian
Subject: AW: Use of AFM publications in my thesis

Dear Adrian,

Yes, if you are not copying the AFM articles and if this is for a thesis, that's fine:

We hereby grant permission for the requested use expected that due credit is given to the original source.

If material appears within our work with credit to another source, authorisation from that source must be obtained.

Credit must include the following components:

- Books: Author(s)/ Editor(s) Name(s): Title of the Book. Page(s). Publication year. Copyright Wiley-VCH Verlag GmbH & Co. KGaA. Reproduced with permission.
- Journals: Author(s) Name(s): Title of the Article. Name of the Journal. Publication year. Volume. Page(s). Copyright Wiley-VCH Verlag GmbH & Co. KGaA. Reproduced with permission.
- Online Portal: Author(s): Title of the Online portal. Link or DOI. Publication year. Copyright Wiley-VCH Verlag GmbH & Co. KGaA. Reproduced with permission.

With kind regards

Bettina Loycke
Senior Rights Manager
Rights & Licenses

Wiley-VCH Verlag GmbH & Co. KGaA
Boschstraße 12
69469 Weinheim
Germany
www.wiley-vch.de

T +(49) 6201 606-280
F +(49) 6201 606-332
rightsDE@wiley.com

WILEY

Von: Hunt, Adrian [mailto:adrian.hunt@usask.ca]
Gesendet: Freitag, 26. April 2013 20:15

An: Rights DE
Betreff: Use of AFM publications in my thesis

Good afternoon.

I had originally sent this email to the editors, but they have said that I should ask this of you.

My name is Adrian Hunt, and I currently have a paper (adfm.201200529) published with AFM. I also have a second paper (adfm.201300808) that is currently going through the review process. I have a question concerning how I may include the material that I have published in my thesis.

In short, I would like to use my words (i.e. the text and figures), but not the formatting, in my thesis. This would be expedient as I would not have to spend time rephrasing work that has already been deemed acceptable to the scientific community. The versions would not be the same because I would have to expand upon the papers where appropriate on analysis and/or discussion that would not fit into a journal article. However, there would be many similarities.

Is this acceptable?

Regards,

Adrian

Hunt, Adrian

From: Permissions Helpdesk [permissionshelpdesk@elsevier.com]
Sent: November-22-13 11:31 AM
To: Hunt, Adrian
Subject: RE: Thesis

Dear Adrian:

Permission is covered by the rights you retain as an Elsevier journal author as outlined at http://www.elsevier.com/journal-authors/author-rights-and-responsibilities, which include Inclusion in a thesis or dissertation**,** provided that proper acknowledgement is given to the original source of publication. Should you require any further clarification, please let me know. Best of luck with your thesis.

Regards,
Hop

Hop Wechsler
Permissions Helpdesk Manager
Global Rights Department
Elsevier
1600 John F. Kennedy Boulevard
Suite 1800
Philadelphia, PA 19103-2899
Tel: +1-215-239-3520
Mobile: +1-215-900-5674
Fax: +1-215-239-3805
E-mail: h.wechsler@elsevier.com
Questions about obtaining permission: whom to contact? What rights to request? When is permission required? Contact the Permissions Helpdesk at:
+1-800-523-4069 x 3808 *permissionshelpdesk@elsevier.com*

From: Hunt, Adrian [mailto:adrian.hunt@usask.ca]
Sent: Wednesday, November 20, 2013 4:04 PM
To: Permissions Helpdesk
Subject: Thesis

Good afternoon.

My name is Adrian Hunt, and I very recently published an article in Carbon. (Carbon 66 539-546 (2014), "Modulation of the band gap of graphene oxide: The role of AA-stacking") I would now like to put this article in my thesis as part of a manuscript-based Ph.D. thesis.

If I include this paper, it will be publically available from the University of Saskatchewan as part of my thesis, however it will not be a stand-alone document that can be located independently of the rest of the work contained therein. As such, someone could get access to the article, but only if they first knew where to find it.

I am unclear as to whether I may put the paper in my thesis as part of ‘fair use’. Do I have permission to put this work in my thesis?

Regards,

Adrian

For Authors

- Journal authors' home
- **Author Rights**
- Ethics
- Funding body agreements
- Author services
- Journal performance
- Early career researchers
- Authors' update
- Book authors' home
- Getting your paper noticed

Author Rights

Elsevier supports the need for authors to share, disseminate and maximize the impact of their research. We take our responsibility as stewards of the online record seriously, and work to ensure our policies and procedures help to protect the integrity of scholarly works.

Author's rights to reuse and post their own articles published by Elsevier are defined by Elsevier's copyright policy. For our proprietary titles, the type of copyright agreement used depends on the author's choice of publication:

For subscription articles: These rights are determined by a copyright transfer, where authors retain scholarly rights to post and use their articles.

For open access articles: These rights are determined by an exclusive license agreement, which applies to all our open access content.

In both cases, the fundamental rights needed to publish and distribute an article remain the same and Elsevier authors will be able to use their articles for a wide range of scholarly purposes.

Details on how authors can reuse and post their own articles are provided below.

Help and support
For reuse and posting not detailed below, please see our posting policy, or for authors who would like to:

- Include material from other sources in your work being published by Elsevier, please visit: Permission seeking guidelines for Elsevier authors.
- Obtain permission to re-use material from Elsevier books, journals, databases, or other products, please visit: Obtaining permission to reuse Elsevier material
- Or if you are an Elsevier author and are contacted by a requestor who wishes to re-use all or part of your article or chapter, please also refer them to our Obtaining Permission to Re-Use Elsevier Material page.
- See our FAQ on posting and copyright queries.
- Contact us directly, please email our Permissions Help Desk.

Author Use | Author Posting | Definitions

How authors can use their own journal articles

Authors can use their articles for a wide range of scholarly, non-commercial purposes as outlined below. These rights apply for all Elsevier authors who publish their article as either a subscription article or an open access article.

We require that all Elsevier authors always include a full acknowledgement and, if appropriate, a link to the final published version hosted on Science Direct.

For open access articles these rights are separate from how readers can reuse your article as defined by the author's choice of Creative Commons user license options.

Authors can use either their accepted author manuscript or final published article for:	
	Use at a conference, meeting or for teaching purposes
	Internal training by their company
	Sharing individual articles with colleagues for their research use* (also known as 'scholarly sharing')
	Use in a subsequent compilation of the author's works
	Inclusion in a thesis or dissertation
	Reuse of portions or extracts from the article in other works
	Preparation of derivative works (other than for commercial purposes)

*Please note this excludes any systematic or organized distribution of published articles.